

P wave tomography for 3-D radial and azimuthal anisotropy beneath Greenland and surrounding regions

Genti Toyokuni¹ and Dapeng Zhao¹

¹Tohoku University

November 22, 2022

Abstract

We present the first 3-D images of *P*-wave radial anisotropy (RAN) and azimuthal anisotropy (AAN) down to 750-km depth beneath Greenland and surrounding regions. The results are obtained by applying a regional tomographic method to simultaneously invert *P* wave arrival times of 1,309 local events and *P* wave relative traveltime residuals of 7,202 teleseismic events, which were recorded mainly by the latest GLISN network. A high-velocity body located beneath northeast Greenland (NEG) to its offshore exhibits a strong negative RAN and a strong AAN with N-S to NE-SW oriented fast-velocity directions (FVDs). The FVDs are generally consistent with the direction of the fold axis of the Caledonian fold belt, which is considered as an outcrop of the NEG body on land. Beneath the Iceland, Jan Mayen, and Svalbard hotspots, a strong positive RAN and a negligible or weak AAN are revealed, which may reflect effects of upwelling mantle plumes. Among the three regions, a weak AAN with a constant FVD is only revealed beneath Iceland, which may reflect the existence of background mantle flow. The RAN and AAN features beneath the Labrador Sea, Davis Strait, and Baffin Bay suggest the following scenario on breakup between Greenland and Canada: the breakup was initiated at the Labrador Sea due to local mantle upwelling, but the northward propagation of the breakup was blocked by a strong high-velocity anomaly beneath Davis Strait; the opening of Baffin Bay might be caused passively by far-field plate forces.



Tectonics

Supporting Information for

***P* wave tomography for 3-D radial and azimuthal anisotropy beneath Greenland and surrounding regions**

Genti Toyokuni¹ and Dapeng Zhao¹

1 Department of Geophysics, Graduate School of Science, Tohoku University, Sendai 980-8578, Japan

Contents of this file

Figures S1 to S20

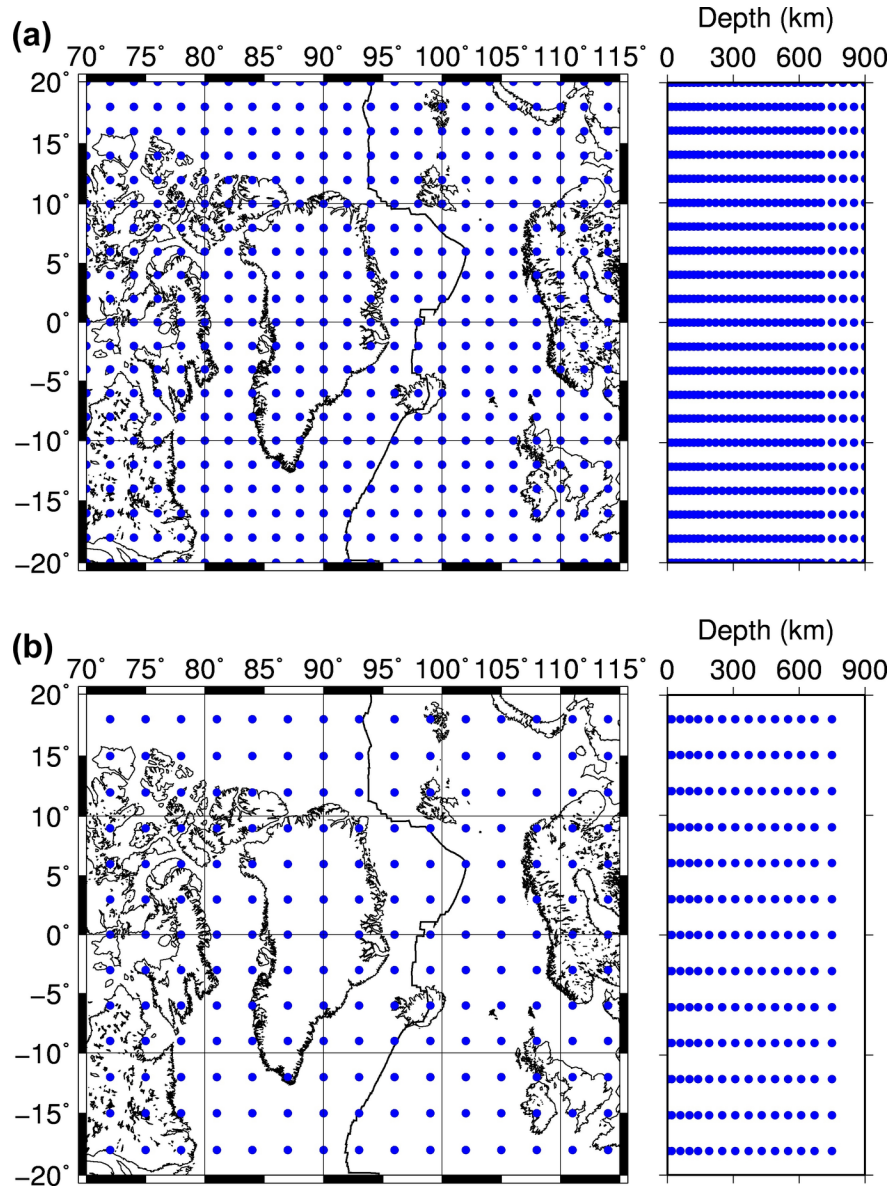


Figure S1 . Distribution of the 3-D grid nodes adopted for (a) isotropic component and (b) anisotropic components in both the V_P radial anisotropy (RAN) and azimuthal anisotropy (AAN) tomography.

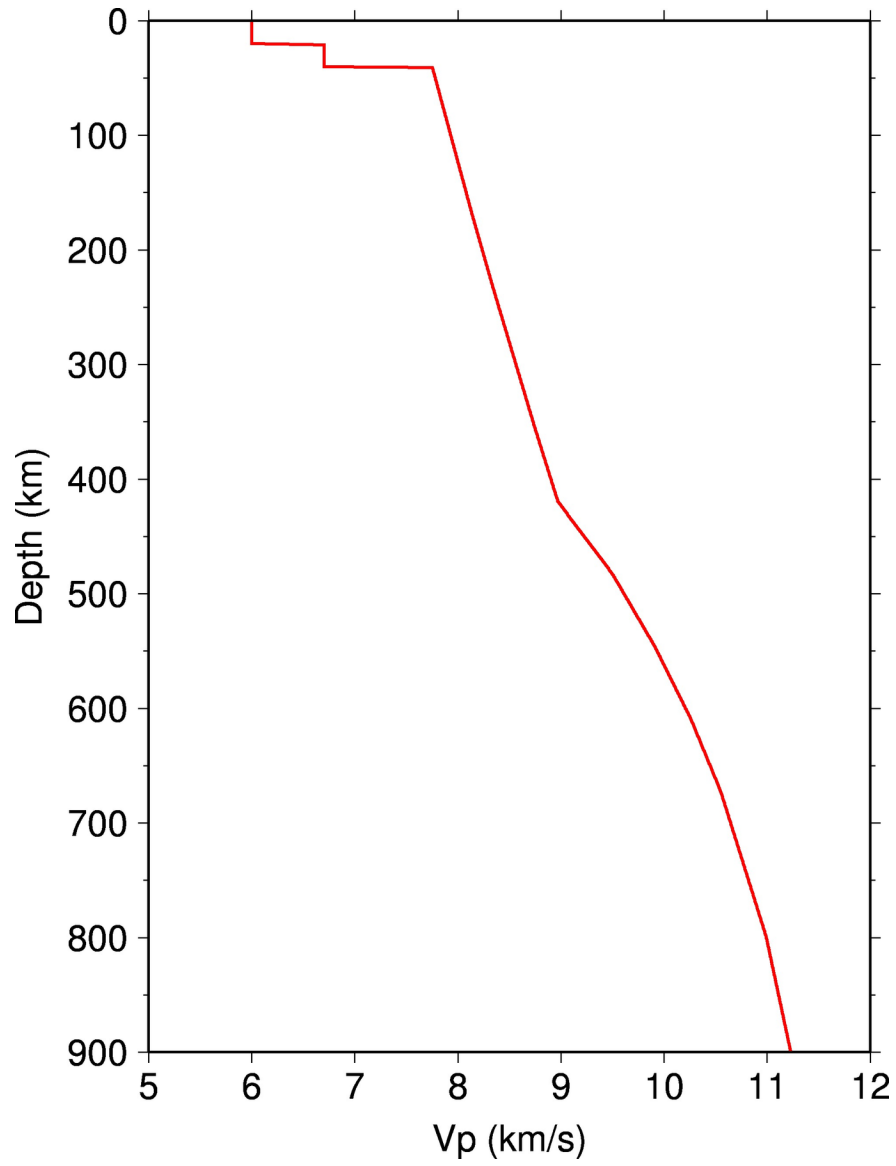


Figure S2 . The starting 1-D P -wave velocity model adopted for the tomographic inversions.

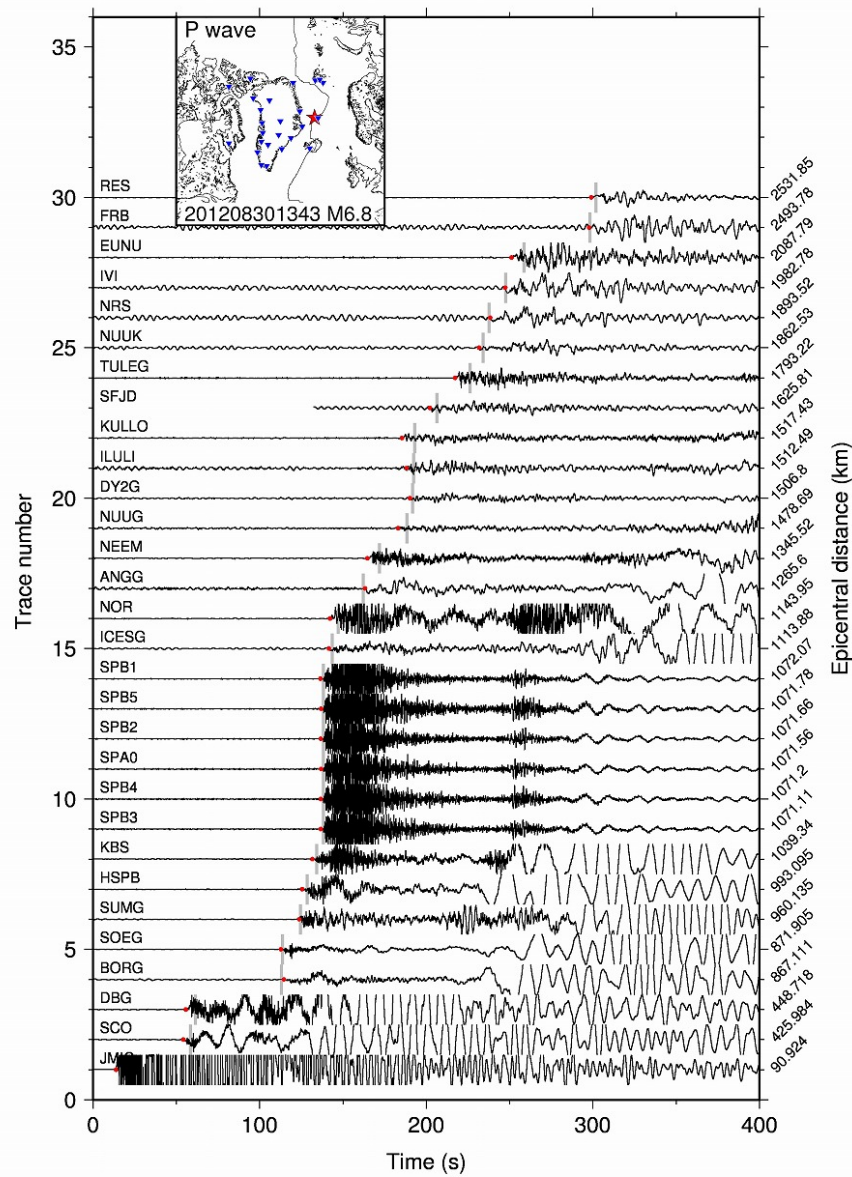


Figure S3 . Examples of picking *P*-wave arrival times of a local earthquake recorded at the GLISN stations. The waveforms are filtered using a Butterworth filter with a frequency band of 1-10 Hz. The red dots denote the picked *P*-wave arrival times; gray bars denote theoretical arrival times calculated for the IASP91 model (Kennett & Engdahl, 1991). The epicenter (red star) and seismic stations (blue triangles) are shown on the inset map.

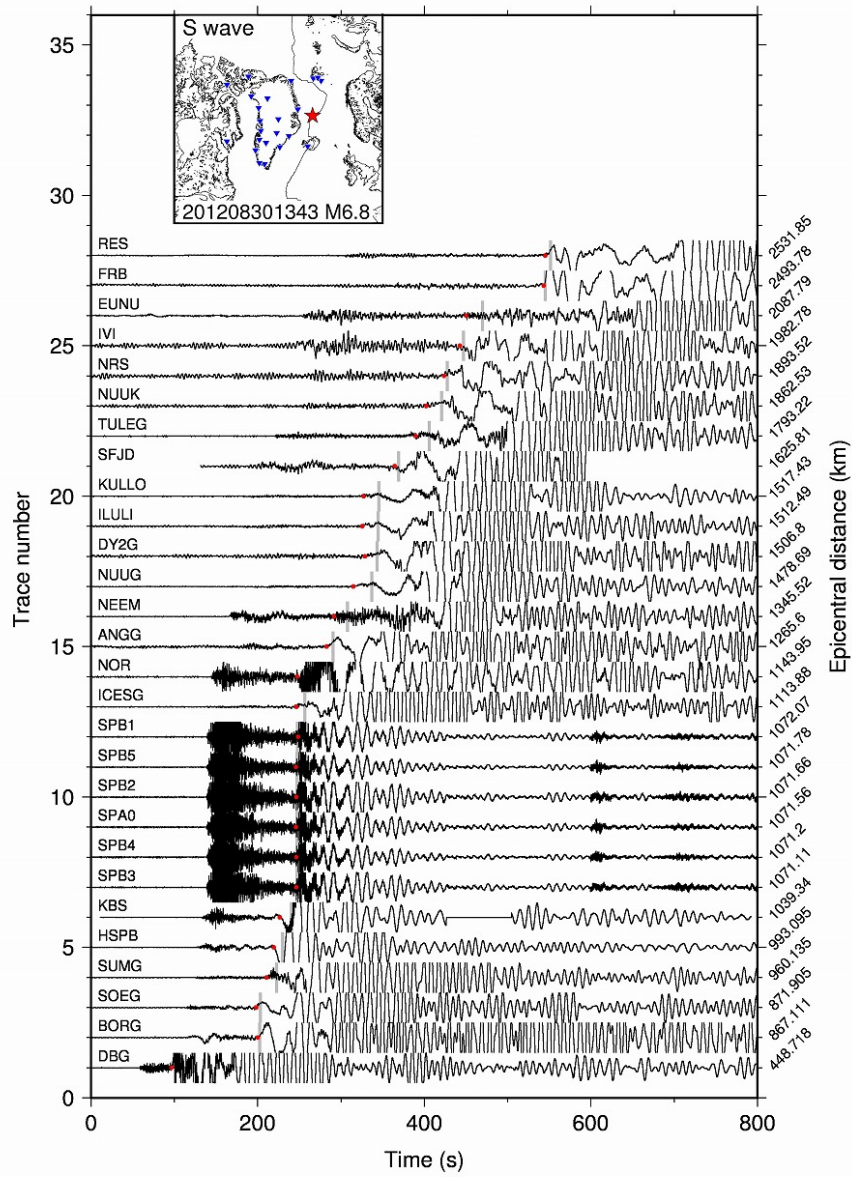


Figure S4 . Same as Figure S3 but for *S* -wave arrival times.

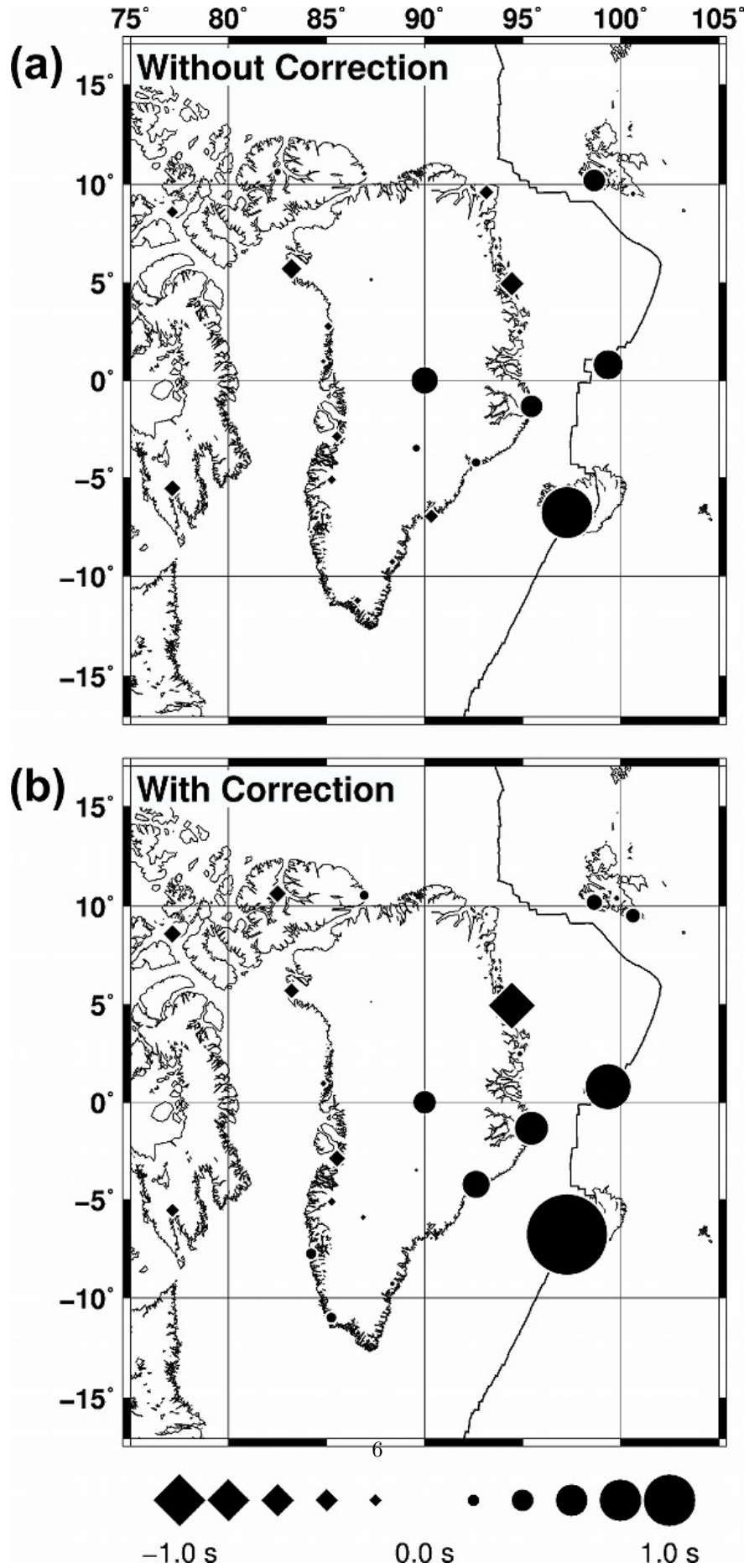


Figure S5. Distribution of average relative teleseismic travel-time residuals at each station used in this study (a) before and (b) after the crustal correction. Diamond and circle symbols denote early and delayed arrivals, respectively.

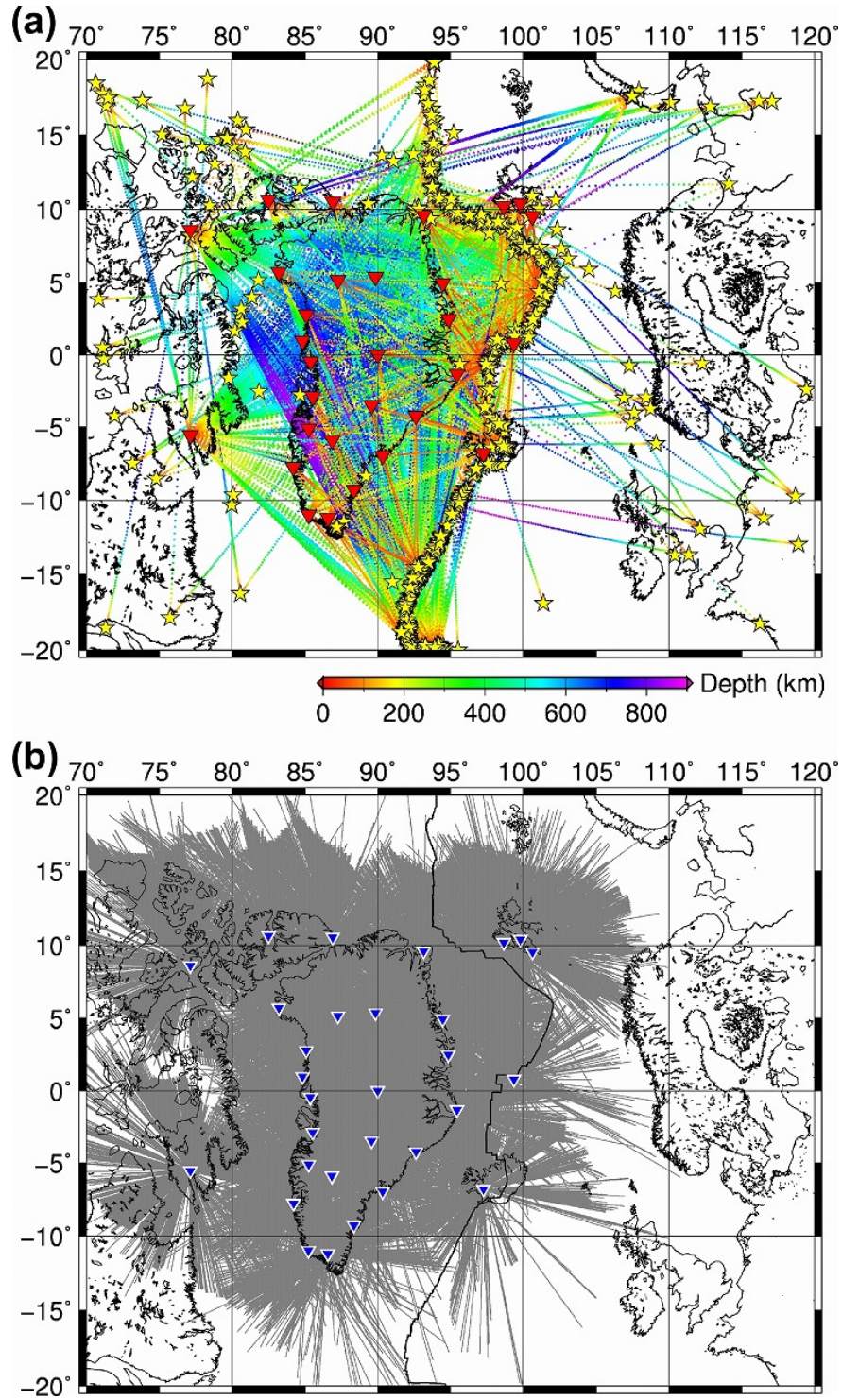


Figure S6. Distribution of seismic rays in the study region. (a) Ray paths from local events. Yellow stars: epicenters of local events; red triangles: seismic stations. Ray color indicates the penetration depth, whose scale is shown at the bottom. (b) Ray paths from teleseismic events. Blue triangles: seismic stations. Note that only the ray paths shallower than 750 km depth are shown.

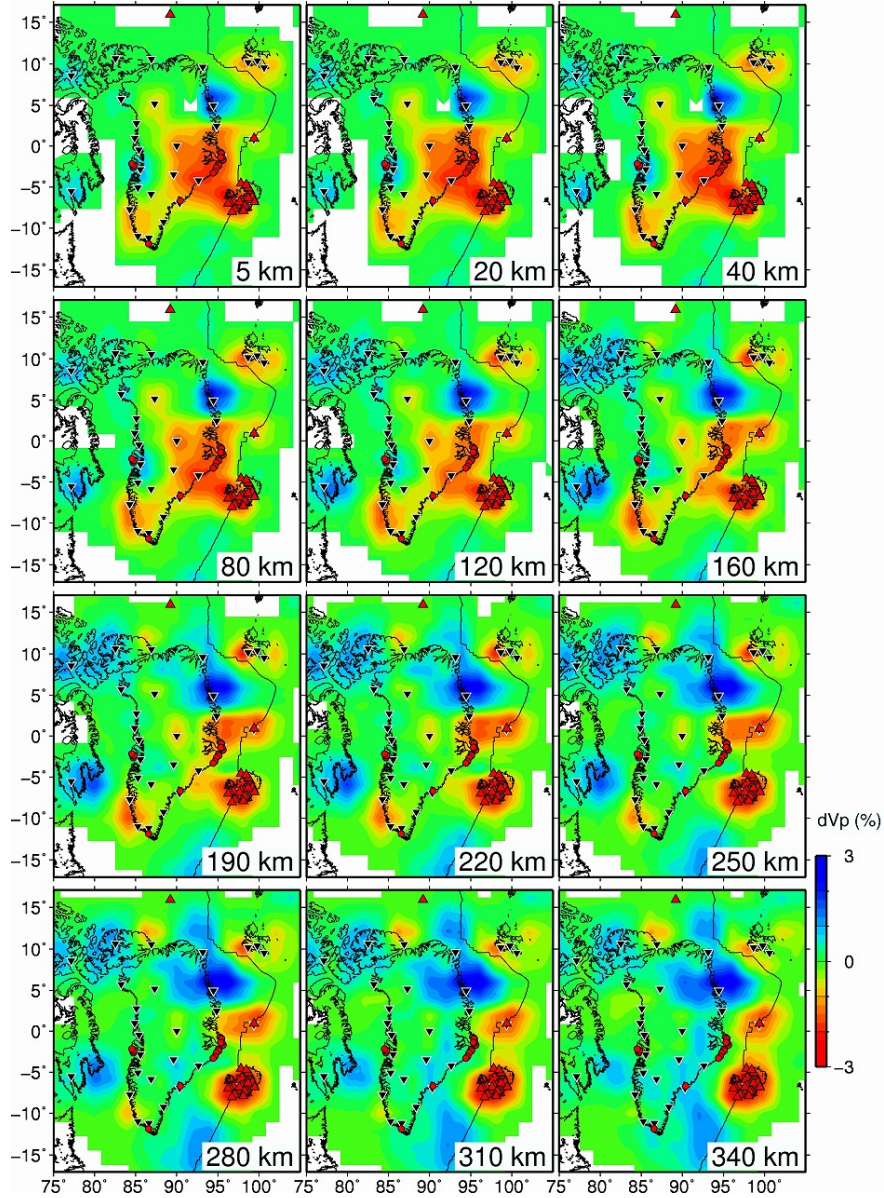


Figure S7.

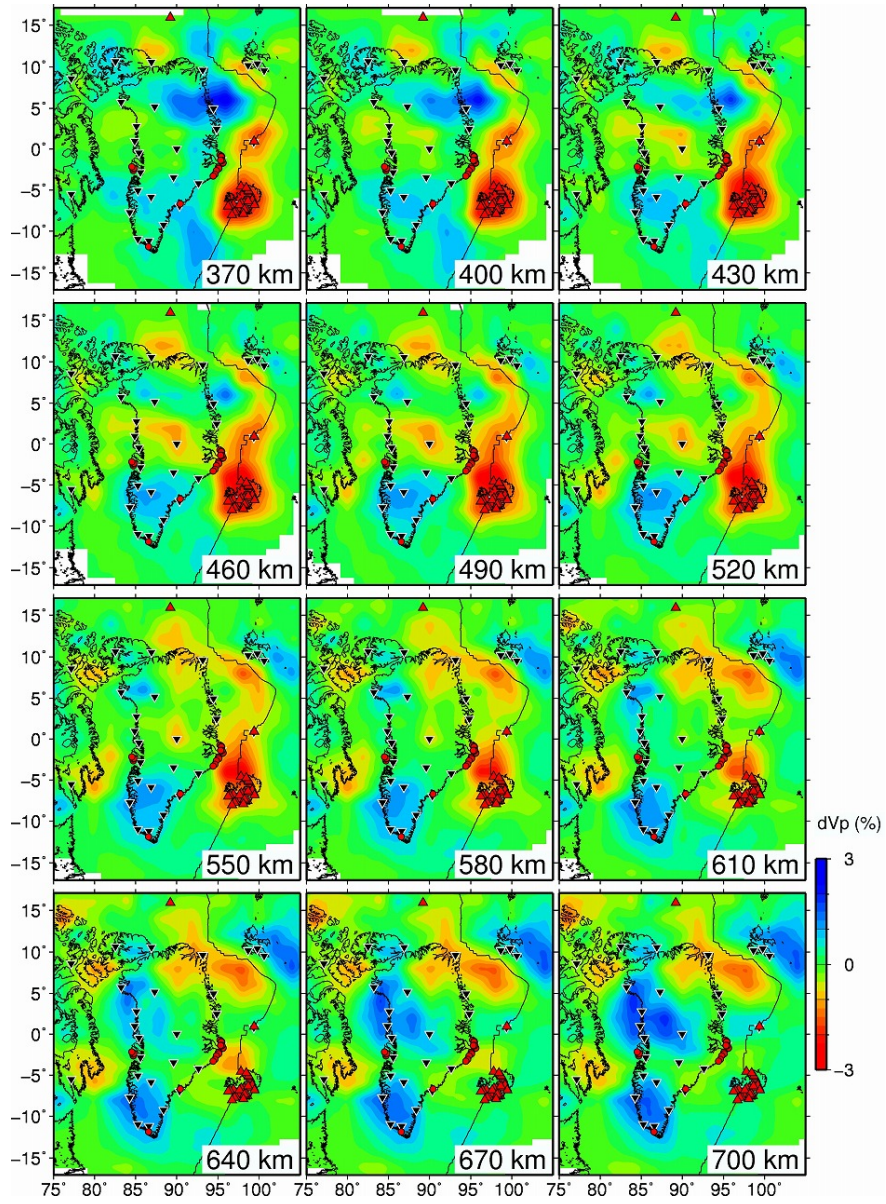


Figure S7. (continued).

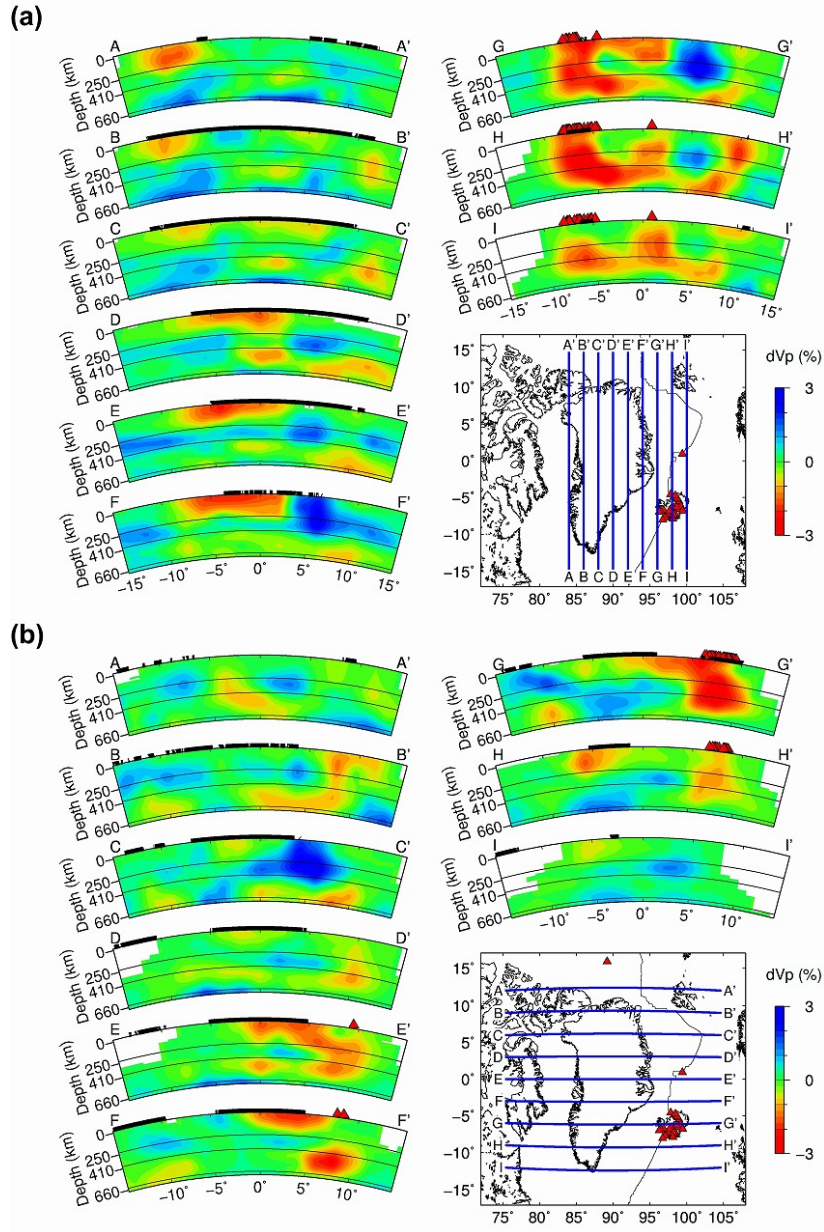


Figure S8.

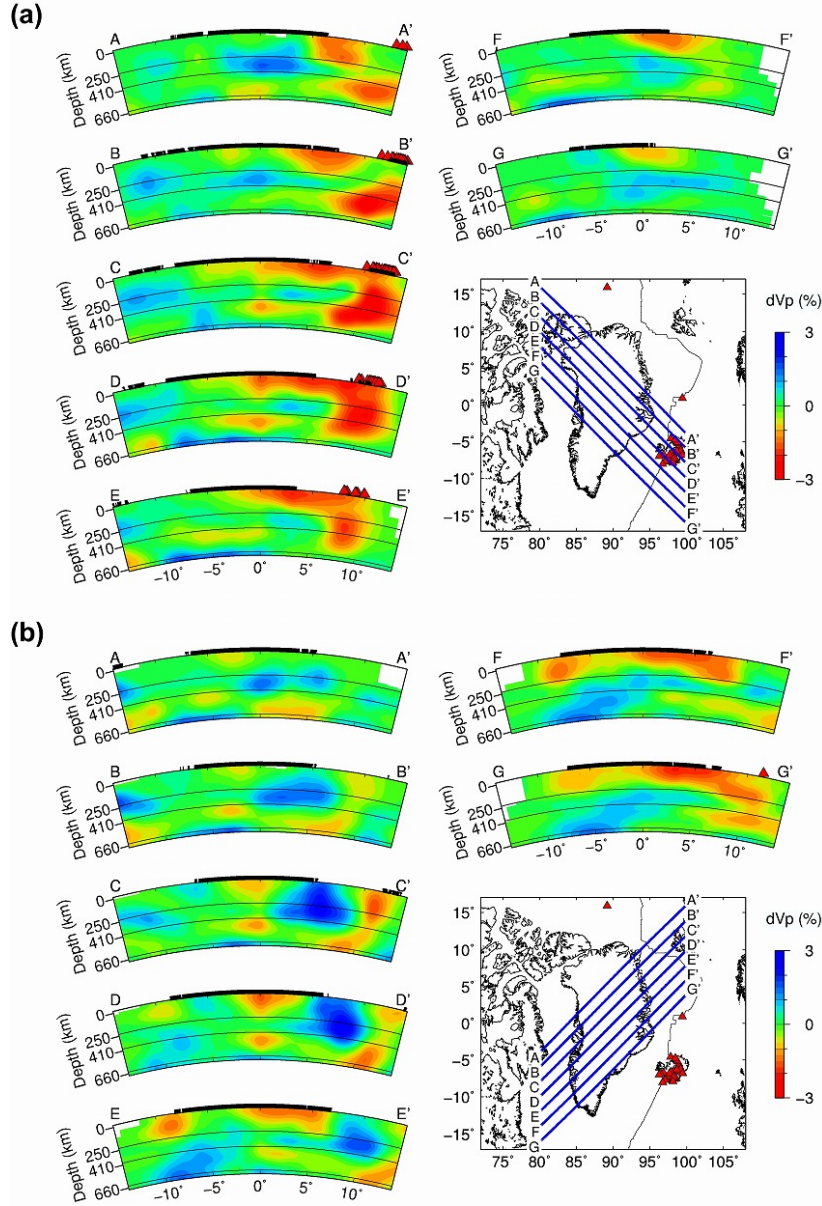


Figure S9.

Figure S7. Map view images of isotopic V_P tomography obtained with the same grid and parameter settings as those in Toyokuni et al. (2020a). The layer depth is shown at the lower-right corner of each panel. Blue and red colors denote high and low V_P perturbations, respectively, whose scale (in %) is shown on the right. Areas with hit counts < 5 are masked in white. The red triangles, red dots, black triangles, and thin black lines denote active volcanoes, hot springs, seismic stations, and plate boundaries, respectively. For comparison, the layout of this figure is exactly the same as that of Figure 4 in Toyokuni et al. (2020a).

Figure S8. Vertical cross-sections of isotopic V_P tomography obtained with the same grid and parameter settings as those in Toyokuni et al. (2020a) along (a) nine N-S oriented profiles and (b) nine E-W oriented profiles. Locations of the profiles are shown on the inset maps. The 250-km depth, and the 410 and 660

km discontinuities are indicated by black solid lines. The thick black lines on the surface denote land areas. Active volcanoes within a $\pm 2^\circ$ width of each profile are shown as red triangles. For comparison, the layout of this figure is exactly the same as that of Figure 5 in Toyokuni et al. (2020a).

Figure S9. Same as Figure S8 but with (a) seven NW-SE oriented profiles and (b) seven NE-SW oriented profiles. For comparison, the layout of this figure is exactly the same as that of Figure 6 in Toyokuni et al. (2020a).

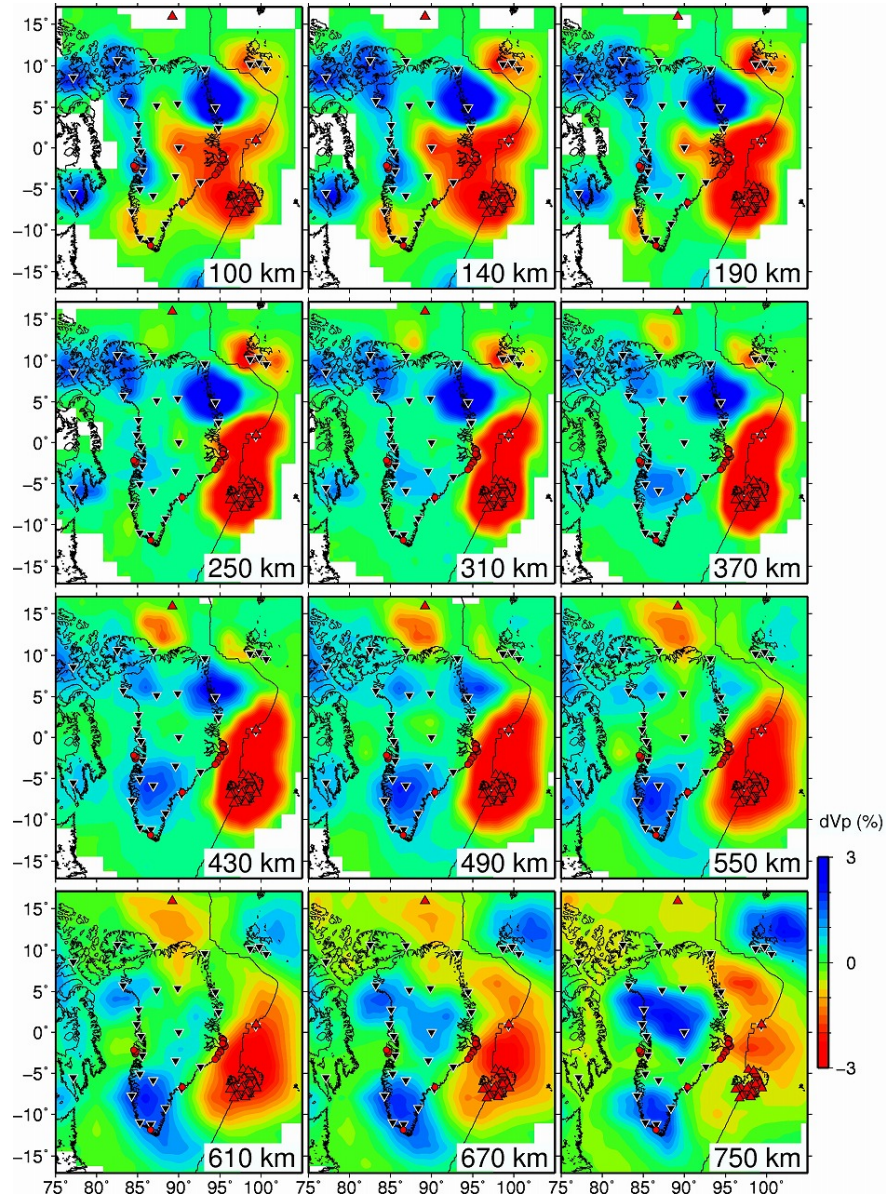
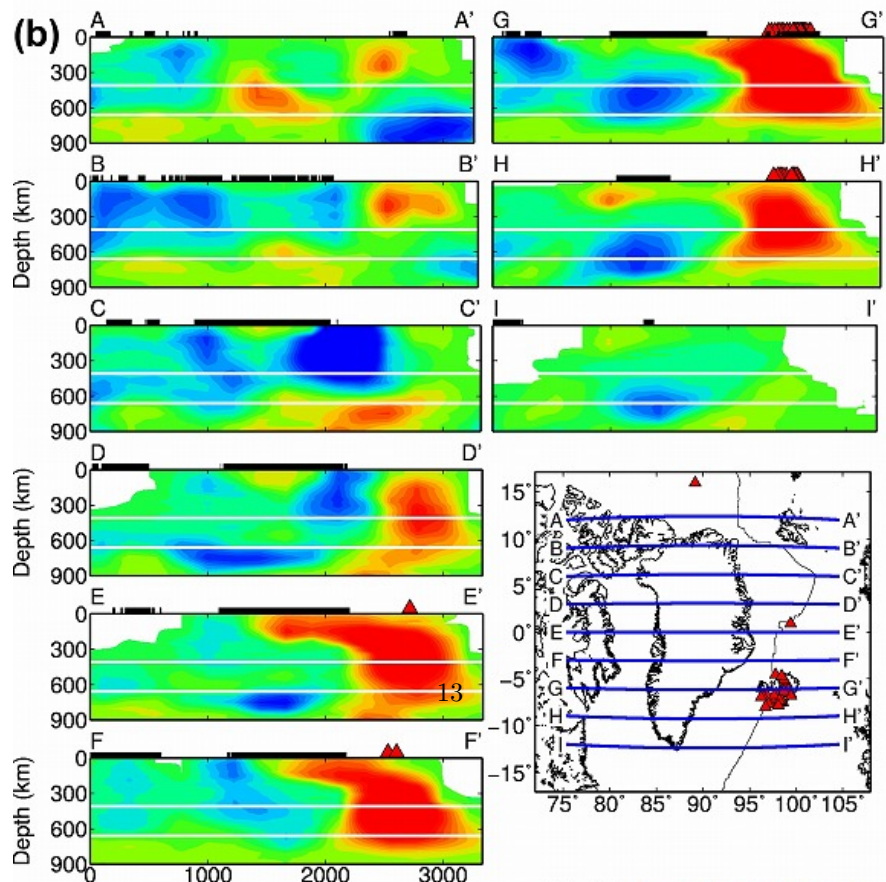
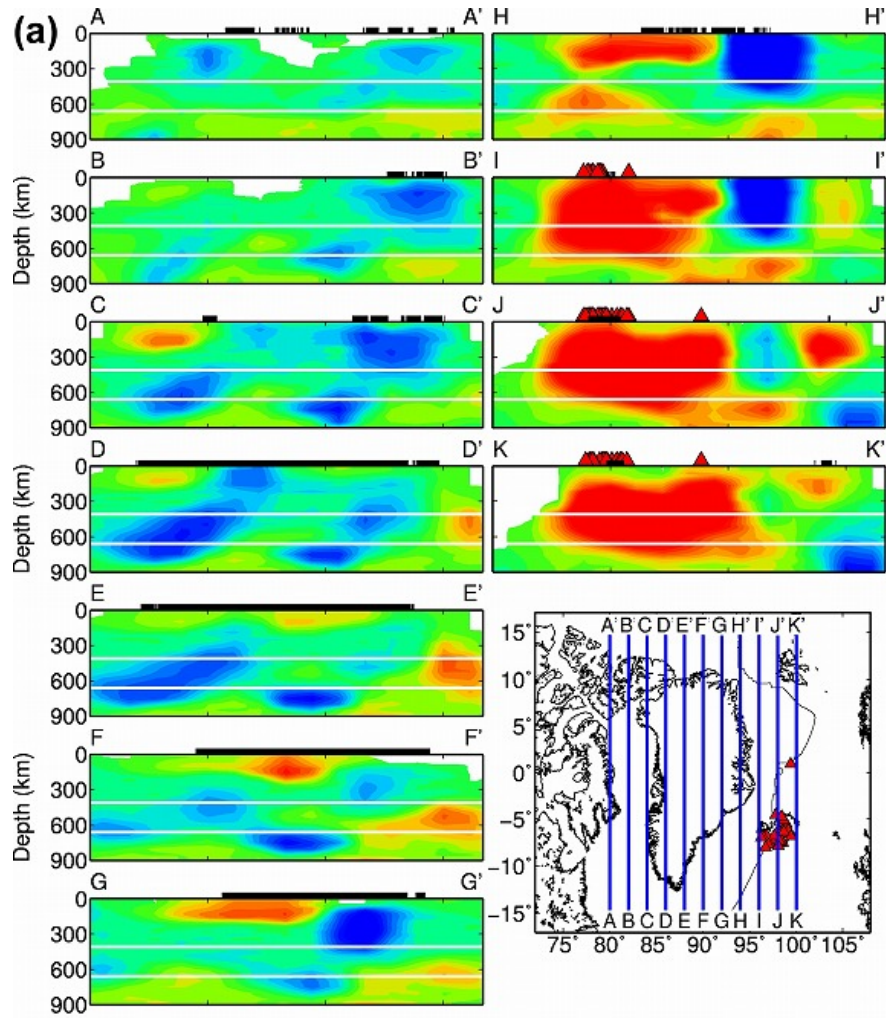


Figure S10. Same as Figure 3 but for V_P isotropic tomography obtained with the same grid setting and the same damping and smoothing parameters as those for the RAN and AAN tomography.



13

Figure S11. Same as Figure 4 but for V_P isotropic tomography obtained with the same grid setting and the same damping and smoothing parameters as those for the RAN and AAN tomography.

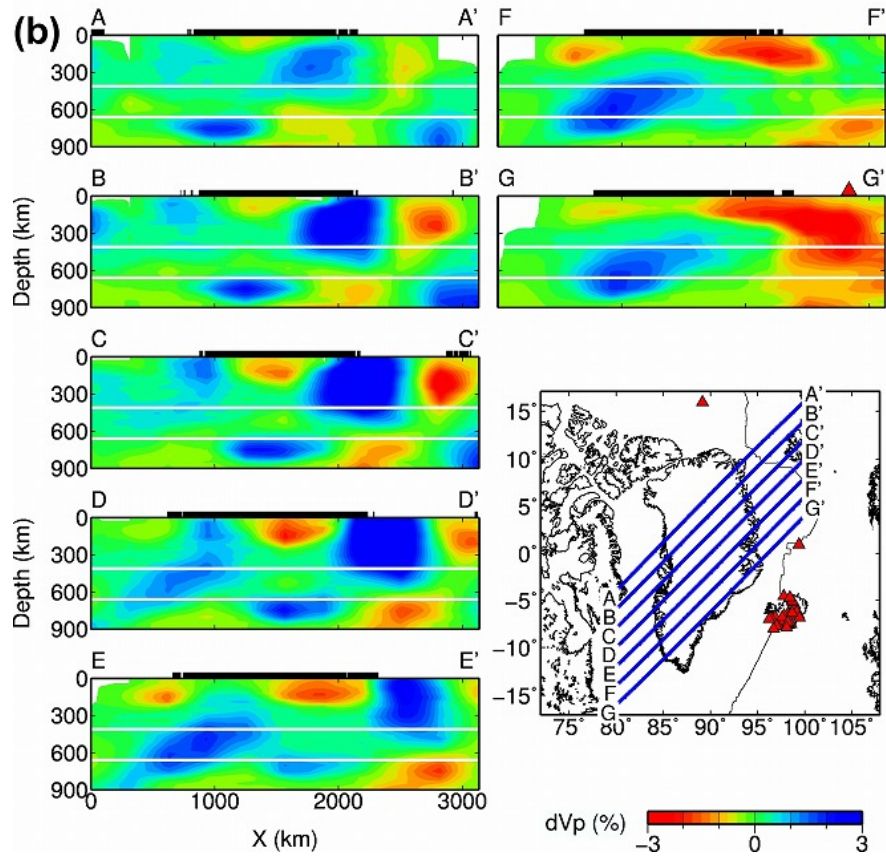
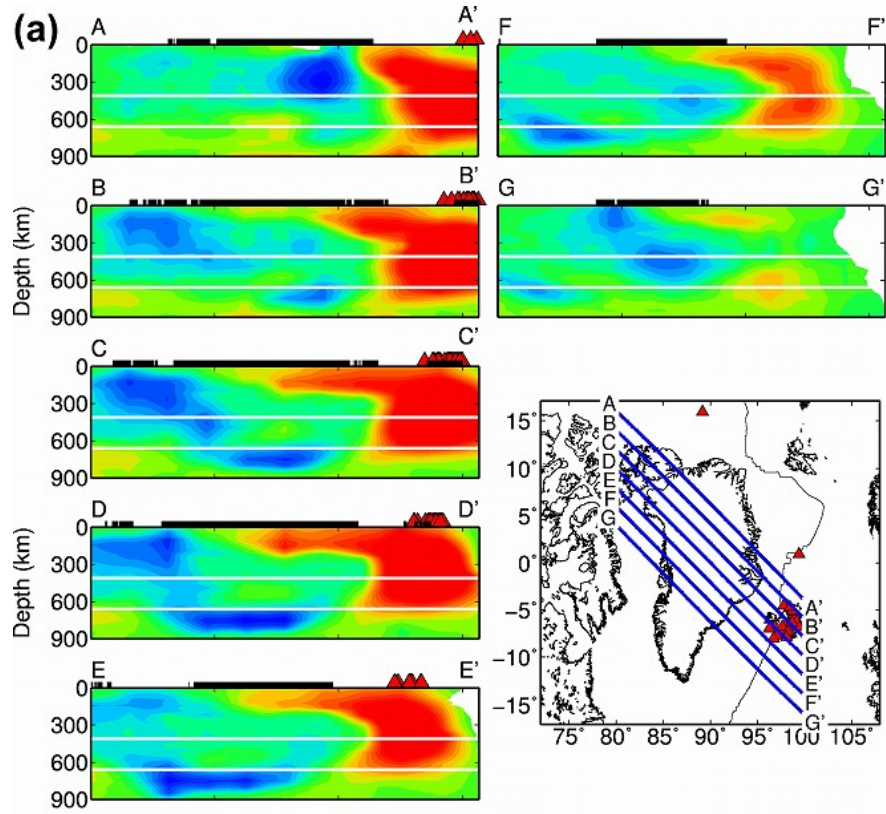


Figure S12. Same as Figure 5 but for V_P isotropic tomography obtained with the same grid setting and the same damping and smoothing parameters as those for the RAN and AAN tomography.

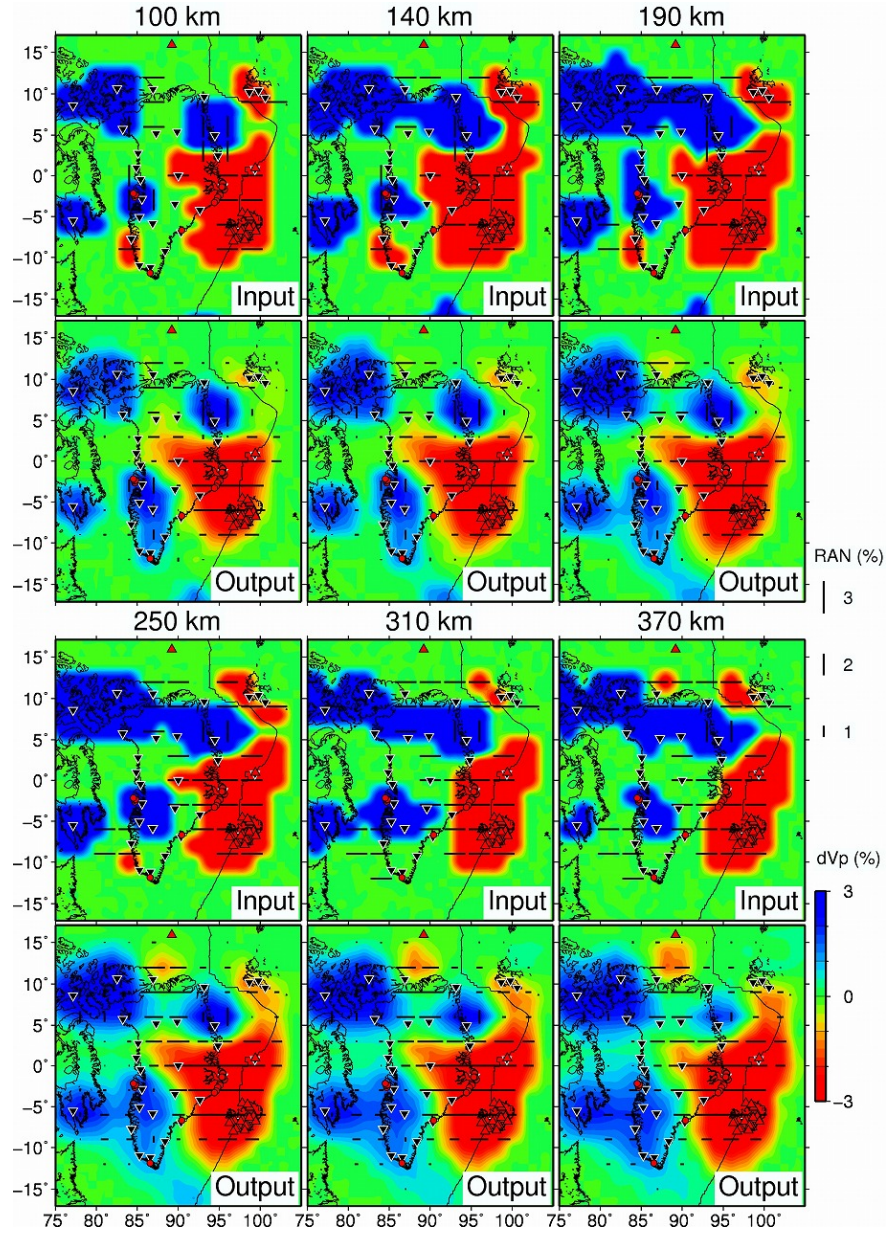


Figure S13. Map view images of the input (upper panels) and output (lower panels) models for the RAN-RRT (Table 1) (RAN: radial anisotropy; RRT: restoring resolution test; see text for details). The layer depth is shown above each panel. Labels are the same as in Figure 3.

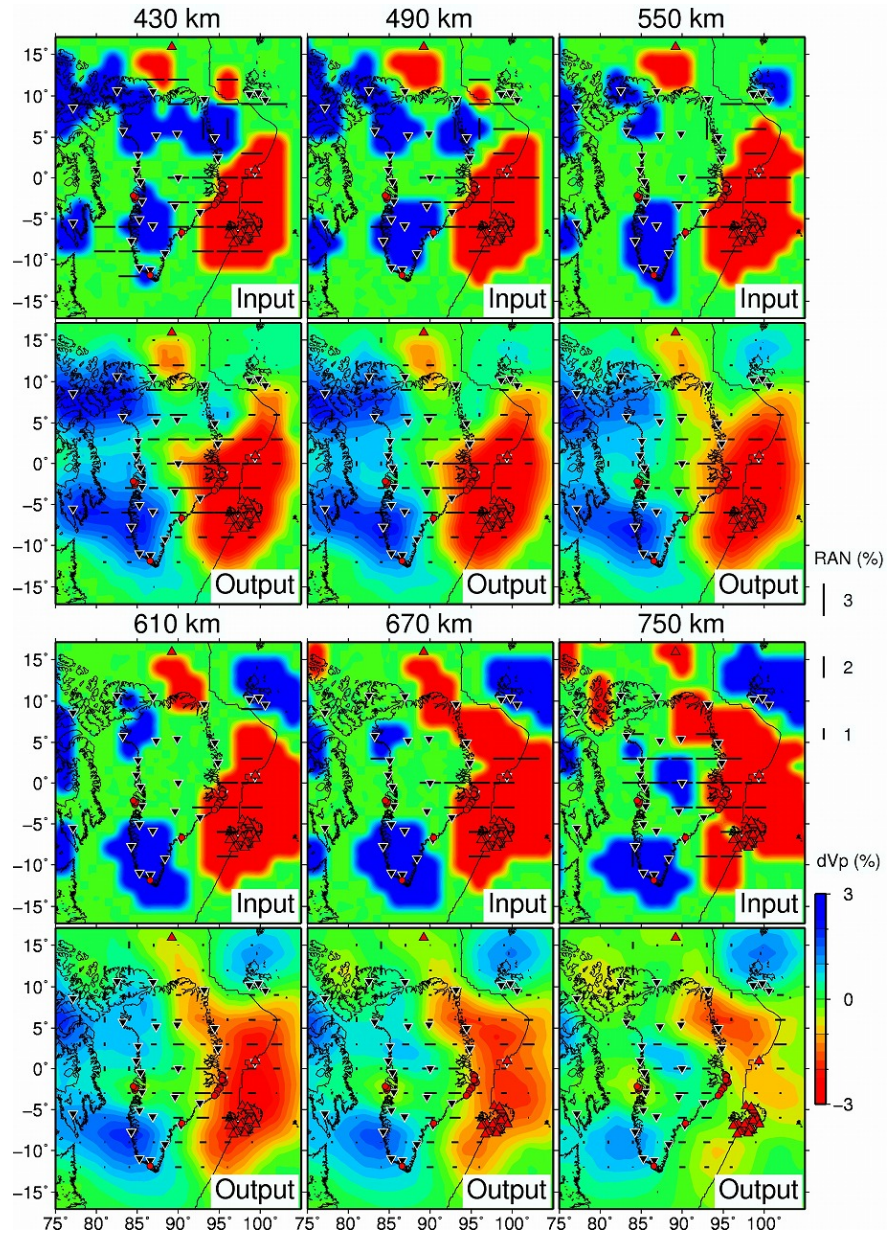


Figure S13. (continued).

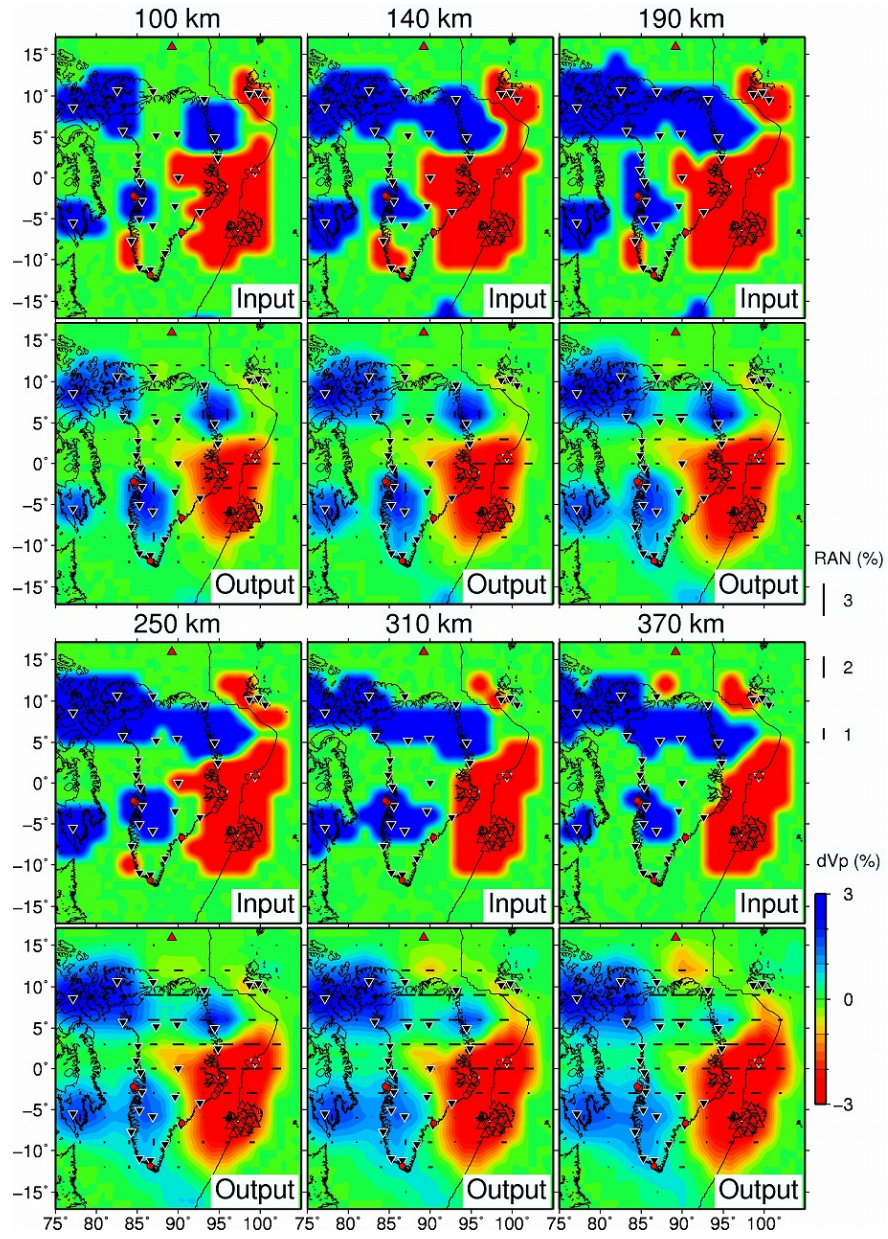


Figure S14. Same as Figure S13 but for the RAN-TOT1 (Table 1) (TOT: trade-off test; see text for details).

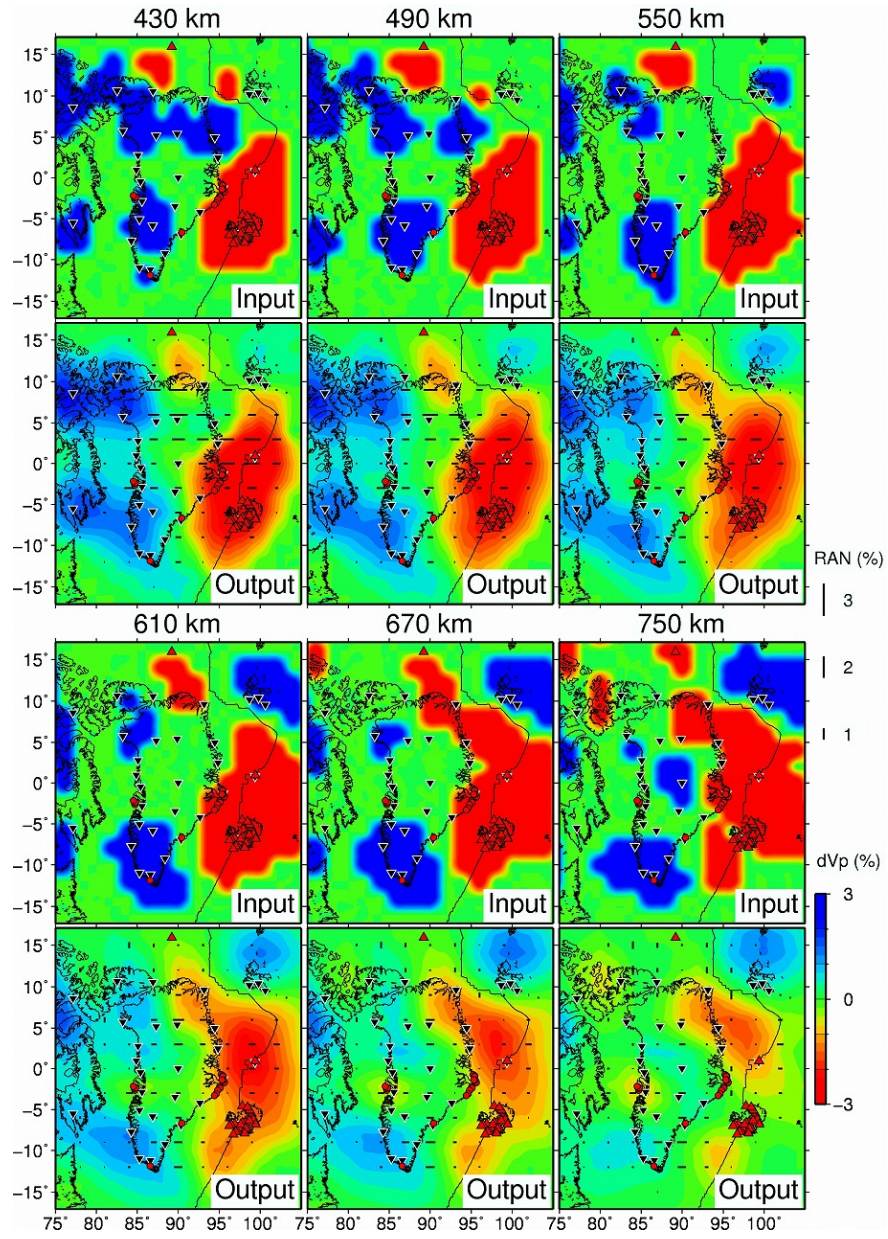


Figure S14. (continued).

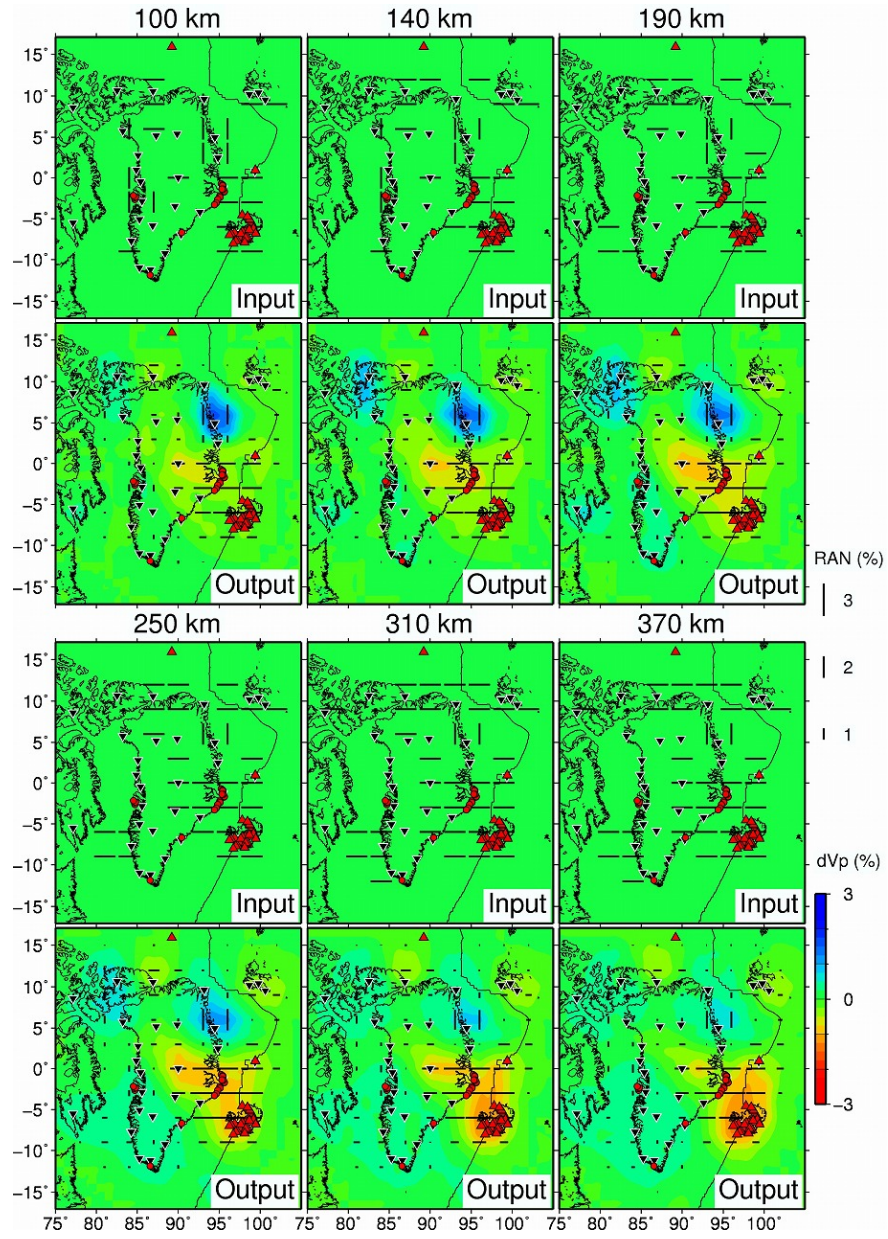


Figure S15. Same as Figure S13 but for the RAN-TOT2 (Table 1) (TOT: trade-off test; see text for details).

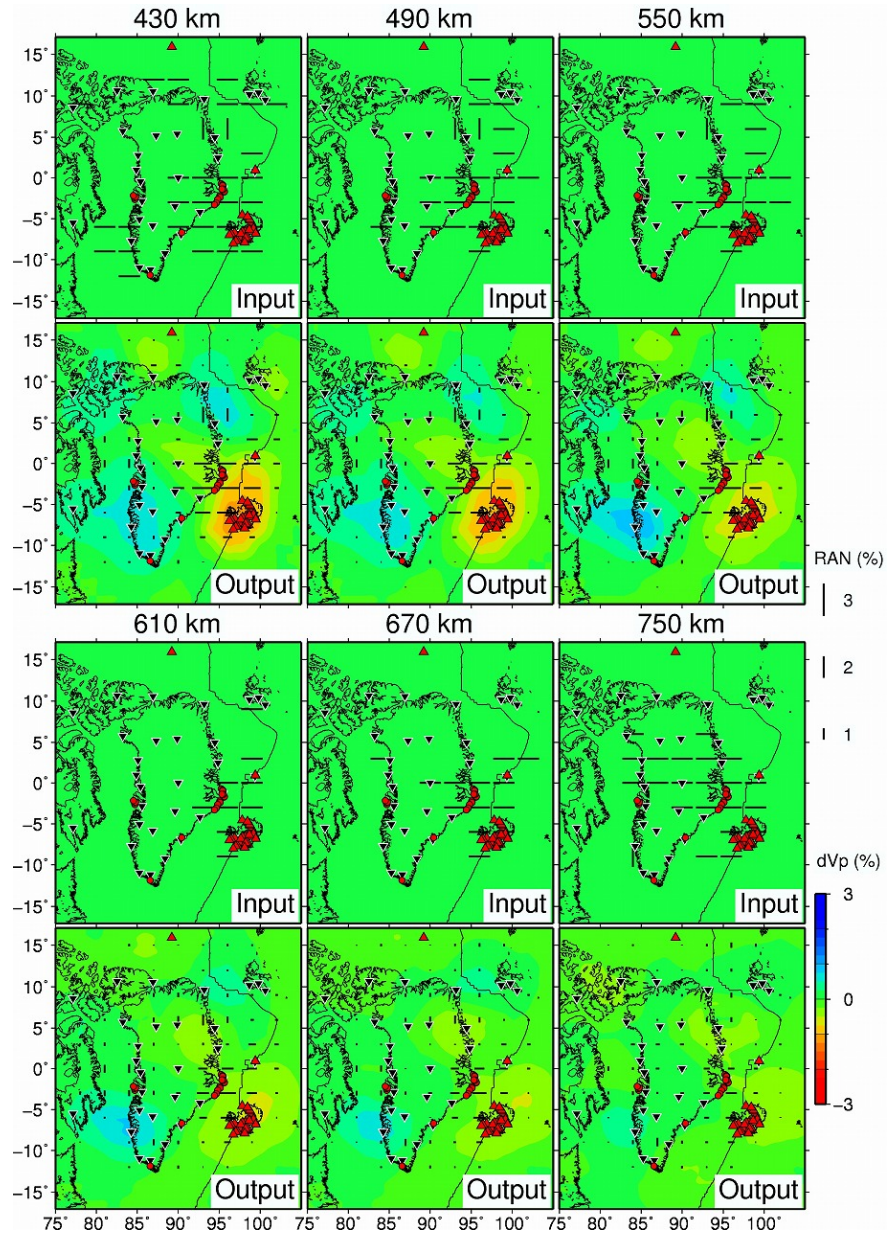


Figure S15. (continued).

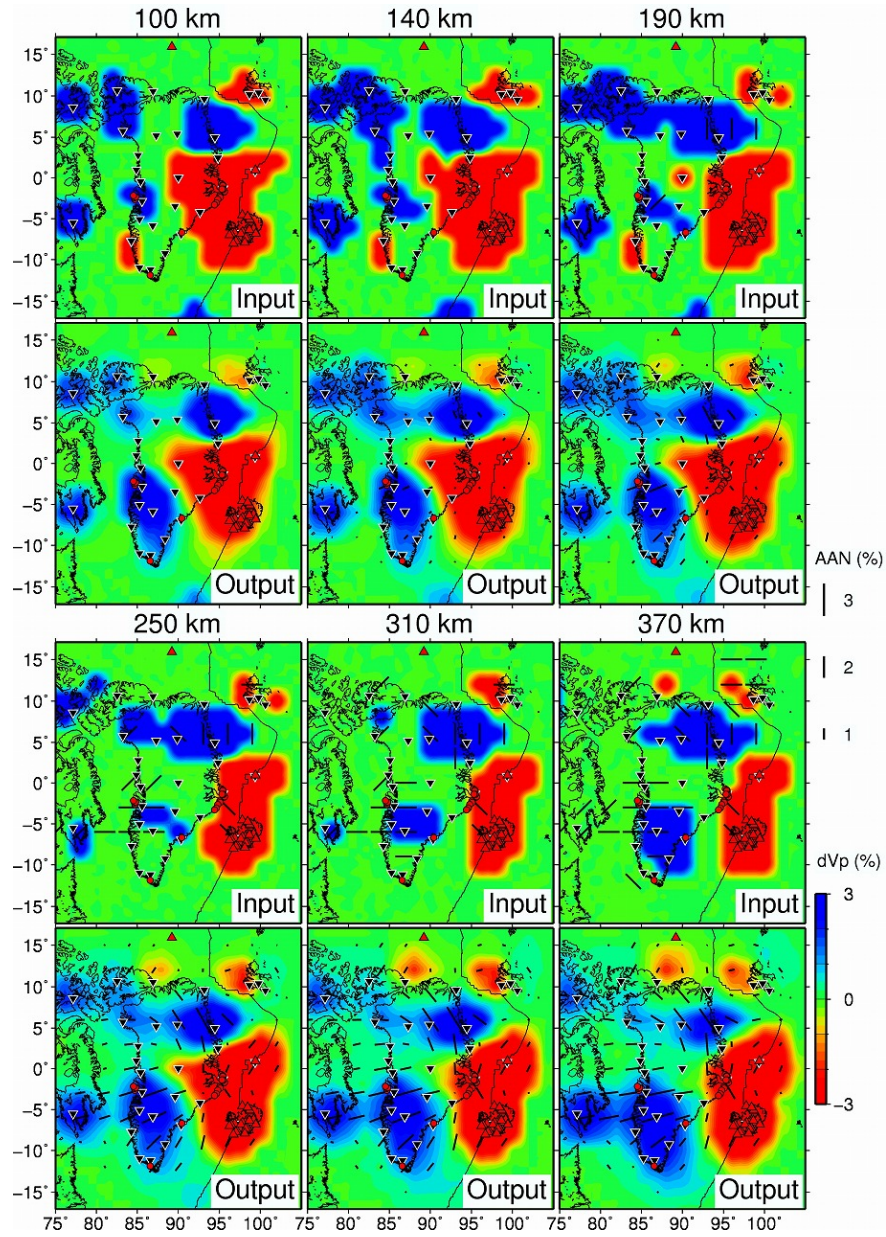


Figure S16. Map view images of the input (upper panels) and output (lower panels) models for the AAN-RRT (Table 1) (AAN: azimuthal anisotropy; RRT: restoring resolution test; see text for details). The layer depth is shown above each panel. Labels are the same as in Figure 6.

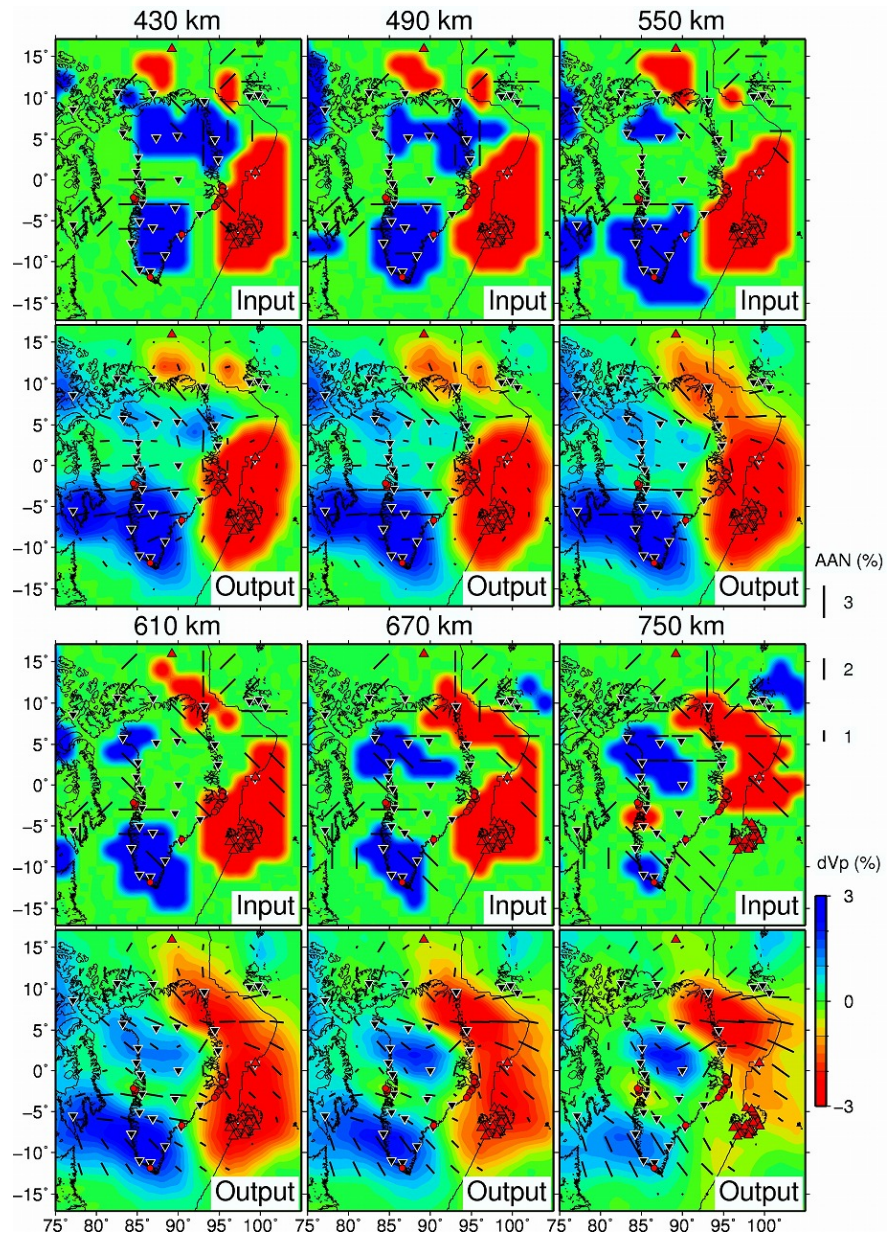


Figure S16. (continued).

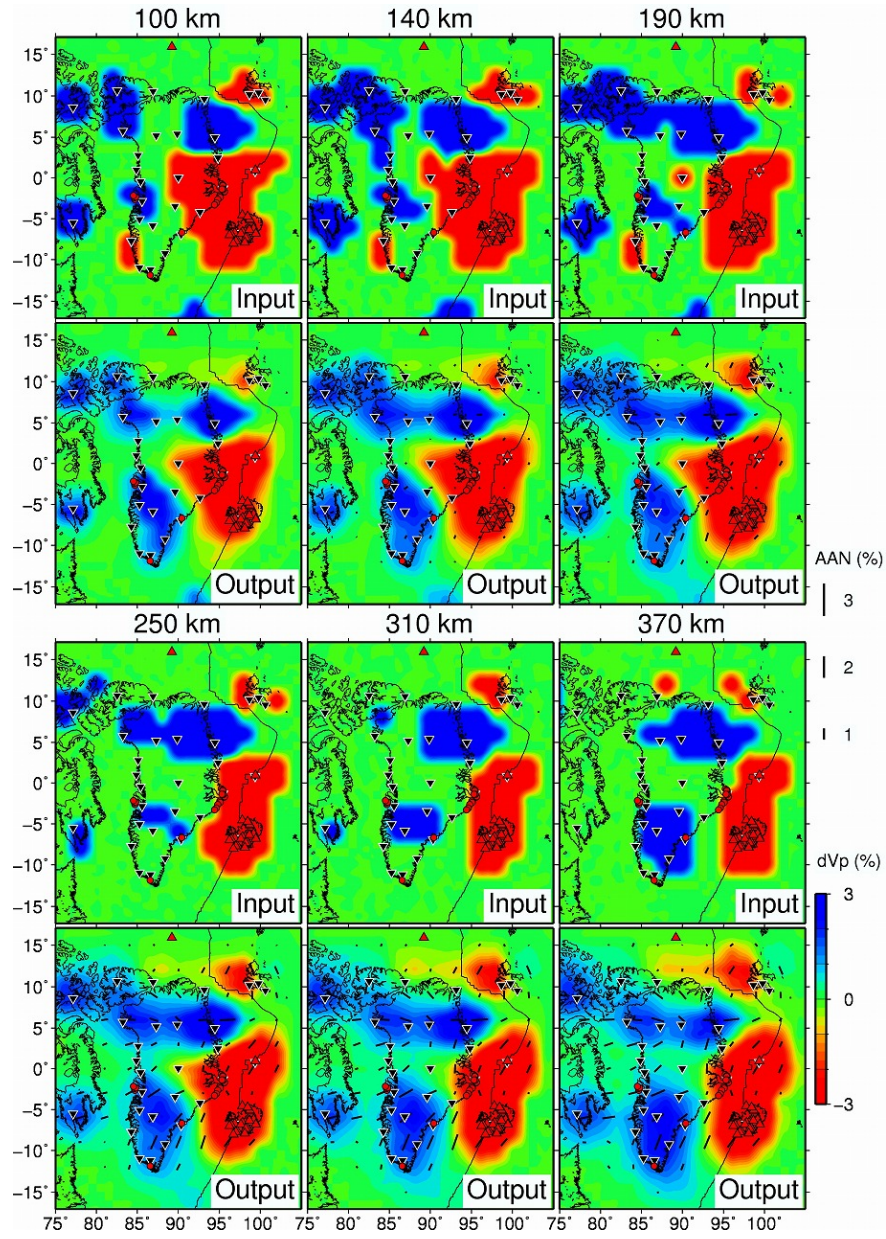


Figure S17. Same as Figure S16 but for the AAN-TOT1 (Table 1) (TOT: trade-off test; see text for details).

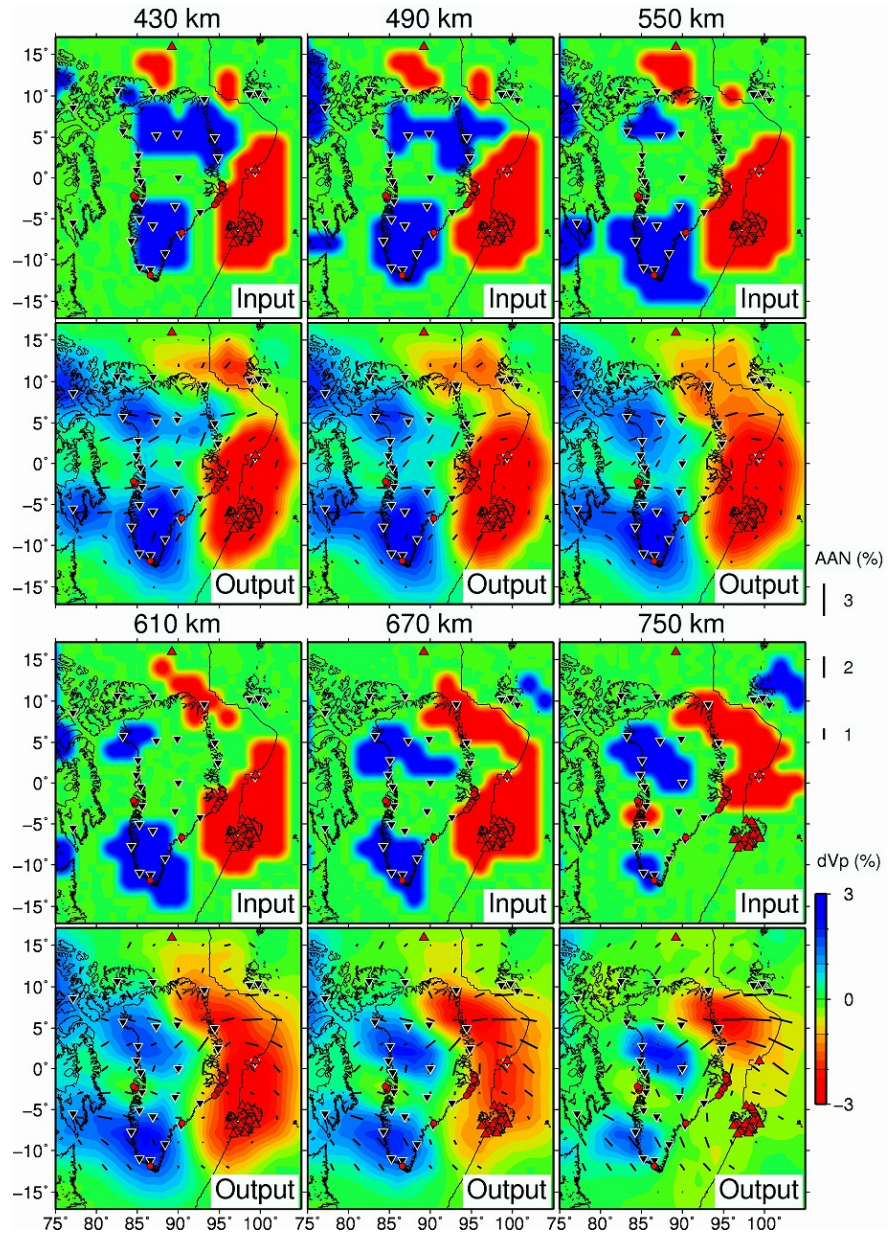


Figure S17. (continued).

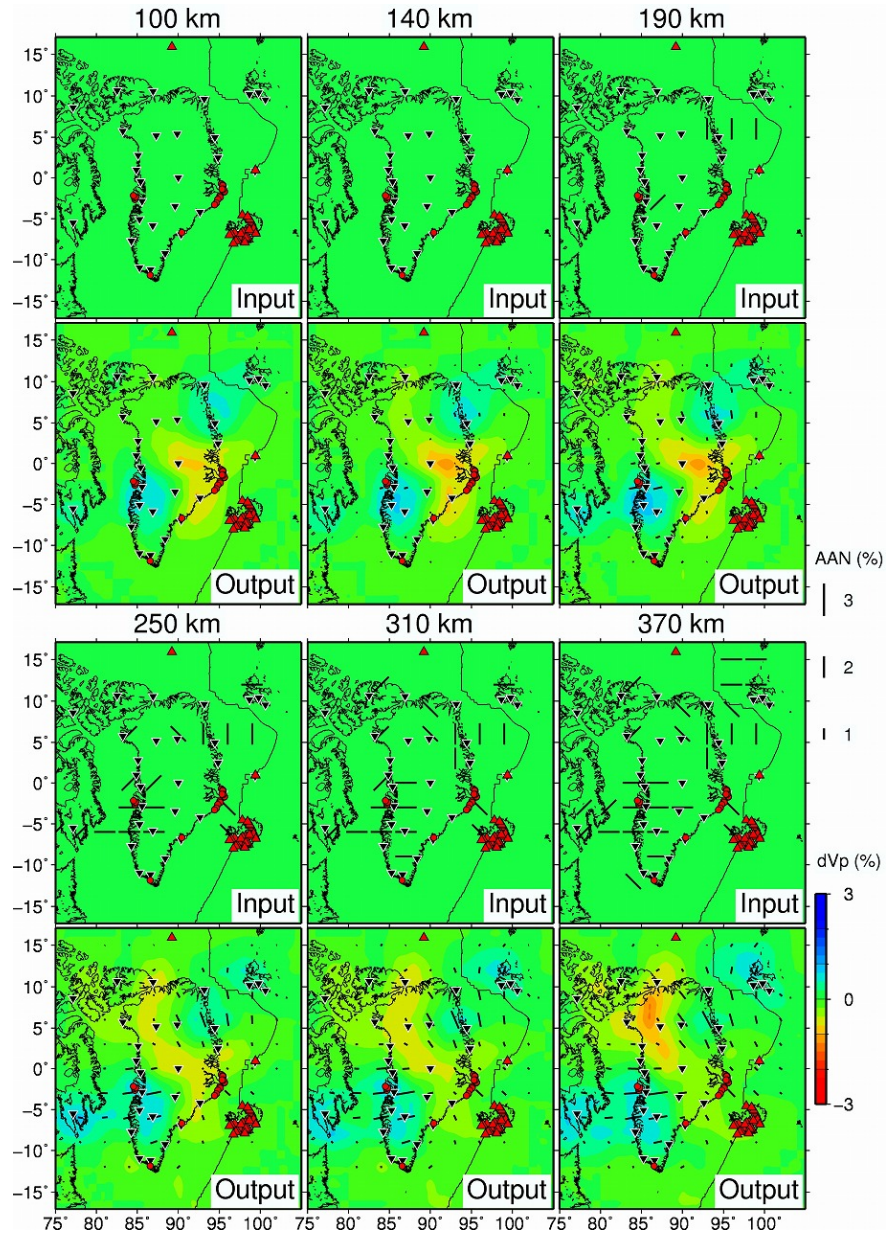


Figure S18. Same as Figure S16 but for the AAN-TOT2 (Table 1) (TOT: trade-off test; see text for details).

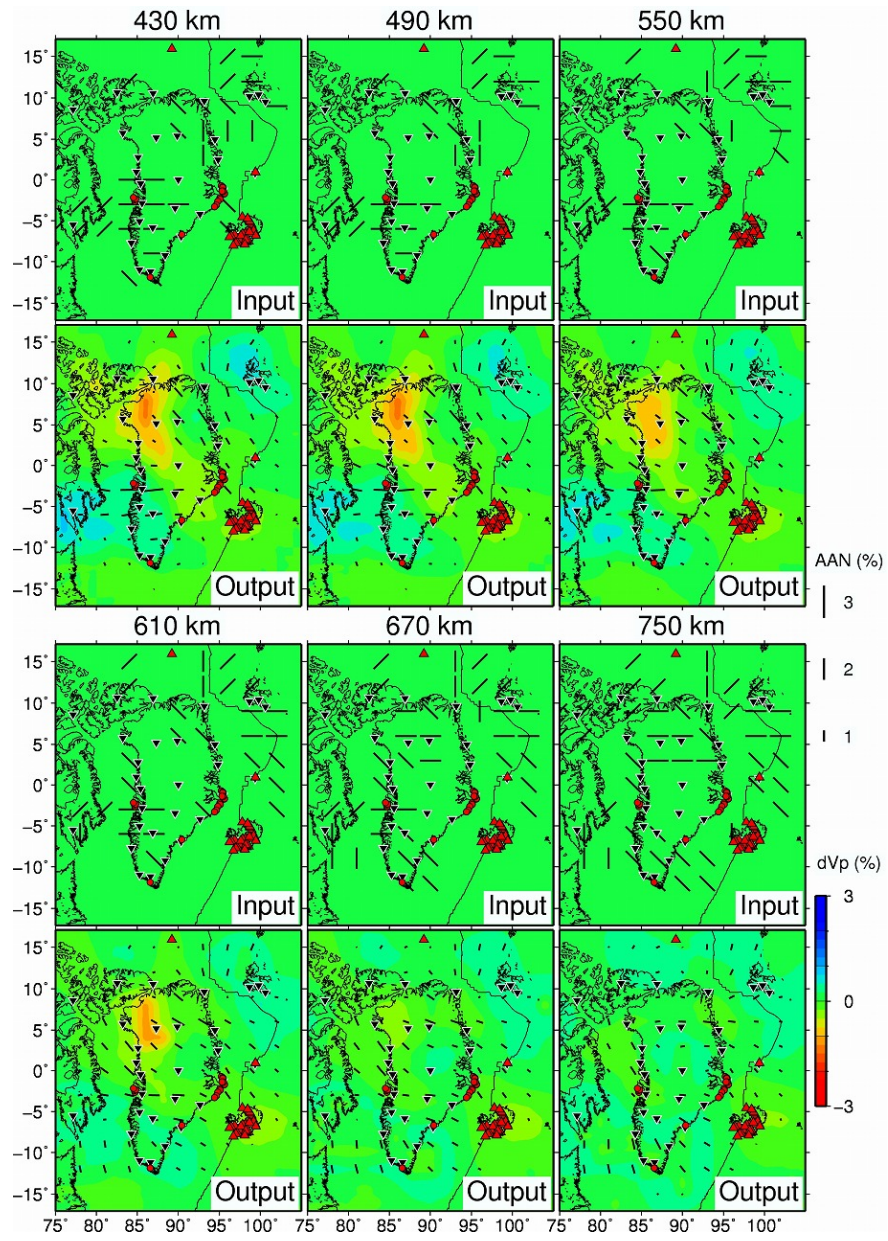


Figure S18. (continued).

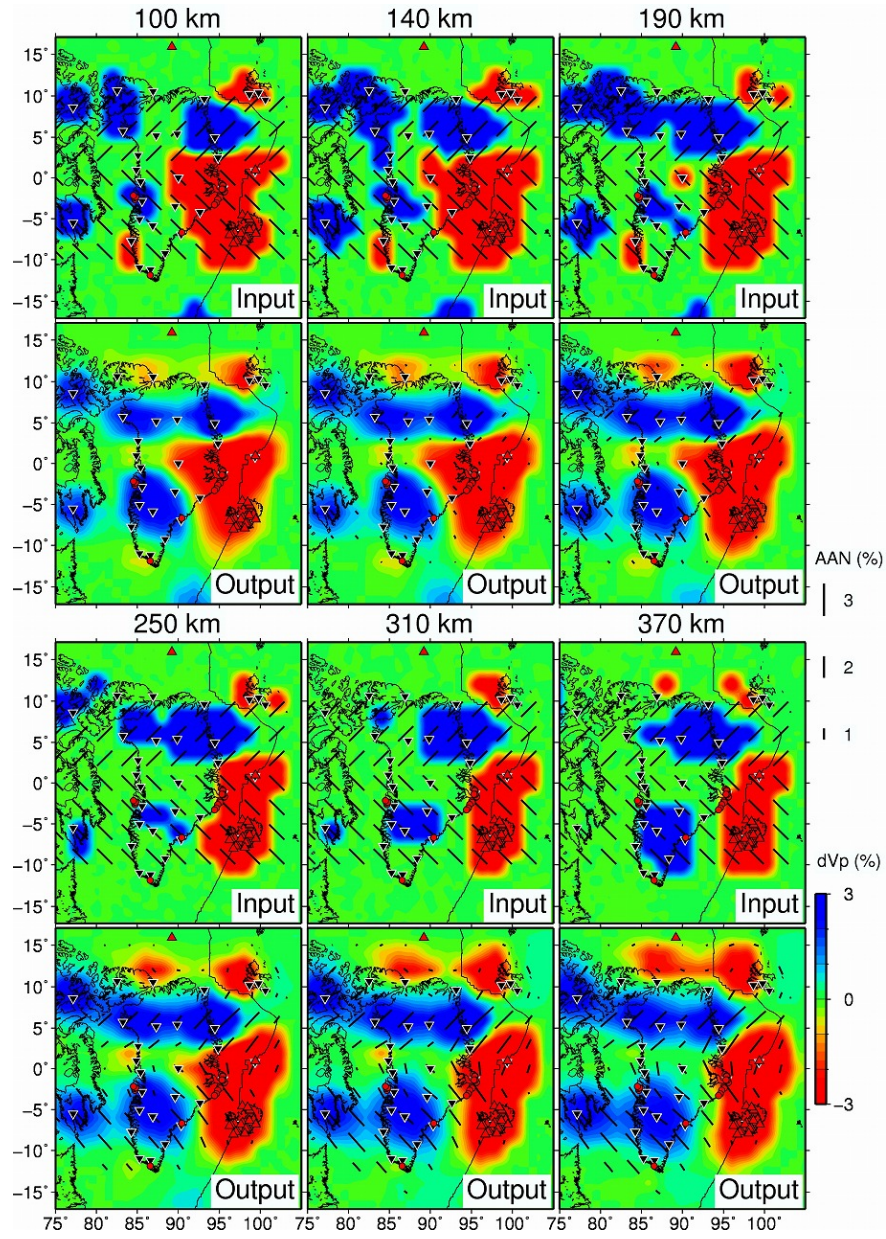


Figure S19. Same as Figure S16 but for the AAN-SRT1 (Table 1) (SRT: synthetic resolution test; see text for details).

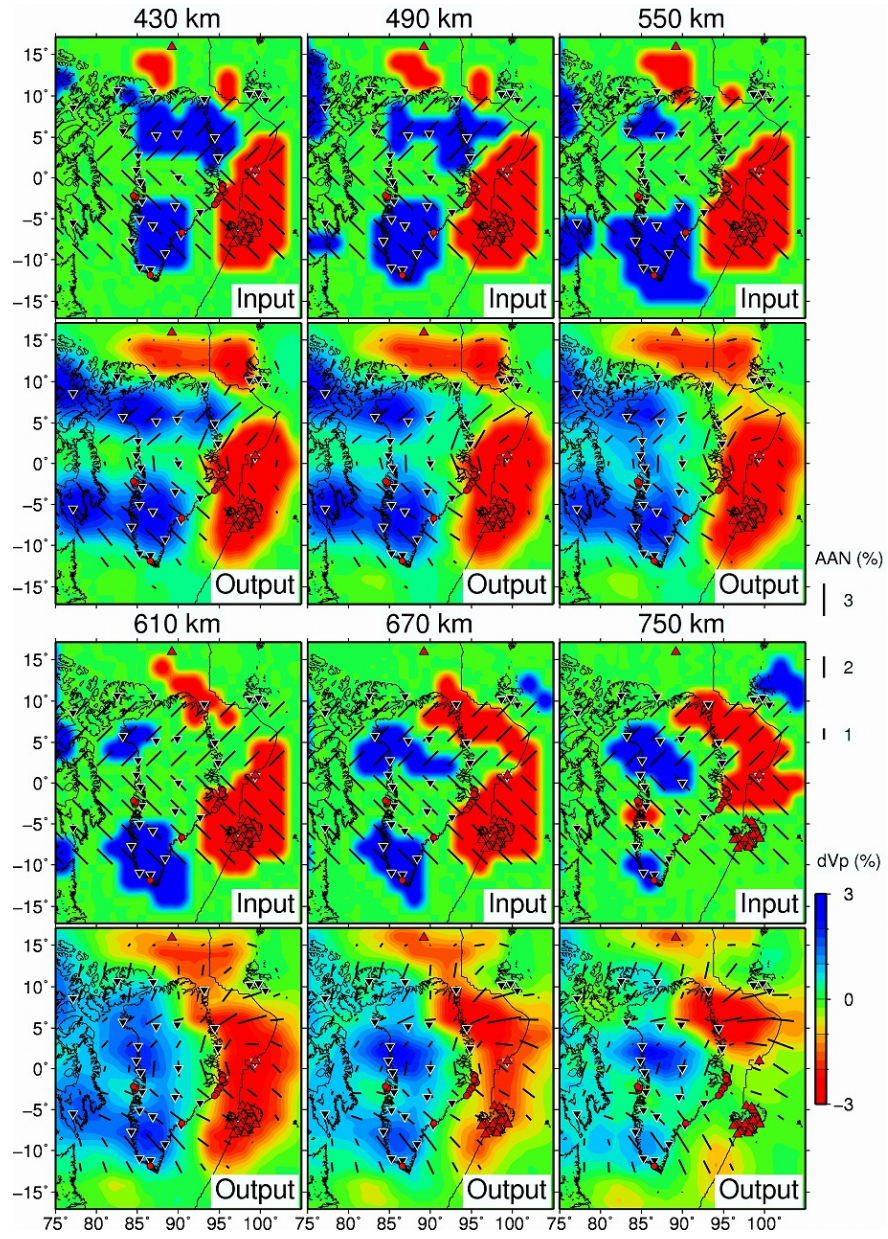


Figure S19. (continued).

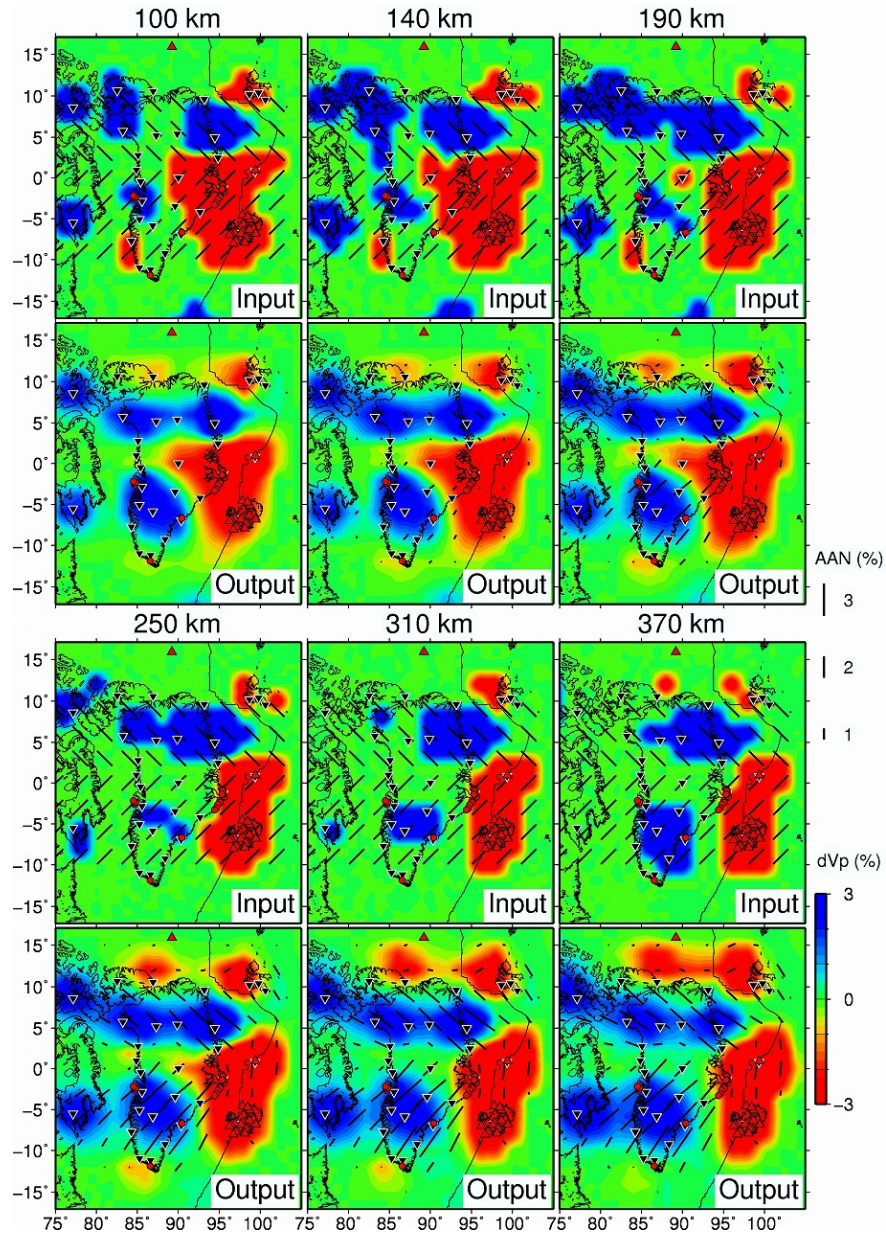


Figure S20. Same as Figure S16 but for the AAN-SRT2 (Table 1) (SRT: synthetic resolution test; see text for details).

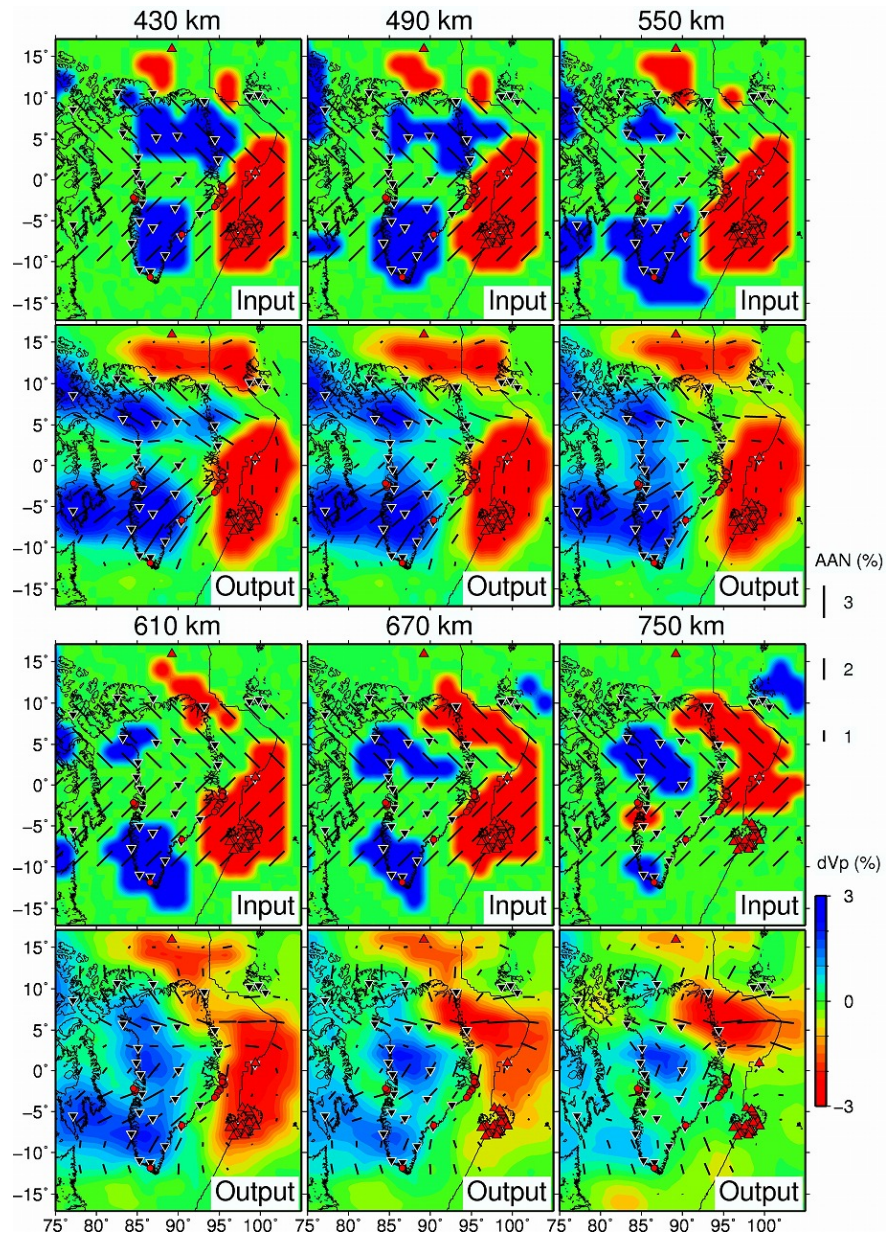


Figure S20. (continued).

References

- Kennett, B. L. N., & Engdahl, E. R. (1991). Traveltimes for global earthquake location and phase identification. *Geophysical Journal International*, 105, 429–465. <https://doi.org/10.1111/j.1365-246X.1991.tb06724.x>
- Toyokuni, G., Matsuno, T., & Zhao, D. (2020a). *P* wave tomography beneath Greenland and surrounding regions: 1. Crust and upper mantle. *Journal of Geophysical Research: Solid Earth*, 125, e2020JB019837. <https://doi.org/10.1029/2020JB019837>

1
2
3
4
5
6
7
8
9
10
11
12
13
14
15
16
17
18
19

***P* wave tomography for 3-D radial and azimuthal anisotropy beneath Greenland and surrounding regions**

Genti Toyokuni^{1*} and Dapeng Zhao¹

¹ Department of Geophysics, Graduate School of Science, Tohoku University, Sendai 980-8578, Japan

Submitted to *Tectonics* in March 2021

*Corresponding author:

Genti Toyokuni

E-mail: toyokuni@tohoku.ac.jp

ORCID ID: 0000-0003-3786-207X

Key Points:

- 3-D *P*-wave radial and azimuthal anisotropy structure of the upper mantle beneath Greenland and surrounding regions is investigated.
- The presence of upper-mantle plumes beneath Iceland, Jan Mayen, and Svalbard hotspots is confirmed from seismic anisotropy.
- A new scenario for the breakup between Greenland and Canada is proposed.

20 **Abstract**

21 We present the first 3-D images of *P*-wave radial anisotropy (RAN) and azimuthal anisotropy
22 (AAN) down to 750-km depth beneath Greenland and surrounding regions. The results are
23 obtained by applying a regional tomographic method to simultaneously invert *P* wave arrival
24 times of 1,309 local events and *P* wave relative traveltimes residuals of 7,202 teleseismic events,
25 which were recorded mainly by the latest GLISN network. A high-velocity body located beneath
26 northeast Greenland (NEG) to its offshore exhibits a strong negative RAN and a strong AAN
27 with N-S to NE-SW oriented fast-velocity directions (FVDs). The FVDs are generally consistent
28 with the direction of the fold axis of the Caledonian fold belt, which is considered as an outcrop
29 of the NEG body on land. Beneath the Iceland, Jan Mayen, and Svalbard hotspots, a strong
30 positive RAN and a negligible or weak AAN are revealed, which may reflect effects of
31 upwelling mantle plumes. Among the three regions, a weak AAN with a constant FVD is only
32 revealed beneath Iceland, which may reflect the existence of background mantle flow. The RAN
33 and AAN features beneath the Labrador Sea, Davis Strait, and Baffin Bay suggest the following
34 scenario on breakup between Greenland and Canada: the breakup was initiated at the Labrador
35 Sea due to local mantle upwelling, but the northward propagation of the breakup was blocked by
36 a strong high-velocity anomaly beneath Davis Strait; the opening of Baffin Bay might be caused
37 passively by far-field plate forces.

38 **1. Introduction**

39 Greenland is the largest island in the world whose land area spans over 20° in the central
40 angle of the Earth. The surface-exposed rocks have preserved ~4 billion years of Earth's history
41 in the oldest part (Henriksen et al., 2009). However, the Greenland Ice Sheet (GrIS), covering
42 80% of the land area, has long been preventing the geological study in the inland area. Greenland

43 itself has low seismic activity and no known active volcanoes, but there are several hot springs
44 on the east and west coasts of Greenland (Hjartarson & Armannsson, 2010) that coincide with
45 Tertiary basalt outcrops. The Mid-Atlantic Ridge (MAR) is located on the eastern side of
46 Greenland, where the North American plate and the Eurasian plate separate from each other,
47 inducing very active seismicity. There are also three major hotspots (Iceland, Jan Mayen, and
48 Svalbard) along the MAR, highlighting the tectonic activity of this region. Turning our eyes to the
49 western side of Greenland, Baffin Bay, Davis Strait, and Labrador Sea separate Greenland and
50 Canada (Figure 1).

51 Currently, 34 seismic stations, including four on the GrIS, are in operation in and around
52 Greenland by the Greenland Ice Sheet monitoring Network (GLISN) launched in 2009 (Clinton
53 et al., 2014; Toyokuni et al., 2014). Seismological studies using the GLISN data have been made
54 actively (e.g., Darbyshire et al., 2018; Lebedev et al., 2017; Levshin et al., 2017; Mordret, 2018;
55 Mordret et al., 2016; Pourpoint et al., 2018; Rickers et al., 2013; Toyokuni et al., 2015, 2018,
56 2020a, 2020b, 2021), but only a few of them focused on the mantle structure using body wave
57 data (Rickers et al., 2013; Toyokuni et al., 2020a, 2020b).

58 Toyokuni et al. (2020a) conducted, for the first time, the detailed body wave (P wave)
59 tomography in and around Greenland to investigate the 3-D P -wave velocity (V_p) structure down
60 to 700-km depth. Their results are summarized as follows. (1) In the upper mantle beneath the
61 Iceland, Jan Mayen and Svalbard hotspots, there are Iceland plume, Jan Mayen plume, and
62 Svalbard plume, respectively, which extend almost vertically down to the mantle transition zone
63 (MTZ) where the three plumes merge together. (2) A low- V_p anomaly, elongating in the NW-SE
64 direction, was revealed at depths ≤ 250 km beneath central Greenland, forming the central
65 Greenland lithospheric low-velocity zone (CGLLVZ). The CGLLVZ is interpreted as a

66 polymerization of ancient Iceland and Jan Mayen plume tracks due to plate movement. (3) A
67 high- V_p body was revealed at depths ≤ 500 km off the northeastern coast of Greenland. This
68 body seems continuous to the Caledonian fold belt in northeast Greenland, and so was
69 interpreted as a remnant of oceanic lithosphere constituted the Iapetus Ocean, closed 490–390
70 Ma, due to collision of Laurentia and Baltica (Henriksen et al., 2009; Metelkin et al., 2015). This
71 body is located inside the bend of MAR that is thought to have existed at the time of the North
72 Atlantic opening (Thiede et al., 2011); therefore, this body may have restricted the mode of plate
73 expansion. Furthermore, this body seems to act as an obstacle separating flows of the Jan Mayen
74 and Svalbard plumes. Hereinafter, we call it the “Northeast Greenland (NEG) body.”

75 Now that the static structural features described above have been revealed, we are
76 interested in dynamic features of the region. Seismic anisotropy shows a direction-dependent
77 nature of the Earth’s material on seismic wave propagation, which is widely revealed from the
78 crust and mantle to the inner core (Long & Becker, 2010). Seismic anisotropy in the mantle is
79 generally induced by the lattice-preferred orientation (LPO) of olivine. There are several olivine
80 types (A-, B-, C-, D-, and E-types) in the upper mantle, which exhibit different relationships
81 between the anisotropic structure and the dominant slip system. However, these olivine fabrics
82 except for B-type exhibit a fast axis parallel to the mantle flow direction (Karato et al., 2008).
83 The B-type olivine only appears in an environment of high-stress, low-temperature, and water-
84 rich conditions (Katayama & Karato, 2006).

85 So far, only a few studies have investigated seismic anisotropy in Greenland, Iceland, and
86 surrounding regions, using surface wave tomography (Darbyshire et al., 2018), shear-wave
87 splitting (SWS) measurements (Bjarnason et al., 2002; Ucisik et al., 2005, 2008), and numerical
88 modeling of mantle flow (Marquart et al., 2007). Darbyshire et al. (2018) conducted surface

89 wave tomography to investigate azimuthal anisotropy of Rayleigh-wave group velocity in the
90 crust and uppermost mantle beneath Greenland. However, the depth they analyzed was limited to
91 $< \sim 100$ km due to the frequency band of the Rayleigh wave. Measuring SWS is a popular method
92 to obtain the azimuthal fast-polarization orientation (FPO) and time delay of the medium directly
93 beneath a station using, for example, *SKS* and *SKKS* phases that have rays close to the vertical
94 direction. The depth range of the medium that provides FPO can be estimated from the degree of
95 time delay, but the depth resolution is not good. To date, there has been no study of the 3-D
96 anisotropic structure beneath Greenland and its surrounding regions using body waves that
97 penetrate deeply into the mantle and so have a good depth resolution.

98 Seismic anisotropy tomography using body waves is the updated method to constrain 3-D
99 images of both radial anisotropy (RAN) and azimuthal anisotropy (AAN) of the subsurface
100 structure (e.g., Ishise & Oda, 2005; Wang & Zhao, 2008, 2013; Zhao, 2015). This method has
101 been applied to various regions in the world, for example, Japan (Ishise & Oda, 2005; Liu &
102 Zhao, 2017; Wang & Zhao, 2021), Alaska (Gou et al., 2019), and Southeast Asia (Huang et al.,
103 2015). However, it has been rarely applied to areas where a mid-ocean ridge or a mantle plume
104 exists, except for the Erebus hotspot in Antarctica (Zhang et al., 2020). The purpose of this study
105 is to determine the first 3-D *P*-wave RAN and AAN model of the upper mantle beneath the study
106 region (Figure 2a) by analyzing the GLISN data to improve our understanding of the subsurface
107 structure and mantle dynamics of this region.

108 **2. Method**

109 We apply a regional tomography method to *P*-wave travel-times from both local and
110 teleseismic events (Zhao et al., 1994, 2012; Toyokuni et al., 2020a). For the local events, we use
111 travel-time residuals (t_{ij}):

112

$$t_{ij} = T_{ij}^{\text{OBS}} - T_{ij}^{\text{CAL}} \quad (1)$$

113

114 where T_{ij}^{OBS} and T_{ij}^{CAL} are observed and calculated (theoretical) arrival times, respectively,
 115 from the i th event to the j th station. For the teleseismic events, we use relative travel-time
 116 residuals (r_{ij}):

117

$$r_{ij} = t_{ij} - \bar{t}_i$$

$$\bar{t}_i = \frac{1}{n_i} \sum_{j=1}^{n_i} t_{ij} \quad (2)$$

118

119 where n_i is the number of recording stations of the i th event, and \bar{t}_i is the average of travel-time
 120 residuals at the n_i stations. Note that \bar{t}_i includes the influence of structural heterogeneity outside
 121 the study volume as well as errors in the hypocentral parameters. In the tomographic inversion,
 122 we only consider the teleseismic ray segments that are located within the study volume.

123 We conduct tomographic inversions for 3-D P -wave RAN and AAN using the method of
 124 [Wang & Zhao \(2008, 2013\)](#). In a RAN medium, the symmetry axis is assumed to be in the
 125 vertical direction, and one parameter is added to express anisotropy. The total slowness (S) due
 126 to RAN can be written as

127

$$S = \frac{1}{V_{P0}} (1 + M \cos 2i) \quad (3)$$

128

129 where V_{P0} is isotropic P -wave velocity, M is the strength of anisotropy, and i is the ray path
 130 incident angle ([Wang & Zhao, 2008](#)). The amplitude of RAN α can be represented as

131

$$\alpha = \frac{V_{Ph} - V_{Pv}}{2V_{P0}} = \frac{M}{1 - M^2} \quad (4)$$

132

133 where V_{Ph} and V_{Pv} are P -wave velocities in the horizontal and vertical directions, respectively.

134 Therefore, positive values of α represent that the horizontally propagating P -wave travels faster
135 than the vertically propagating one ($V_{Ph} > V_{Pv}$), and vice versa.

136 In an AAN medium, the symmetry axis is assumed to be in a horizontal plane, and two
137 parameters are adopted to express AAN. The total slowness (S) due to AAN can be written as

138

$$S = \frac{1}{V_{P0}} [1 + A \cos 2\phi + B \sin 2\phi] \quad (5)$$

139

140 where A and B are two azimuthal anisotropy parameters, and ϕ is the ray path azimuth (Wang &
141 Zhao, 2013). The amplitude of AAN β and fast velocity direction (FVD) ψ can be expressed as

142

$$\beta = \frac{V_{Pf} - V_{Ps}}{2V_{P0}} = \frac{\sqrt{A^2 + B^2}}{1 - (A^2 + B^2)^2} \quad (6)$$

143

$$\psi = \begin{cases} \frac{1}{2} \tan^{-1} \left(\frac{B}{A} \right) + \begin{cases} \frac{\pi}{2} & (A > 0) \\ 0 & (A < 0) \end{cases} \\ -\frac{\pi}{4} & (A = 0, B > 0) \\ \frac{\pi}{4} & (A = 0, B < 0) \end{cases} \quad (7)$$

144

145 where V_{Pf} and V_{Ps} are P -wave velocities in the fast and slow directions, respectively.

146 We first determine a 3-D isotropic V_p model using the seismic tomography method of
147 [Zhao et al. \(1994, 2012\)](#), which discretizes the study volume using a 3-D grid. We conduct
148 global coordinate transformation of the study region by moving its center to the equator
149 ([Takenaka et al., 2017; Toyokuni et al., 2020a](#)), so that we can set 3-D grid nodes for the
150 tomographic inversion uniformly both in the latitude and longitude directions. Following
151 [Toyokuni et al. \(2020a\)](#), we move the station SUMG (longitude, latitude) $=(-38.461^\circ, 72.574^\circ)$
152 on the GrIS summit to a point on the equator $(90^\circ, 0^\circ)$. We then arrange 2-D grid meshes in the
153 area between 70° and 120° longitude and -20° and 20° latitude, after the coordinate
154 transformation ([Figure 2a](#)). For the isotropic 3-D V_p structure (V_{p0}), we adopt a horizontal grid
155 interval of 2° in both latitude and longitude directions, and the 2-D grid meshes are set at depths
156 of 5, 20, 40, 60, 80, 100, 120, 140, 160, 190, 220, 250, 280, 310, 340, 370, 400, 430, 460, 490,
157 520, 550, 580, 610, 640, 670, 700, 750, 800, 850, and 900 km ([Figure S1a](#)). For the V_p
158 anisotropic components (M for the RAN, or A and B for the AAN), we adopt a horizontal grid
159 interval of 3° in both latitude and longitude directions, and 2-D grid meshes are set at depths of 5,
160 20, 60, 100, 140, 190, 250, 310, 370, 430, 490, 550, 610, 670, and 750 km ([Figure S1b](#)). Note
161 that, to solve the anisotropic components at the grid nodes, we need seismic rays from various
162 directions with a sufficient density. Hence, we set the grid nodes for the anisotropy coarser than
163 those for solving the isotropic component. Tomographic inversions for the 3-D RAN and AAN
164 structures are conducted separately because of the different assumptions on the symmetry axis
165 for RAN and AAN.

166 Theoretical travel times are calculated by using a 3-D ray tracing technique that combines
167 the pseudo-bending scheme ([Um & Thurber, 1987](#)) and Snell's law ([Zhao et al., 1992](#)). The
168 initial 1-D model for the isotropic component is shown in [Figure S2](#). The initial values of the

169 anisotropic parameters are set to zero. The Conrad and Moho depths are fixed at 20 and 40 km,
170 respectively. We conduct the tomographic inversions using the LSQR algorithm (Paige &
171 Saunders, 1982) with damping and smoothing regularizations (Zhao et al., 1992, 1994, 2012;
172 Wang & Zhao, 2008, 2013).

173 3. Data

174 The data used in this study are the updated version of those used in Toyokuni et al.
175 (2020a). We first downloaded all P -wave arrival time data of $M \geq 3$ earthquakes observed at 33
176 GLISN stations and one temporary station (station code: IC-GL) on the GrIS during January
177 1964 to December 2016 from the ISC-EHB catalog (<http://www.isc.ac.uk/isc-ehb/>). To extract
178 local earthquake data, the coordinate transformation (Section 2) is first applied to all the
179 epicenters and station locations. Earthquakes that occurred between 70° and 120° longitude, and
180 -20° and 20° latitude were then extracted as local earthquakes. All earthquakes recorded at one
181 or more stations were extracted. As a result, 2,414 P -wave arrival times from 1,288 local events
182 were obtained (Figure 2a). The magnitudes of these extracted events range from 3.1 to 7.1, with
183 focal depths between 0.0 and 31.5 km. To extract teleseismic events, earthquakes with epicentral
184 distances between 30° and 100° and recorded at five or more stations in the study region were
185 extracted. As a result, 51,578 P -wave arrival times from 7,088 teleseismic events were obtained.

186 We then manually picked 781 P -wave and 541 S -wave arrival times from 43 local events
187 recorded at 34 GLISN stations from waveforms downloaded from the IRIS/DMC
188 (<https://ds.iris.edu/ds/nodes/dmc/>) (Figures S3 and S4). We relocated the 43 events using both P -
189 and S -wave arrival times, and extracted those events with five or more data with absolute travel-
190 time residuals within ± 3 s for both P - and S -wave data, and with uncertainty of the focal depth \leq

191 20 km. After this processing, 407 *P*-wave arrival times from 21 local events remain in the data
192 set (Figure 2a). The *S*-wave data are not used in the subsequent analysis.

193 We also added teleseismic *P*-wave relative arrival-time data picked by Toyokuni et al.
194 (2020a), which contain 7,573 picks from 347 teleseismic events that occurred from January 1,
195 2012 to July 15, 2019. When the event overlaps with those in the ISC catalog, the ISC data are
196 removed. As a result, we obtained 56,498 *P*-wave arrival times ($51,578 - 2,653 + 7,573$) from
197 7,231 teleseismic events ($7,088 - 204 + 347$). We then applied crustal correction to the
198 teleseismic data according to the method of Jiang et al. (2009a, 2009b, 2015) and Toyokuni et al.
199 (2020a). Figures S5a and S5b show the distributions of the relative travel-time residuals
200 averaged at each station for all events, both before and after the crustal correction. During the
201 process, any teleseismic data with relative travel-time residuals exceeding ± 3 s are further
202 discarded. As a result, the number of teleseismic events and the number of relative travel-time
203 residuals are 7,202 and 55,917, respectively, before the crustal correction, and 7,202 and 55,768,
204 respectively, after the correction (Figure 2b). The final dataset used for our tomographic
205 inversions includes these teleseismic data and 2,821 *P*-wave arrival times ($2,414 + 407$) from
206 1,309 local earthquakes ($1,288 + 21$) obtained from the ISC-EHB catalog and our manual
207 picking. Figure S6 shows the distribution of the local and teleseismic rays used in this study.

208 **4. Results**

209 **4.1 Isotropic tomography**

210 We first conduct a tomographic inversion for the 3-D isotropic V_p structure with exactly
211 the same grid and parameter settings as Toyokuni et al. (2020a) using our new data set. Map
212 views and vertical cross-sections of the results are shown in Figure S7, and Figures S8–S9,

213 respectively. All the features described in [Section 1](#) are well visible in these results, confirming
 214 the robustness of the images obtained by the isotropic V_p tomography.

215 **4.2 Radial anisotropy (RAN)**

216 [Figure 3](#) shows map views of the obtained RAN tomography. Focusing on the isotropic
 217 component, the NEG body is clearly imaged as the most prominent high-velocity (high- V_{p0})
 218 region at depths ≤ 490 km beneath the northeastern coast of Greenland to the northeastern
 219 offshore. High- V_{p0} anomalies are also visible from northwestern Greenland to Ellesmere Island
 220 at depths ≤ 490 km, and beneath the southern tip of Greenland at depths ≥ 430 km. The most
 221 prominent low-velocity (low- V_{p0}) anomalies are related to hotspots beneath Iceland, Jan Mayen,
 222 and Svalbard from the surface down to 610 km depth. At depths ≤ 250 km, a low- V_{p0} anomaly is
 223 also visible beneath inland Greenland elongated in the NW-SE direction and extend to the
 224 Iceland and Jan Mayen hotspots (the CGLLVZ). These isotropic V_p features are in very good
 225 agreement with the previous results of isotropic tomography ([Toyokuni et al., 2020a](#) and [Section](#)
 226 [4.1](#)), although the anisotropic tomography is obtained by stronger smoothing, and so the features
 227 are much blunt.

228 Regarding the anisotropic features, reliable results are obtained at depths of 190–550 km
 229 according to the resolution tests shown in the followings. The most prominent negative RAN
 230 ($\alpha < 0$, i.e., $V_{ph} < V_{pv}$, as shown in vertical bars in [Figure 3](#)) can be seen beneath the NEG body.
 231 Weak negative RAN is also found along the coast of western Greenland at depths ≤ 310 km, but
 232 nothing else is prominent. In contrast, positive RAN ($\alpha > 0$, i.e., $V_{ph} > V_{pv}$, as shown in
 233 horizontal bars in [Figure 3](#)) can be found at all depths and in various parts of the study region.
 234 The most notable ones are located in the low-V zones just beneath the Iceland, Jan Mayen, and
 235 Svalbard hotspots. There is another remarkable positive RAN beneath Davis Strait and the

236 Labrador Sea at depths ≤ 490 km, but no significant anisotropy is found beneath Baffin Bay. No
 237 significant anisotropy is observed in the low- V_{P0} zone running in the NW-SE direction beneath
 238 central Greenland at depths ≤ 250 km, and in the high- V_{P0} zone beneath the southern tip of
 239 Greenland at depths ≥ 430 km.

240 Vertical cross-sections are shown in [Figures 4 and 5](#). In the cross-sections through
 241 Iceland, Jan Mayen, and Svalbard (e.g., J-J' and K-K' sections in [Figure 4a](#)), a low- V_{P0} anomaly
 242 extending from the mantle transition zone (MTZ) and a strong positive RAN ($V_{Ph} > V_{Pv}$) are
 243 remarkable. A strong negative RAN ($V_{Ph} < V_{Pv}$) in the high- V_{P0} body in the upper mantle
 244 between Jan Mayen and Svalbard is also characteristic. In the cross-sections from Iceland to
 245 central Greenland (e.g., C-C' sections in [Figure 5a](#)), the low- V_{P0} zone suddenly thins to a depth \leq
 246 250 km when entering the Greenland side beyond Denmark Strait, and a positive RAN ($V_{Ph} >$
 247 V_{Pv}) weakens in the thinned low- V_{P0} zone. The upper mantle beneath the Labrador Sea is
 248 characterized by a weak low- V_{P0} anomaly and a moderate positive RAN ($V_{Ph} > V_{Pv}$). Overall,
 249 the characteristics of the isotropic component are in good agreement with the results of isotropic
 250 tomography. However, in the anisotropic tomography, the grid is coarse and the smoothing is set
 251 to be strong, so the resolution becomes lower. For example, the Iceland plume and the Jan
 252 Mayen plume are not separated, and the CGLLVZ looks thicker than that in the isotropic
 253 tomography.

254 **4.3 Azimuthal anisotropy (AAN)**

255 [Figure 6](#) shows map views of the obtained AAN tomography. Regarding the anisotropic
 256 features, reliable results are obtained at depths of 190–550 km according to the resolution tests
 257 shown in the followings. The regions with marked AAN at depths ≤ 430 km are the interior of
 258 the NEG body and the region beneath Davis Strait to southwestern Greenland. The NEG body

259 corresponds well to the strong AAN that exhibits N-S to NW-SE FVDs. On the other hand, the
260 AAN in southwestern Greenland does not clearly correspond to the high- V_{p0} anomaly, and the
261 predominant FVDs are NE-SW to E-W. No significant AAN is seen in central Greenland, which
262 appears to separate these two regions. Even at depths of 490 and 550 km, the overall
263 characteristics do not change largely. The NEG body is obscured, but the AAN still remains,
264 exhibiting N-S to NE-SW FVDs. The predominant FVD in southwestern Greenland is E-W. No
265 strong AAN appears beneath the Iceland, Jan Mayen, and Svalbard hotspots. However, only
266 beneath Iceland, a weak AAN with N-S to NW-SE FVDs occurs at depths of 190–550 km.

267 Vertical cross-sections are shown in [Figures 7 and 8](#). The characteristics of the isotropic
268 component are almost the same as those of RAN tomography. In the cross-sections through
269 Iceland, Jan Mayen, and Svalbard (e.g., [J-J'](#) and [K-K'](#) sections in [Figure 7a](#)), a weak AAN with
270 NNW-SSE FVDs appears at depths ≤ 600 km beneath Iceland, but the AAN is hardly seen
271 beneath Jan Mayen and Svalbard. The high- V_{p0} body in the upper mantle between Jan Mayen
272 and Svalbard has a remarkable AAN with N-S to NE-SW FVDs. In the cross-sections from
273 Iceland to central Greenland (e.g., [C-C'](#) sections in [Figure 8a](#)), the AAN weakens in the thinned
274 low- V_{p0} zone beneath central Greenland. In the cross-sections through Baffin Island and western
275 Greenland, a moderate AAN with NE-SW FVD is predominant in the upper mantle beneath
276 Davis Strait, which continues to a region beneath the west coast of Greenland. The similar AAN
277 seems to extend to a region beneath Baffin Island, but here N-S FVDs are more predominant.
278 Going further south and looking at the cross-sections through the Labrador Sea, the AAN
279 weakens in and around the low- V_{p0} zone at depths ≤ 300 km, but a stronger AAN with E-W
280 FVDs becomes prominent at depths of 300–500 km.

281 After making many tomographic inversions, the number of iterations is set to three for
282 both the RAN and AAN tomography, and the damping parameters in the 1st, 2nd, and 3rd
283 iterations are set to 20, 50, and 100, respectively. The smoothing parameter is set to 20,000 for
284 both the isotropic and anisotropic components in the RAN and AAN tomography. For
285 comparison, we conducted another inversion for only the isotropic component with the same
286 parameters and grid settings (Figures S10–S12). The final root-mean-square (RMS) travel-time
287 residual is 0.648 s after the inversion for only the isotropic component, 0.616 s for RAN, and
288 0.607 s for AAN, indicating that the 3-D velocity model fits the data better when anisotropy is
289 included in the inversion (Figure 9).

290 **5. Resolution tests**

291 We conducted many resolution tests, including restoring resolution tests (RRTs) (Zhao et
292 al., 1992), trade-off tests (TOTs), and synthetic resolution tests (SRTs), to evaluate the ray
293 coverage and spatial resolution of our models.

294 For the RAN tomography, three tests (RAN-RRT, RAN-TOT1, and RAN-TOT2, see
295 Table 1) are conducted. The RAN-RRT is the RRT that highlights the patterns in the main RAN
296 tomographic results when constructing the input model. To create the input model for the
297 isotropic component, at grid nodes with V_{P0} anomalies $> +0.6\%$ or $< -0.6\%$ in the RAN
298 tomographic results, constant V_{P0} anomalies of $+3\%$ or -3% are assigned. For the anisotropic
299 component, at grid nodes with $\alpha > +1.0\%$ or $< -1.0\%$ in the RAN tomographic results, constant
300 α of $+2\%$ or -2% are assigned. The isotropic V_P perturbation and anisotropy at the other grid
301 nodes are set to zero. The RAN-TOT1 is a TOT to examine the trade-off between isotropic V_P
302 and anisotropy, and its input model contains only the isotropic component. The RAN-TOT2 is

303 another TOT to examine the trade-off, but its input model contains only the anisotropic
304 component.

305 For the AAN tomography, five tests (AAN-RRT, AAN-TOT1, AAN-TOT2, AAN-SRT1,
306 and AAN-SRT2, see [Table 1](#)) are conducted. The AAN-RRT is a RRT that highlights the
307 patterns in the main AAN tomographic results when constructing the input model. To create the
308 input model for the isotropic component, at grid nodes with V_{p0} anomalies $> +0.6\%$ or $< -0.6\%$
309 in the main AAN tomographic results, we assign constant V_{p0} anomalies of $+3\%$ or -3% . For the
310 anisotropic component, at grid nodes with $\beta > +1.0\%$ or $< -1.0\%$ in the AAN tomographic
311 results, we assign constant β of $+2\%$ or -2% . As for the FVD, at the grid nodes where FVD is in
312 the range from -45.0° to -22.5° , from -22.5° to 22.5° , from 22.5° to 67.5° , from 67.5° to 112.5° ,
313 and from 112.5° to 135.0° in the main AAN tomographic results, we assign a constant value of
314 -45.0° , 0.0° , 45.0° , 90.0° , and -45.0° , respectively, in the RRT input model. The isotropic V_p
315 perturbation and anisotropy at the other grid nodes are set to zero. As in the case of RAN
316 tomography, AAN-TOT1 and AAN-TOT2 are performed to examine the trade-off from isotropic
317 V_p to anisotropy and from anisotropy to isotropic V_p , respectively. The AAN-SRT1 and AAN-
318 SRT2 are two SRTs whose input model contains synthetic anisotropic anomalies, whereas its
319 isotropic component is the same as that in the AAN-RRT input model.

320 Synthetic data sets for all the RRT, TOT, and SRT inversions for both the RAN and AAN
321 cases are constructed by calculating theoretical arrival times for each input model but with
322 random errors added, which range between -0.3 and $+0.3$ s with a standard deviation of 0.1 s.
323 Main features of the test results are summarized in [Figures 10 and 11](#) for the RAN and AAN
324 cases, respectively. Details of the test results are shown in supporting information for the RAN-

325 RRT (Figure S13), RAN-TOT1 (Figure S14), RAN-TOT2 (Figure S15), AAN-RRT (Figure S16),
326 AAN-TOT1 (Figure S17), AAN-TOT2 (Figure S18), AAN-SRT1 (Figure S19), and AAN-SRT2
327 (Figure S20).

328 Regarding the RAN-RRT results (Figures 10a and S13), due to strong smoothing in the
329 inversion of this study, both isotropic and anisotropic components spread more widely than those
330 in the input model. However, main features of both the isotropic and anisotropic components are
331 generally recovered at depths of 100–750 km, although the recovery of anisotropic component is
332 slightly worse at depths of 670 and 750 km. Regarding the RAN-TOT1 results (Figures 10b and
333 S14), the isotropic component is well recovered at all depths. On the other hand, exudation from
334 the isotropic to anisotropic component can be confirmed at depths of 190–490 km. However, the
335 pattern of anisotropy is different from that of the main RAN tomographic results (Figure 3), and
336 the maximal intensity of anisotropy is about 60% of those for the RAN-RRT case, so the
337 influence of trade-off on the tomographic result is considered to be small. Regarding the RAN-
338 TOT2 results (Figures 10c and S15), the anisotropy pattern is well recovered at depths ≤ 670 km,
339 and there is almost no leakage from the anisotropy to isotropic V_p .

340 Similar to the RAN case, the effect of smoothing can be seen in the AAN-RRT results
341 (Figures 11a and S16), but the characteristics of both isotropic and anisotropic components can
342 be recovered well at depths of 100–750 km. The AAN-TOT1 results (Figures 11b and S17)
343 show that the isotropic components are well recovered at all depths. The leakage from the
344 isotropic to anisotropic components becomes remarkable at depths ≥ 610 , but the intensity is
345 weak at other depths, and the pattern is also significantly different from that of the main AAN
346 tomographic results. Regarding the AAN-TOT2 results (Figures 11c and S18), the anisotropic
347 characteristics are well recovered at depths ≤ 610 km, and there is almost no leakage from the

348 anisotropic to isotropic components. The AAN-SRT1 (Figures 11d and S19) and AAN-SRT2
349 (Figures 11e and S20) results show that the pattern of isotropic component is slightly distorted
350 by the strong artificial anisotropic components. However, the intensity of anisotropy and FVDs
351 are well recovered in both cases at depths of 100–550 km. In particular, the input FVDs in the
352 AAN-SRT1 case are well recovered, although these have a sense that is orthogonal to the
353 anisotropic pattern obtained by the main AAN tomographic results, confirming the reliability of
354 the FVDs obtained by the main AAN tomography.

355 **6. Discussion**

356 According to the resolution tests in Section 5, we here discuss the structure at depths of
357 190–550 km. The RAN and AAN tomographic results in this depth range do not change largely
358 at any depth, whose characteristics are represented by the map views at a depth of 310 km that
359 are enlarged in Figures 12a and 12b. Figure 12c summarizes the characteristics of isotropic
360 component, RAN, and AAN for seven areas (NEG body, Iceland hotspot, Jan Mayen hotspot,
361 Svalbard hotspot, Labrador Sea, Davis Strait, and Baffin Bay). First, the characteristics of AAN
362 (Figure 12b) beneath Greenland are compared with the SWS measurements (Figure 12d) by
363 Ucisik et al. (2008). The SWS feature is estimated to be mainly in the upper mantle, but some
364 contributions from the crust and lower mantle maybe present (Ucisik et al., 2008). The overall
365 characteristics of the two results are similar: for example, FVD along coastline is dominant
366 beneath the northeastern coast of Greenland, no apparent anisotropy can be observed beneath the
367 SUMG station in central Greenland, and FVD in the NE-SW direction is dominant beneath the
368 west coast of Greenland. Different from the SWS measurements that have poor depth resolution,
369 the anisotropic tomography reveals 3-D isotropic and anisotropic structures, which brings more

370 detailed insights into the static and dynamic features. In the following, we discuss main features
371 in each of the seven areas in [Figures 12a–12c](#).

372 **6.1 The Northeast Greenland body.**

373 The NEG body is characterized by a high- V_{P0} anomaly, a strong negative RAN ($V_{Ph} <$
374 V_{Pv}), and a strong AAN with N-S to NE-SW FVDs. This body is presumed as a remnant of the
375 oceanic lithosphere that made up the Iapetus Ocean closed at 490–390 Ma. The causes of seismic
376 anisotropy in such a cold rock body may be (1) fossil anisotropy originally possessed by the
377 oceanic lithosphere, (2) shape-preferred orientation (SPO) associated with the shape and texture
378 of the rock body, and (3) LPO accompanying with mantle flow. Since both the isotropic and
379 anisotropic characteristics inside the NEG body are clearly different from those in the
380 surrounding regions, we consider that (1) and (2) are primarily responsible. In particular,
381 regarding (2), since the NEG body includes the inland Caledonian fold belt, which has a fold axis
382 in the N-S direction, we expect that the FVDs are likely to be dominant along the fold axis
383 ([Okaya et al., 2018](#)), and that the weight of the rock body causes consolidation resulting in
384 $V_{Ph} < V_{Pv}$. Such an interpretation well explains the results of this study.

385 **6.2 Iceland, Jan Mayen, and Svalbard hotspots**

386 The upper mantle beneath the Iceland hotspot is characterized by a strong positive RAN
387 ($V_{Ph} > V_{Pv}$) and a weak AAN with NW-SE FVDs, which may primarily be associated with the
388 Iceland plume. The Iceland plume is one of the strongest buoyant plumes in the world, and so is
389 estimated that the rising rate of mantle material in the center of the plume is extremely fast.
390 Possible causes of anisotropy in such plumes are (1) LPO associated with the flow of the plume
391 and the surrounding mantle, and (2) SPO due to the shape of the plume and the heterogeneous

392 distribution of mantle materials with different temperatures. Regarding (1), the vertical LPO is
393 dominant in the plume center, whereas in the surrounding regions, the mantle flow is drawn
394 toward or diverges from the plume center, creating a radial flow field that dominates horizontal
395 LPO (Marquart et al., 2007). Regarding (2), low- V material continues in the vertical direction
396 along the rising plume, whereas in the horizontal direction, the material properties change from
397 low- V at the plume center to high- V in the surrounding regions, resulting in horizontal FVDs that
398 are distributed radially from the plume center. Therefore, in both cases, the feature of $V_{Ph} > V_{Pv}$
399 appears macroscopically, and a weak or negligible AAN is expected by canceling out the radial
400 FVDs. Such an interpretation well explains the results of this study. Because there is no
401 resolution for the narrow central conduit of the rising plume in the tomographic inversions in the
402 current spatial scale, the feature of $V_{Ph} > V_{Pv}$ is expected to be dominant in RAN, reflecting the
403 properties in the surrounding wide areas. On the other hand, SWS measurements in Iceland
404 revealed N-S to NW-SE FPOs, which are interpreted to reflect the background mantle flow
405 (Figure 12e, Bjarnason et al., 2002). The SWS results are considered to reflect anisotropy at
406 depths shallower than 200 km (Bjarnason et al., 2002), but background mantle flow in the same
407 direction is also reported to exist at 600-km depth (Ito et al., 2014). The weak FVDs found in this
408 study are also in the same direction, supporting the existence of the background mantle flow
409 beneath Iceland.

410 Previous studies also suggested the presence of mantle plumes beneath the Jan Mayen
411 (e.g., Elkins et al., 2016; Schilling et al., 1999) and Svalbard hotspots (Toyokuni et al., 2020a).
412 In this study, a strong positive RAN ($V_{Ph} > V_{Pv}$) and a negligible AAN are found beneath these
413 hotspots, and so the existence of mantle plumes is more conclusive according to the same
414 interpretation as in the case of Iceland plume. In addition, unlike the case of Iceland plume, there

415 is no weak AAN reflecting the background mantle flow beneath the Jan Mayen hotspot. The
416 AAN-SRT1 and AAN-SRT2 results show that if AAN is originally present beneath Jan Mayen,
417 it can be sufficiently detected (Figures 12d and 12e). Therefore, this result may suggest that the
418 Iceland plume and the Jan Mayen plume may belong to different plume systems. The difference
419 between the Iceland and Jan Mayen plumes was also pointed out by geochemical studies due to
420 their difference in magma composition (e.g., Schilling et al., 1999). Toyokuni et al. (2020b) also
421 suggested that the Jan Mayen and Svalbard plumes are tributaries of the Greenland plume rising
422 from the CMB beneath Greenland, and so the plume system is distinguishable from the rather
423 isolated Iceland plume. The results of this study reinforce such previous interpretations.

424 In the cross-sections of the RAN and AAN tomography passing through Greenland and
425 Iceland, or Greenland and Jan Mayen, CGLLVZ is clearly visible in the isotropic V_p image
426 inside the lithosphere beneath Greenland, whose thickness is estimated to be >200 km V_p
427 (Artemieva, 2019; Jakovlev et al., 2012). The origin of CGLLVZ is thought to be residual heat of
428 the Iceland and Jan Mayen plumes (Toyokuni et al., 2020a). The RAN cross-sections show that
429 the RAN strength, which is very strong beneath Iceland, suddenly weakens when entering
430 CGLLVZ. This may be due to that CGLLVZ is currently out of the mantle plumes, reinforcing
431 the interpretation of Toyokuni et al. (2020a).

432 **6.3 Labrador Sea, Davis Strait, and Baffin Bay**

433 Breakup between Greenland and Canada is estimated to have occurred during the Late
434 Cretaceous to early Cenozoic (Henriksen et al., 2009), but the cause of the breakup is currently
435 under debate. So far, two contradicting hypotheses have been proposed: active breakup caused
436 by the rising Iceland plume beneath Davis Strait, and passive breakup caused by far-field plate
437 forces. Peace et al. (2017) denied the mantle plume hypothesis by combining various

438 observations, and proposed that the breakup began in the Labrador Sea in the south by far-field
439 plate forces, but it was blocked by a thick continental keel beneath Davis Strait and did not
440 propagate to Baffin Bay in the north.

441 Our results show that the Labrador Sea is characterized by a strong positive RAN
442 ($V_{Ph} > V_{Pv}$) and a negligible AAN, which is similar to the features of the mantle plume
443 described in [Section 6.2](#). In addition, the isotropic tomography shows a conduit-like low- V_p
444 anomaly at depths ≤ 300 km ([Figure S7](#)), suggesting the existence of local mantle upwelling. On
445 the other hand, beneath Baffin Bay, there is no characteristic aspect because the isotropic
446 component is average, and both RAN and AAN are negligible. The AAN-SRT1 and AAN-SRT2
447 results show that if AAN is originally present beneath Baffin Bay and the Labrador Sea, it can be
448 sufficiently detected ([Figures 11d and 11e](#)). Davis Strait, located between these two areas,
449 exhibits a clear high- V_p corridor extending from land at depths of 160–430 km ([Figure S7](#)),
450 suggesting the presence of cold and rigid rock bodies as mentioned by [Peace et al. \(2017\)](#). The
451 AAN is remarkably strong only in this area, showing NE-SW to E-W FVDs that are continuous
452 from the west coast of Greenland and Baffin Island, also supporting the existence of rock bodies.
453 Such FVDs are considered to reflect fossil anisotropy of rock body and/or LPO by mantle flow.
454 A positive RAN ($V_{Ph} > V_{Pv}$) continuing from the Labrador Sea is dominant in the south, but it
455 becomes negligible in the north. Combining the above features, we suggest the following process
456 of the breakup between Greenland and Canada: the opening of the Labrador Sea was initiated by
457 a local mantle upwelling, but the rock body beneath Davis Strait prevented the northward
458 propagation of the breakup, while the Baffin Bay opened by a passive rift due to far-field plate
459 forces. This is in good agreement with the interpretation of [Peace et al. \(2017\)](#), but we suggest

460 the existence of a local mantle upwelling beneath the Labrador Sea, which could be the driving
461 force of the breakup.

462 Traditionally, the Tertiary basalt province on the west coast of Greenland was thought to
463 have been formed by the Iceland plume track. However, several recent studies do not support
464 this interpretation (Martos et al., 2018; Toyokuni et al., 2020a). Locally enhanced magmatism
465 due to the northward-propagating Labrador Sea rift is blocked beneath Davis Strait may be a
466 rational explanation for the Tertiary basalt province and existence of hot springs on the west
467 coast of Greenland. In addition, Toyokuni et al. (2020a) suggested that the high geothermal heat
468 flux (Martos et al., 2018) and low- V_p in the Archean block in southern Greenland were caused by
469 a selective heat transfer from a hot mantle material beneath the Labrador Sea. The existence of
470 local mantle upwelling suggested by this study reinforces this possibility. Regarding the origin of
471 this local mantle upwelling, further tomographic studies targeting much wider regions are
472 required.

473 Figure 13 shows a comparison of our AAN tomographic images with simulation results
474 of the mantle flow field due to the rising Iceland plume (Marquart et al., 2007). The FVDs
475 beneath Greenland are in good agreement with the directions of mantle flow, except at a depth of
476 680 km, where our tomographic resolution is relatively lower. Because the strong AAN areas
477 correspond to the NEG body and another rock body beneath Davis Strait, the resulting
478 anisotropy may be strongly influenced by the fossil anisotropy and SPO in these bodies.
479 However, the good agreement of our results with the mantle flow model suggests that the LPO
480 due to the rising Iceland, Jan Mayen, and Svalbard plumes is detected by our anisotropic
481 tomography.

482 7. Conclusions

483 The first 3-D P -wave RAN and AAN model beneath Greenland and its surrounding
 484 regions down to 750-km depth is obtained by inverting a large number of high-quality P -wave
 485 arrival-times of local earthquakes and relative travel-time residuals of teleseismic events
 486 recorded by the GLISN and other seismic stations. Our novel tomographic results reveal the
 487 following features.

488 (1) The NEG body distributed from Northeast Greenland to its offshore at depths $\leq \sim 500$
 489 km exhibits a strong negative RAN ($V_{Ph} < V_{Pv}$) and a strong AAN with N-S to NE-SW FVDs.
 490 Because the NEG body is considered as a remnant of oceanic lithosphere of the Iapetus Ocean
 491 closed at 490–390 Ma when Laurentia and Baltica collided, the RAN and AAN might reflect
 492 fossil anisotropy inside the oceanic lithosphere, SPO associated with the fold, and/or LPO
 493 associated with mantle flow due to the upper-mantle plume system such as the Iceland plume.

494 (2) Low- V_p zones beneath the Iceland, Jan Mayen, and Svalbard hotspots are
 495 characterized by a strong positive RAN ($V_{Ph} > V_{Pv}$) and negligible or weak AAN, which may
 496 reflect horizontal radial LPO and/or SPO centered at the rising mantle plumes. The existence of
 497 Svalbard plume was first suggested by [Toyokuni et al. \(2020a\)](#), but this study confirms it more
 498 concretely from the perspective of seismic anisotropy. Furthermore, a weak AAN is revealed
 499 only beneath Iceland, which is thought to reflect the background mantle flow. This locality might
 500 suggest differences of the Iceland plume system in the south and the Jan Mayen–Svalbard plume
 501 system in the north, as pointed out in [Toyokuni et al. \(2020b\)](#).

502 (3) The upper mantle beneath the Labrador Sea is characterized by isotropic low- V_p and a
 503 strong positive RAN ($V_{Ph} > V_{Pv}$) and a negligible AAN, suggesting the presence of local mantle
 504 upwelling. On the other hand, the upper mantle beneath Baffin Bay has an average isotropic

505 feature and no noticeable anisotropy. Davis Strait, located between these two regions, is
506 characterized by isotropic high- V_p , a transitive RAN, and a strong AAN, suggesting the presence
507 of cold rock bodies. These results suggest that breakup between Greenland and Canada might be
508 caused as follows: the breakup started at the Labrador Sea because of local mantle upwelling, the
509 northward propagation of the breakup was blocked at Davis Strait, and Baffin Bay was opened
510 by far-field plate forces.

511 **Acknowledgments**

512 We are grateful to Drs. Dean Childs, Kevin Nikolaus, Kent Anderson, Masaki Kanao,
513 Yoko Tono, Seiji Tsuboi, Robin Abbott, Kathy Young, Drew Abbott, Silver Williams, Jason
514 Hebert, Tetsuto Himeno, Susan Whitley, Orlando Leone, Akram Mostafanejad, Kirsten Arnell,
515 and other staff members at GLISN, IRIS/PASSCAL, CH2M HILL Polar Services, and
516 Norlandair for their contributions to the field operations in Greenland. We thank the staff of the
517 ISC, IRIS/DMC, and USGS for providing the open-access arrival-time and waveform data used
518 in this study. Dr. Árni Hjartarson kindly provided the hot springs locations in Greenland. We
519 appreciate Drs. Hiroshi Takenaka, Akira Hasegawa, Toru Matsuzawa, Ryota Takagi, Keisuke
520 Yoshida, and Katsutada Kaminuma for helpful discussions. This work was partially supported by
521 research grants from Japan Society for the Promotion of Science (Nos. 18K03794, 24403006,
522 23224012, and 26241010). The GMT ([Wessel et al., 2013](#)) and SAC ([Goldstein et al., 2003](#))
523 software packages are used in this study. Part of the arrival-time data are downloaded from the
524 ISC (<http://www.isc.ac.uk/>). The waveform data are downloaded from the IRIS/DMC
525 (<https://ds.iris.edu/ds/nodes/dmc/>). Part of the event data are also downloaded from the USGS
526 (<https://www.usgs.gov/>). Archiving of data from this study is underway through Zenodo.
527 Currently these data can be seen in Supporting Information for review purposes.

528 **Author contributions**

529 Conceptualization: Genti Toyokuni, Dapeng Zhao

530 Data curation: Genti Toyokuni

531 Formal analysis: Genti Toyokuni

532 Methodology: Genti Toyokuni, Dapeng Zhao

533 Resources: Genti Toyokuni, Dapeng Zhao

534 Visualization: Genti Toyokuni

535 Writing – original draft: Genti Toyokuni

536 Writing – review & editing: Genti Toyokuni, Dapeng Zhao

537 **References**

538 Artemieva, I. M. (2019). Lithosphere thermal thickness and geothermal heat flux in Greenland
539 from a new thermal isostasy method. *Earth-Science Reviews*, 188, 469–481.

540 <https://doi.org/10.1016/j.earscirev.2018.10.015>

541 Bjarnason, I. T., Silver, P. G., Rumpker, G., & Solomon, S. C. (2002). Shear wave splitting
542 across the Iceland hot spot: Results from the ICEMELT experiment. *Journal of*
543 *Geophysical Research*, 107(B12), 2382. <https://doi.org/10.1029/2001JB000916>

544 Clinton, J. F., Nettles, M., Walter, F., Anderson, K., Dahl-Jensen, T., Giardini, D., Govoni, A.,
545 Hanka, W., Lasocki, S., Lee, W. S., McCormack, D., Mykkeltveit, S., Stutzmann, E., &
546 Tsuboi, S. (2014). Seismic network in Greenland monitors Earth and ice system. *Eos,*
547 *Transactions, American Geophysical Union*, 95(2), 13–24.

548 <https://doi.org/10.1002/2014EO020001>

- 549 Darbyshire, F. A., Dahl-Jensen, T., Larsen, T. B., Voss, P. H., & Joyal, G. (2018). Crust and
550 uppermost-mantle structure of Greenland and the Northwest Atlantic from Rayleigh wave
551 group velocity tomography. *Geophysical Journal International*, 212(3), 1546–1569.
552 <https://doi.org/10.1093/gji/ggx479>
- 553 Dumke, I., Burwicz, E. B., Berndt, C., Klaeschen, D., Feseker, T., Geissler, W. H., & Sarkar, S.
554 (2016). Gas hydrate distribution and hydrocarbon maturation north of the Knipovich
555 Ridge, western Svalbard margin. *Journal of Geophysical Research: Solid Earth*, 121(3),
556 1405–1424. <https://doi.org/10.1002/2015JB012083>
- 557 Elkins, L. J., Hamelin, C., Blichert-Toft, J., Scott, S. R., Sims, K. W. W., Yeo, I. A., Devey, C.
558 W., & Pedersen, R. B. (2016). North Atlantic hotspot-ridge interaction near Jan Mayen
559 Island. *Geochemical Perspectives Letters*, 2(1), 55–67.
560 <http://dx.doi.org/10.7185/geochemlet.1606>
- 561 Goldstein, P., Dodge, D., Firpo, M., & Minner, L. (2003). SAC2000: Signal processing and
562 analysis tools for seismologists and engineers. In W. H. K. Lee, H. Kanamori, P. C.
563 Jennings, & C. Kisslinger (Eds.), *International Geophysics* (Vol. 81, pp. 1613–1614).
564 London: Academic Press.
- 565 Gou, T., Zhao, D., Huang, Z., & Wang, L. (2019). Aseismic deep slab and mantle flow beneath
566 Alaska: Insight from anisotropic tomography. *Journal of Geophysical Research: Solid
567 Earth*, 124, 1700–1724. <https://doi.org/10.1029/2018JB016639>
- 568 Henriksen, N., Higgins, A. K., Kalsbeek, F., & Pulvertaft, T. C. R. (2009). *Greenland from
569 Archean to Quaternary, Descriptive Text to the 1995 Geological Map of Greenland*,

- 570 1:2 500 000, 126 pp. Copenhagen: Geological Survey of Denmark and Greenland.
571 <https://doi.org/10.1007/978-4-431-55360-1>
- 572 Hjartarson, A., & Armannsson, H. (2010). *Geothermal research in Greenland*. Paper presented
573 at World Geothermal Congress 2010, Bali, Indonesia.
- 574 Huang, Z., Zhao, D., & Wang, L. (2015). P wave tomography and anisotropy beneath Southeast
575 Asia: Insight into mantle dynamics. *Journal of Geophysical Research: Solid Earth*, 120,
576 5154–5174. <https://doi.org/10.1002/2015JB012098>
- 577 Ishise, M., & Oda, H. (2005). Three-dimensional structure of P-wave anisotropy beneath Tohoku
578 district, northeast Japan. *Journal of Geophysical Research*, 110, B07304.
579 <https://doi.org/10.1029/2004JB003599>
- 580 Ito, G., Dunn, R., Li, A., Wolfe, C. J., Gallego, A., & Fu, Y. (2014). Seismic anisotropy and
581 shear wave splitting associated with mantle plume-plate interaction. *Journal of*
582 *Geophysical Research: Solid Earth*, 119, 4923–4937.
583 <https://doi.org/10.1002/2013JB010735>
- 584 Jakovlev, A. V., Bushenkova, N. A., Koulakov, I. Yu., & Dobretsov, N. L. (2012). Structure of
585 the upper mantle in the Circum-Arctic region from regional seismic tomography. *Russian*
586 *Geology and Geophysics*, 53(10), 963–971. <https://doi.org/10.1016/j.rgg.2012.08.001>
- 587 Jiang, G., Zhao, D., & Zhang, G. (2009a). Seismic tomography of the Pacific slab edge under
588 Kamchatka. *Tectonophysics*, 465(1–4), 190–203.
589 <https://doi.org/10.1016/j.tecto.2008.11.019>

- 590 Jiang, G., Zhao, D., & Zhang, G. (2009b). Crustal correction in teleseismic tomography and its
591 application (in Chinese with English abstract). *Chinese Journal of Geophysics*, 52(6),
592 1508–1514. <https://doi.org/10.3969/j.issn.0001-5733.2009.06.012>
- 593 Jiang, G., Zhang, G., Zhao, D., Lü, Q., Li, H., & Li, X. (2015). Mantle dynamics and Cretaceous
594 magmatism in east-central China: Insight from teleseismic tomograms. *Tectonophysics*,
595 664, 256–268. <https://doi.org/10.1016/j.tecto.2015.09.019>
- 596 Karato, S., Jung, H., Katayama, I., & Skemer, P. (2008). Geodynamic significance of seismic
597 anisotropy of the upper mantle: New insights from laboratory studies. *Annual Review of*
598 *Earth and Planetary Sciences*, 36(1), 59–95.
599 <https://doi.org/10.1146/annurev.earth.36.031207.124120>
- 600 Katayama, I., & Karato, S. (2006). Effect of temperature on the B- to C-type olivine fabric
601 transition and implication for flow pattern in subduction zones. *Physics of the Earth and*
602 *Planetary Interiors*, 157(1–2), 33–45. <https://doi.org/10.1016/j.pepi.2006.03.005>
- 603 Kumar, P., Kind, R., Priestley, K., & Dahl-Jensen, T. (2007). Crustal structure of Iceland and
604 Greenland from receiver function studies. *Journal of Geophysical Research: Solid Earth*,
605 112(B3), B03301. <https://doi.org/10.1029/2005JB003991>
- 606 Lebedev, S., Schaeffer, A. J., Fullea, J., & Pease, V. (2017). Seismic tomography of the Arctic
607 region: inferences for the thermal structure and evolution of the lithosphere. *Geological*
608 *Society, London, Special Publications*, 460, 419–440. <https://doi.org/10.1144/SP460.10>
- 609 Levshin, A. L., Shen, W., Barmin, M. P., & Ritzwoller, M. H. (2017). Surface wave studies of
610 the Greenland upper lithosphere using ambient seismic noise.
611 <https://pdfs.semanticscholar.org/977c/ce2101b7f9b384d38e9b051bf289a7277b54.pdf>

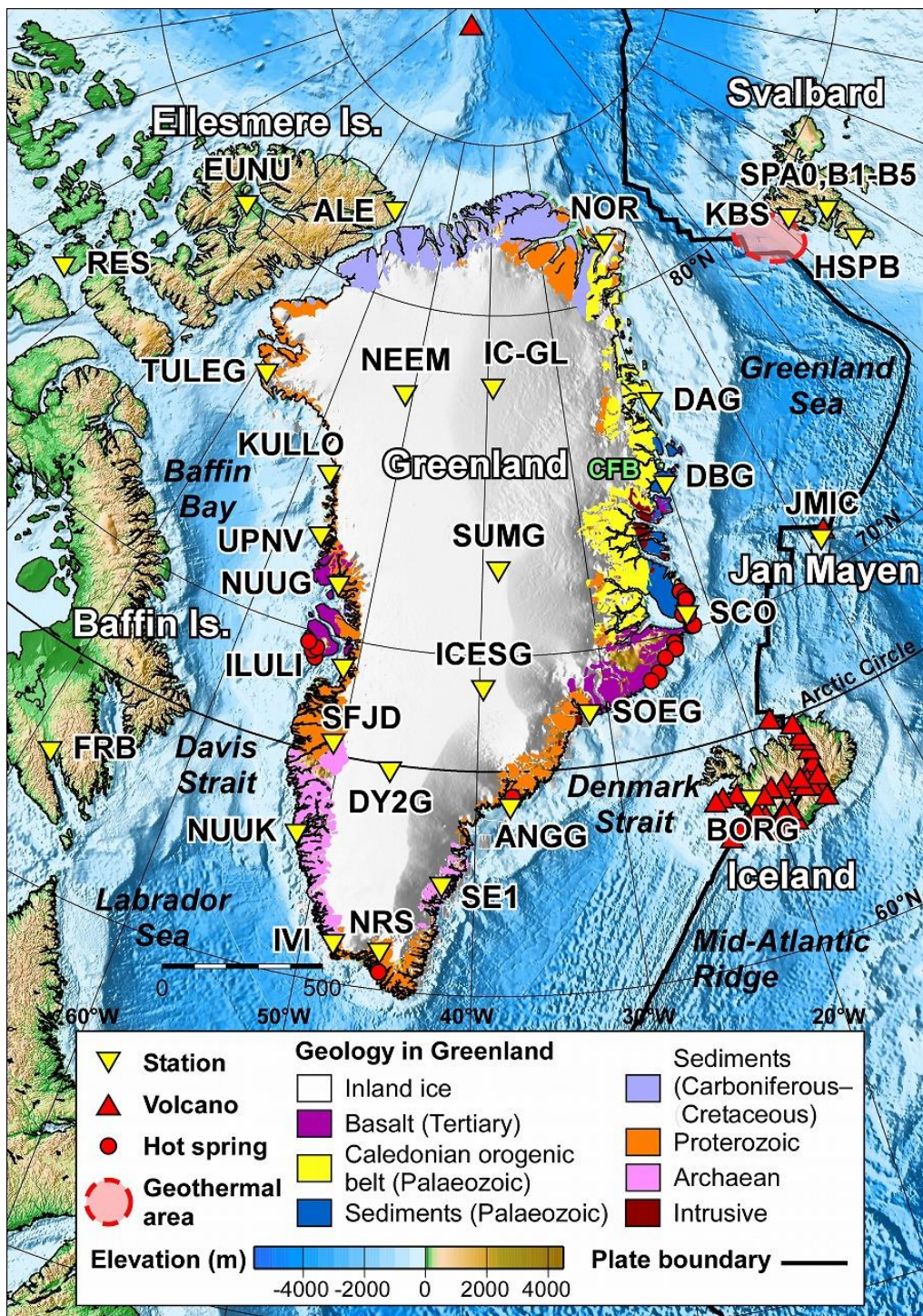
- 612 Liu, X., & Zhao, D. (2017). P-wave anisotropy, mantle wedge flow and olivine fabrics beneath
613 Japan. *Geophysical Journal International*, 210, 1410-1431.
614 <https://doi.org/10.1093/gji/ggx247>
- 615 Long, M. D., & Becker, T. W. (2010). Mantle dynamics and seismic anisotropy. *Earth and*
616 *Planetary Science Letters*, 297(3–4), 341–354. <https://doi.org/10.1016/j.epsl.2010.06.036>
- 617 Marquart, G., Schmeling, H., & Čadež, O. (2007). Dynamic models for mantle flow and seismic
618 anisotropy in the North Atlantic region and comparison with observations. *Geochemistry,*
619 *Geophysics, Geosystems*, 8, Q02008. <https://doi.org/10.1029/2006GC001359>
- 620 Martos, Y. M., Jordan, T. A., Catalán, M., Jordan, T. M., Bamber, J. L., & Vaughan, D. G.
621 (2018). Geothermal heat flux reveals the Iceland hotspot track underneath Greenland.
622 *Geophysical Research Letters*, 45, 8214–8222. <https://doi.org/10.1029/2018GL078289>
- 623 Metelkin, D. V., Vernikovskiy, V. A., & Matushkin, N. Yu. (2015). Arctida between Rodinia and
624 Pangea. *Precambrian Research*, 259, 114–129.
625 <https://doi.org/10.1016/j.precamres.2014.09.013>
- 626 Mordret, A. (2018). Uncovering the Iceland hot spot track beneath Greenland. *Journal of*
627 *Geophysical Research: Solid Earth*, 123, 4922–4941.
628 <https://doi.org/10.1029/2017JB015104>
- 629 Mordret, A., Mikesell, T. D., Harig, C., Lipovsky, B. P., & Prieto, G. A. (2016). Monitoring
630 southwest Greenland's ice sheet melt with ambient seismic noise. *Science Advances*,
631 2(5), e1501538. <http://dx.doi.org/10.1126/sciadv.1501538>

- 632 Okaya, D., Vel, S. S., Song, W. J., & Johnson, S. E. (2018). Modification of crustal seismic
633 anisotropy by geological structures ("structural geometric anisotropy"). *Geosphere*, 15(1),
634 146–170. <https://doi.org/10.1130/GES01655.1>
- 635 Paige, C. C., & Saunders, M. A. (1982). LSQR, An algorithm for sparse linear equations and
636 sparse least squares. *ACM Transactions on Mathematical Software (TOMS)*, 8(1), 43–71.
637 <https://doi.org/10.1145/355984.355989>
- 638 Peace, A. L., Foulger, G. R., Schiffer, C., & McCaffrey, K. J. (2017). Evolution of Labrador
639 Sea–Baffin Bay: Plate or plume processes? *Geoscience Canada*, 44(3), 91–102.
640 <https://doi.org/10.12789/geocanj.2017.44.120>
- 641 Portnov, A., Vadakkepuliambatta, S., Mienert, J., & Hubbard, A. (2016). Ice-sheet-driven
642 methane storage and release in the Arctic. *Nature Communications*, 7, 10314.
643 <https://doi.org/10.1038/ncomms10314>
- 644 Pourpoint, M., Anandakrishnan, S., Ammon, C. J., & Alley, R. B. (2018). Lithospheric structure
645 of Greenland from ambient noise and earthquake surface wave tomography. *Journal of*
646 *Geophysical Research: Solid Earth*, 123, 7850–7876.
647 <https://doi.org/10.1029/2018JB015490>
- 648 Rickers, F., Fichtner, A., & Trampert, J. (2013). The Iceland–Jan Mayen plume system and its
649 impact on mantle dynamics in the North Atlantic region: Evidence from full-waveform
650 inversion. *Earth and Planetary Science Letters*, 367, 39–51.
651 <https://doi.org/10.1016/j.epsl.2013.02.022>
- 652 Schilling, J.-G., Kingsley, R., Fontignie, D., Poreda, R., & Xue, S. (1999). Dispersion of the Jan
653 Mayen and Iceland mantle plumes in the Arctic: A He-Pb-Nd-Sr isotope tracer study of

- 654 basalts from the Kolbeinsey, Mohns, and Knipovich Ridges. *Journal of Geophysical*
655 *Research*, 104(B5), 10543–10569. <https://doi.org/10.1029/1999JB900057>
- 656 Takenaka, H., Komatsu, M., Toyokuni, G., Nakamura, T., & Okamoto, T. (2017). Quasi-
657 Cartesian finite-difference computation of seismic wave propagation for a three-
658 dimensional sub-global model. *Earth, Planets and Space*, 69, 67.
659 <https://doi.org/10.1186/s40623-017-0651-1>
- 660 Thiede, J., Eldholm, O., & Myhre, A. M. (2011). Chapter 46 Scientific deep-sea drilling in high
661 northern latitudes. *Geological Society, London, Memoirs*, 35, 703–714.
662 <https://doi.org/10.1144/M35.46>
- 663 Toyokuni, G., Kanao, M., Tono, Y., Himeno, T., Tsuboi, S., Childs, D., Anderson, K., &
664 Takenaka, H. (2014). Monitoring of the Greenland ice sheet using a broadband
665 seismometer network: the GLISN project. *Antarctic Record*, 58(1), 1–18.
666 <http://doi.org/10.15094/00009722>
- 667 Toyokuni, G., Komatsu, M., & Takenaka, H. (2021). Estimation of seismic attenuation of the
668 Greenland Ice Sheet using 3-D waveform modeling. *Journal of Geophysical Research:*
669 *Solid Earth*. <https://doi.org/10.1029/2021JB021694>
- 670 Toyokuni, G., Matsuno, T., & Zhao, D. (2020a). *P* wave tomography beneath Greenland and
671 surrounding regions: 1. Crust and upper mantle. *Journal of Geophysical Research: Solid*
672 *Earth*, 125, e2020JB019837. <https://doi.org/10.1029/2020JB019837>
- 673 Toyokuni, G., Matsuno, T., & Zhao, D. (2020b). *P* wave tomography beneath Greenland and
674 surrounding regions: 2. Lower mantle. *Journal of Geophysical Research: Solid Earth*,
675 125, e2020JB019839. <https://doi.org/10.1029/2020JB0198379>

- 676 Toyokuni, G., Takenaka, H., Kanao, M., Tsuboi, S., & Tono, Y. (2015). Numerical modeling of
677 seismic waves for estimating the influence of the Greenland ice sheet on observed
678 seismograms. *Polar Science*, 9(1), 80–93. <https://doi.org/10.1016/j.polar.2014.12.001>
- 679 Toyokuni, G., Takenaka, H., Takagi, R., Kanao, M., Tsuboi, S., Tono, Y., Childs, D., & Zhao, D.
680 (2018). Changes in Greenland ice bed conditions inferred from seismology. *Physics of*
681 *the Earth and Planetary Interiors*, 277, 81–98. <https://doi.org/10.1016/j.pepi.2017.10.010>
- 682 Ucisik, N., Gudmundsson, Ó., Priestley, K., & Larsen, T. B. (2005). Seismic anisotropy beneath
683 east Greenland revealed by shear wave splitting. *Geophysical Research Letters*, 32,
684 L08315. <https://doi.org/10.1029/2004GL021875>
- 685 Ucisik, N., Gudmundsson, Ó., Hanka, W., Dahl-Jensen, T., Mosegaard, K., & Priestley, K.
686 (2008). Variations of shear-wave splitting in Greenland: Mantle anisotropy and possible
687 impact of the Iceland plume. *Tectonophysics*, 462(1–4), 137–148.
688 <https://doi.org/10.1016/j.tecto.2007.11.074>
- 689 Um, J., & Thurber, C. (1987). A fast algorithm for two-point seismic ray tracing. *Bulletin of the*
690 *Seismological Society of America*, 77(3), 972–986.
- 691 Wang, J., & Zhao, D. (2008). P-wave anisotropic tomography beneath Northeast Japan. *Physics*
692 *of the Earth and Planetary Interiors*, 170(1–2), 115–133.
693 <https://doi.org/10.1016/j.pepi.2008.07.042>
- 694 Wang, J., & Zhao, D. (2013). P-wave tomography for 3-D radial and azimuthal anisotropy of
695 Tohoku and Kyushu subduction zones. *Geophysical Journal International*, 193(3), 1166–
696 1181. <https://doi.org/10.1093/gji/ggt086>
- 697 Wang, Z. W., & Zhao, D. (2021). 3D anisotropic structure of the Japan subduction zone. *Science*
698 *Advances*, 7, eabc9620. <https://doi.org/10.1126/sciadv.abc9620>

- 699 Wessel, P., Smith, W. H. F., Scharroo, R., Luis, J., & Wobbe, F. (2013). Generic Mapping Tools:
700 Improved Version Released. *Eos, Transactions, American Geophysical Union*, 94(45),
701 409. <https://doi.org/10.1002/2013EO450001>
- 702 Zhang, H., Zhao, D., Ju, C., Li, Y. E. Li, G., Ding, M., Chen, S., & Zhao, J. (2020). Upper
703 mantle deformation of the Terror Rift and northern Transantarctic Mountains in
704 Antarctica: Insight from *P* wave anisotropic tomography. *Geophysical Research Letters*,
705 47, e2019GL086511. <https://doi.org/10.1029/2019GL086511>
- 706 Zhao, D. (2015). *Multiscale Seismic Tomography*, 304 pp. Tokyo: Springer.
707 <https://doi.org/10.1007/978-4-431-55360-1>
- 708 Zhao, D., Hasegawa, A., & Horiuchi, S. (1992). Tomographic imaging of P and S wave velocity
709 structure beneath northeastern Japan. *Journal of Geophysical Research*, 97(B13), 19909–
710 19928. <https://doi.org/10.1029/92JB00603>
- 711 Zhao, D., Hasegawa, A., & Kanamori, H. (1994). Deep structure of Japan subduction zone as
712 derived from local, regional, and teleseismic events. *Journal of Geophysical Research:*
713 *Solid Earth*, 99(B11), 22313–22329. <https://doi.org/10.1029/94JB01149>
- 714 Zhao, D., Yanada, T., Hasegawa, A., Umino, N., & Wei, W. (2012). Imaging the subducting
715 slabs and mantle upwelling under the Japan Islands. *Geophysical Journal International*,
716 190(2), 816–828. <https://doi.org/10.1111/j.1365-246X.2012.05550.x>
- 717
- 718
- 719
- 720



721
 722 **Figure 1.** Map of Greenland and its surrounding regions. White color denotes the Greenland ice
 723 sheet (GrIS). Yellow triangles: seismic stations used in this study; red triangles: active

724 volcanoes; red dots: hot springs. The red dashed line shows the Svalbard geothermal area
725 ([Dumke et al., 2016](#); [Portnov et al., 2016](#)). Geological map of Greenland ([Kumar et al., 2007](#)) is
726 also shown. CFB = Caledonian fold belt.

727

728

729

730

731

732

733

734

735

736

737

738

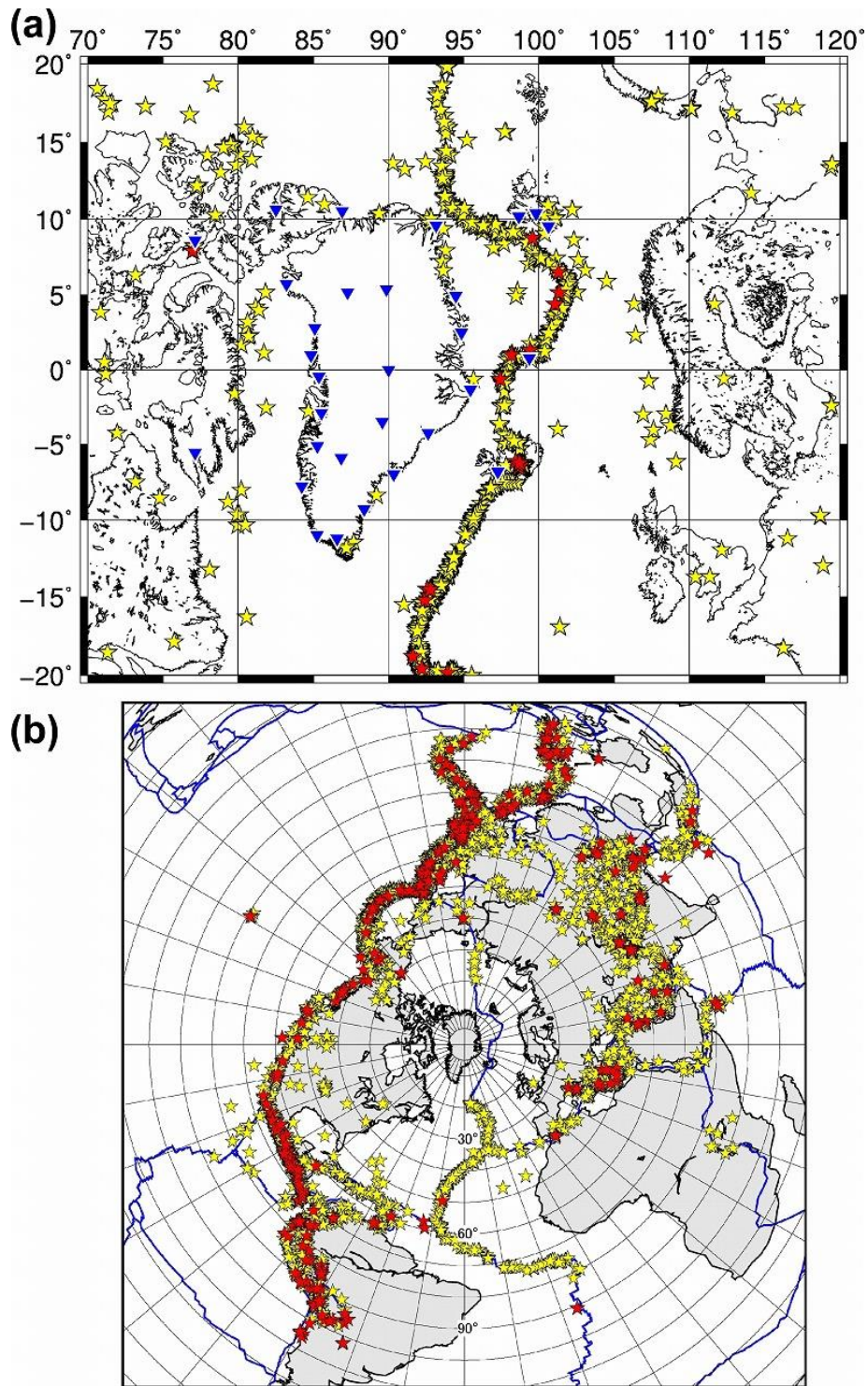
739

740

741

742

743



744

745 **Figure 2.** Epicentral distribution of (a) local earthquakes and (b) teleseismic events used in this

746 study. The panel (a) also displays longitudinal and latitudinal ranges of our study region. In (a),

747 yellow stars: 1,288 events from the ISC-EHB catalog; red stars: 21 events whose arrival times
748 were manually picked by the authors. In (b), red circles: 6,884 events from the ISC-EHB catalog;
749 red stars: 347 events whose arrival times were picked by [Toyokuni et al. \(2020a\)](#) using a
750 waveform cross-correlation method.

751

752

753

754

755

756

757

758

759

760

761

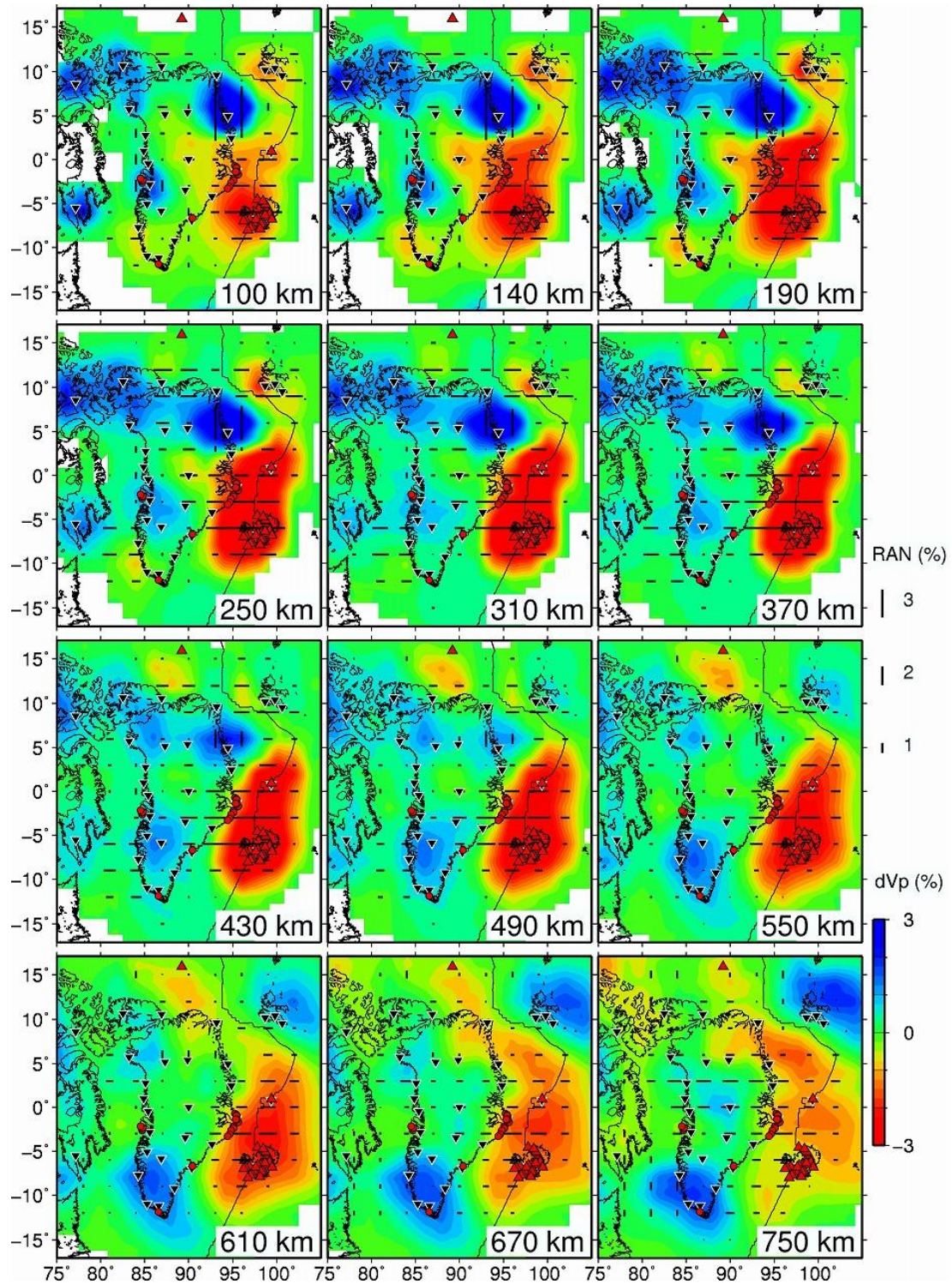
762

763

764

765

766



767

768 **Figure 3.** Map view images of V_p radial anisotropy (RAN) tomography. The layer depth is
 769 shown at the lower-right corner of each panel. Blue and red colors denote high and low isotropic

770 V_P perturbations, respectively, whose scale (in %) is shown on the right. The length of black bars
771 denotes the RAN amplitude, whose scale (in %) is also shown on the right. The horizontal and
772 vertical bars denote positive RAN ($V_{Ph} > V_{Pv}$) and negative RAN ($V_{Ph} < V_{Pv}$), respectively.
773 Areas with hit counts < 5 are masked in white. The red triangles, red dots, black triangles, and
774 thin black lines denote active volcanoes, hot springs, seismic stations, and plate boundaries,
775 respectively.

776

777

778

779

780

781

782

783

784

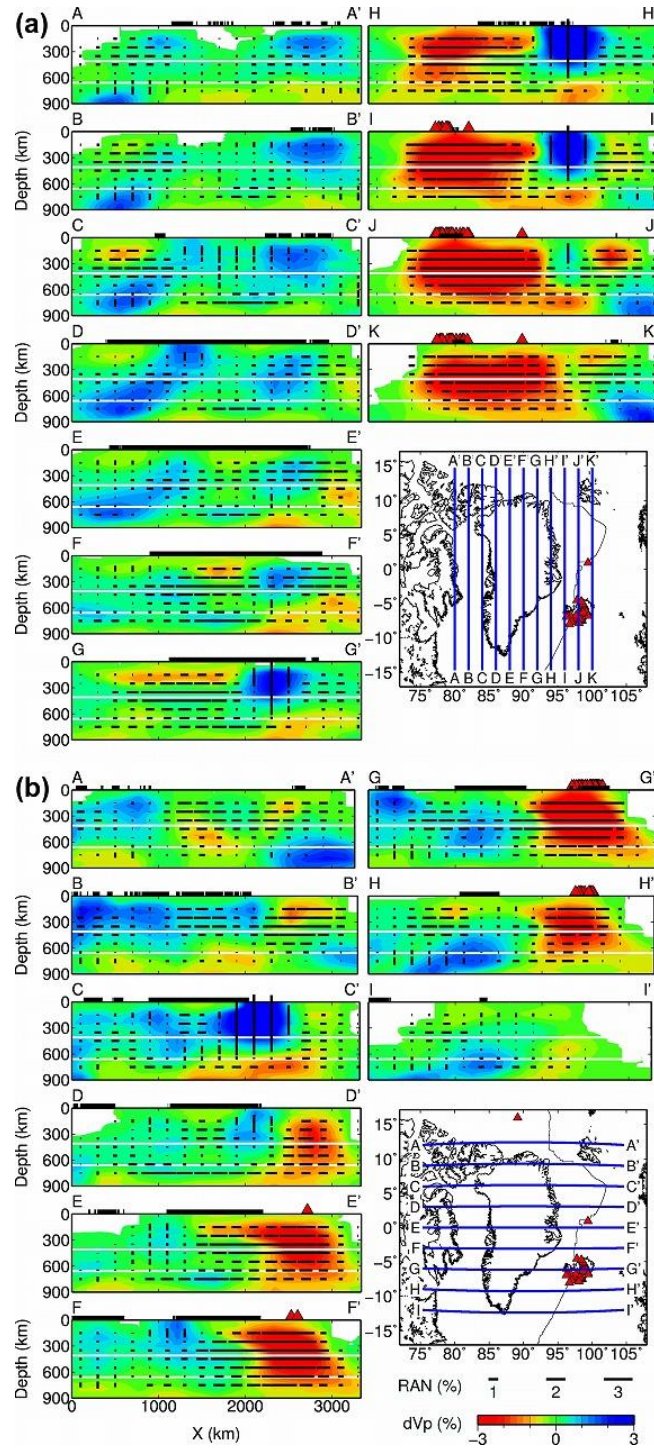
785

786

787

788

789



790

791 **Figure 4.** Vertical cross-sections of V_p radial anisotropy (RAN) tomography along (a) eleven N-
 792 S oriented profiles and (b) nine E-W oriented profiles. Locations of the profiles are shown on the

793 inset maps. Blue and red colors denote high and low isotropic V_p perturbations, respectively,
794 whose scale (in %) is shown at the bottom. The length of black bars denotes the RAN amplitude,
795 whose scale (in %) is also shown at the bottom. The horizontal and vertical bars denote positive
796 RAN ($V_{ph} > V_{pv}$) and negative RAN ($V_{ph} < V_{pv}$), respectively. Areas with hit counts < 5 are
797 masked in white. The 410-km and 660-km discontinuities are indicated by white solid lines. The
798 thick black lines on the surface denote land areas. Active volcanoes within a $\pm 2^\circ$ width of each
799 profile are shown as red triangles.

800

801

802

803

804

805

806

807

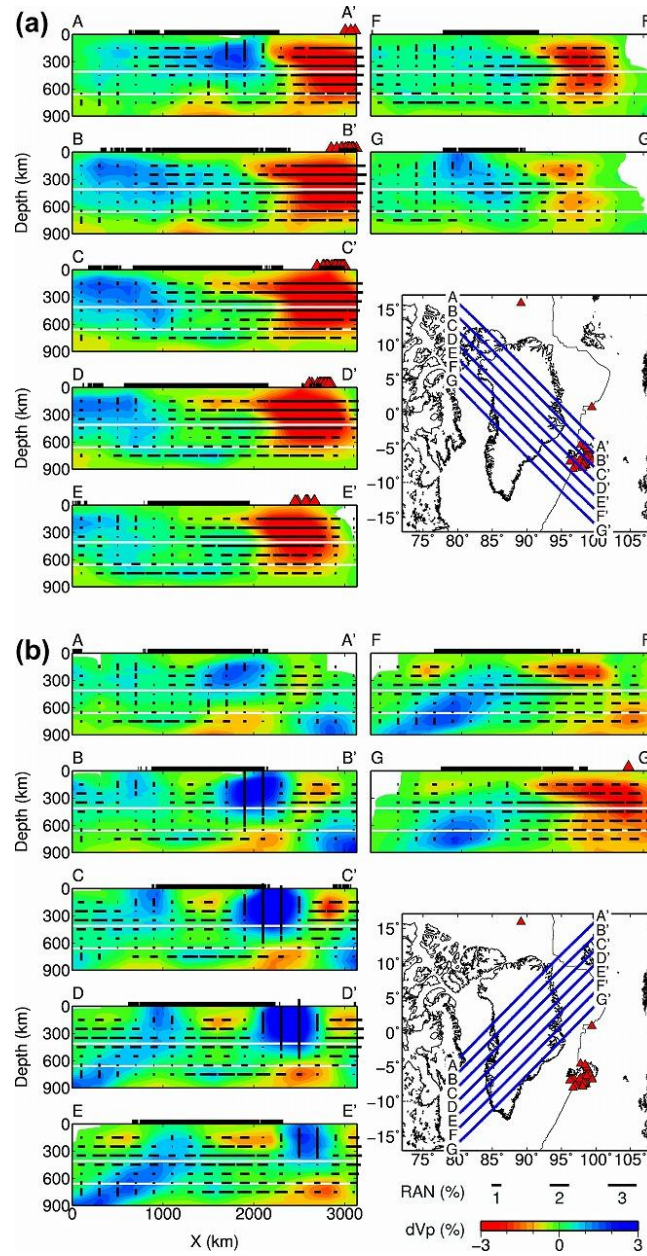
808

809

810

811

812

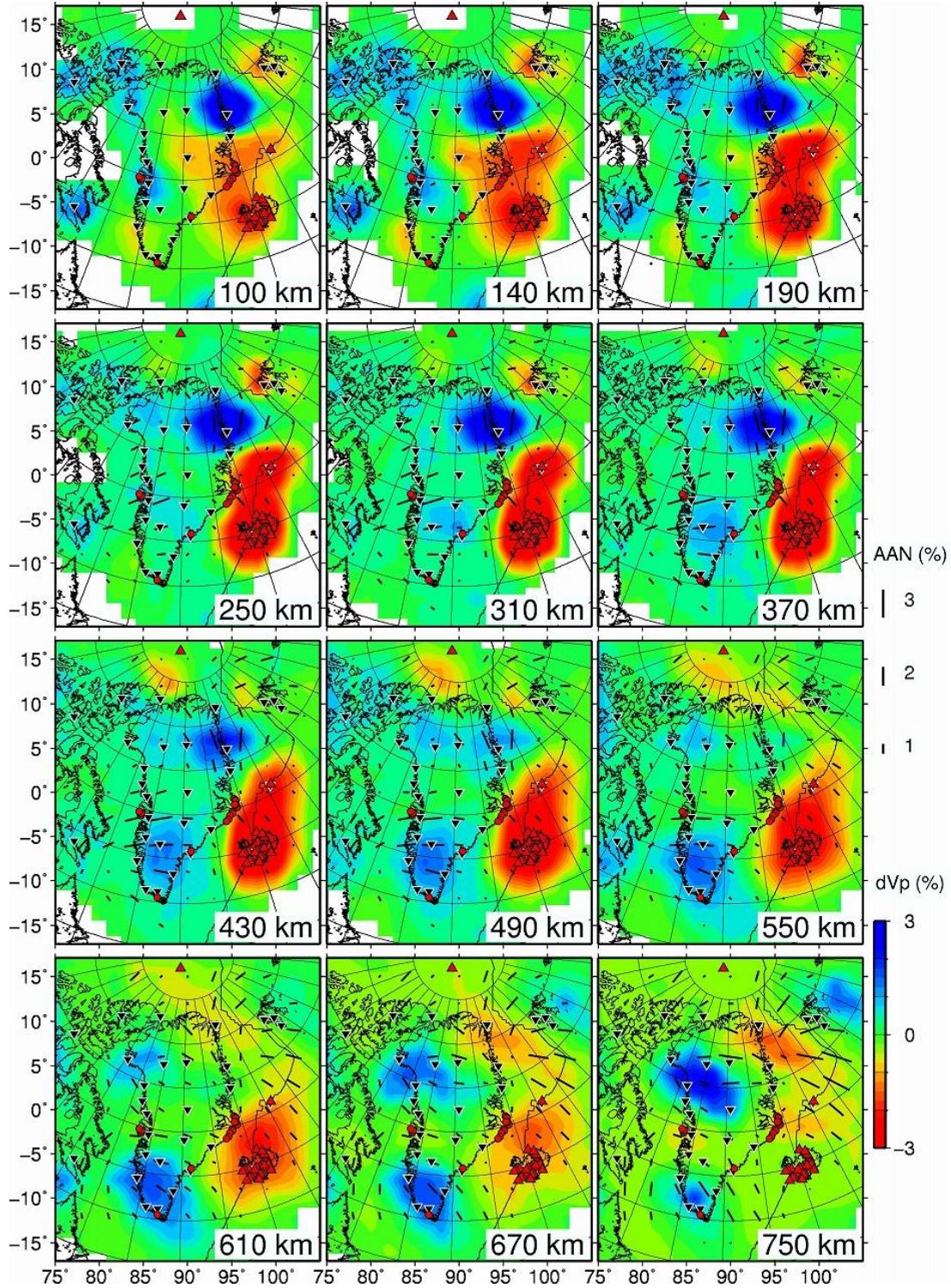


813

814 **Figure 5.** Same as [Figure 4](#) but along (a) seven NW-SE oriented profiles and (b) seven NE-SW
 815 oriented profiles.

816

817



818

819 **Figure 6.** Same as [Figure 3](#) but for V_p azimuthal anisotropy (AAN) tomography. The length of
 820 black bars denotes the AAN amplitude, whose scale (in %) is shown on the right. The bar

821 orientation denotes fast-velocity direction (FVD). The other symbols are the same as those in
822 [Figure 3](#) except for displaying the meridian of the geographical coordinates so that the FVDs are
823 more visible.

824

825

826

827

828

829

830

831

832

833

834

835

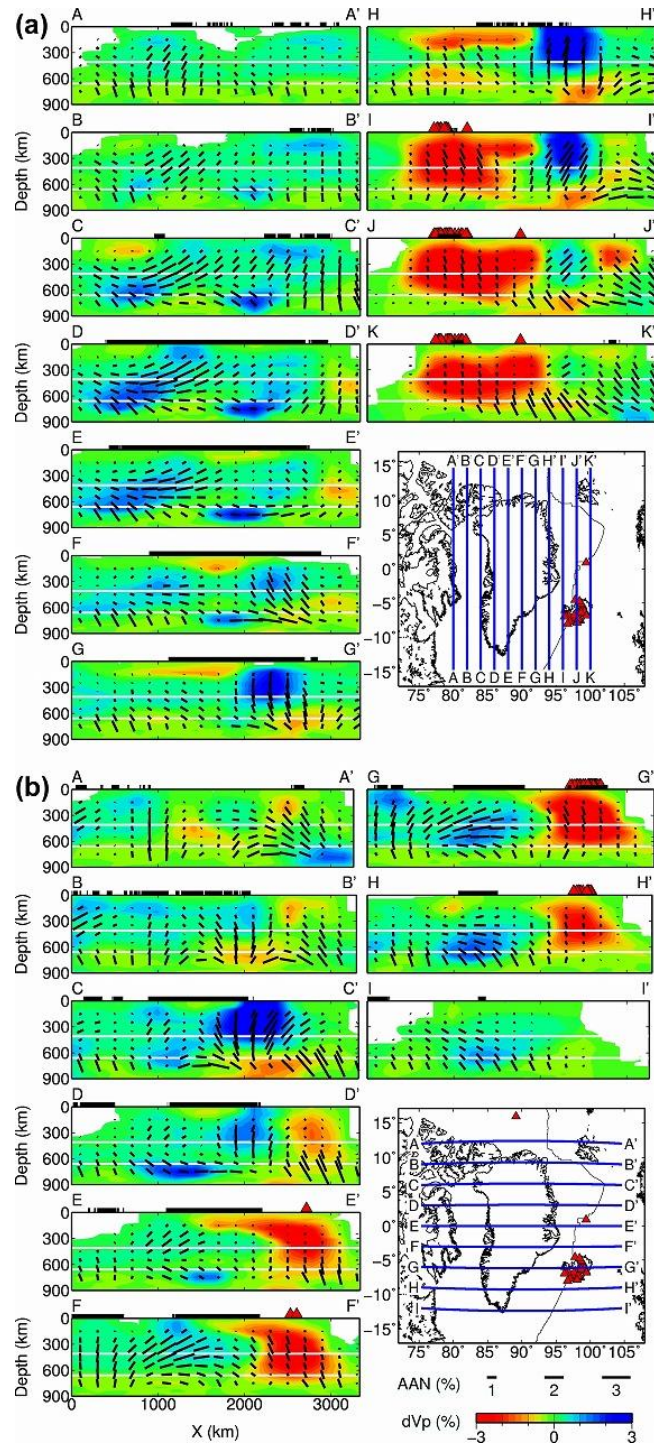
836

837

838

839

840



841

842 **Figure 7.** Same as [Figure 4](#) but for V_p azimuthal anisotropy (AAN) tomography. The length of

843 black bars denotes the AAN amplitude, whose scale (in %) is shown on the right. The bar

844 orientation denotes fast-velocity direction (FVD): vertical bars denote N-S FVDs, whereas
845 horizontal bars denote E-W FVDs. The other symbols are the same as those in [Figure 5](#).

846

847

848

849

850

851

852

853

854

855

856

857

858

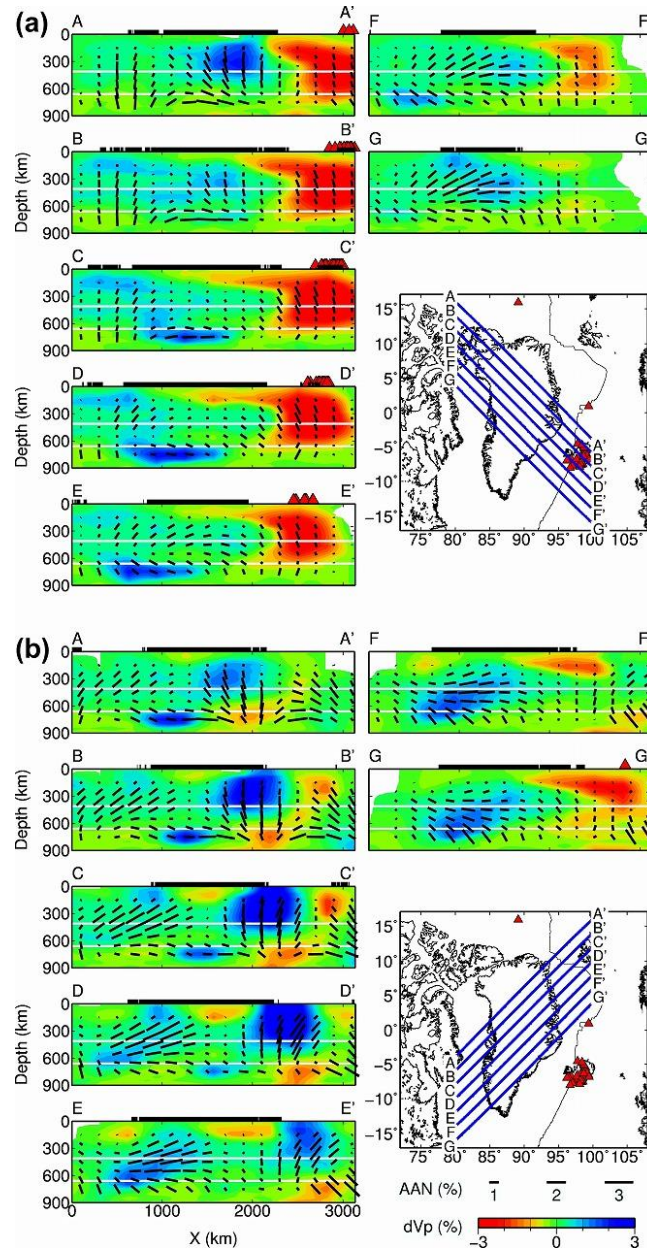
859

860

861

862

863



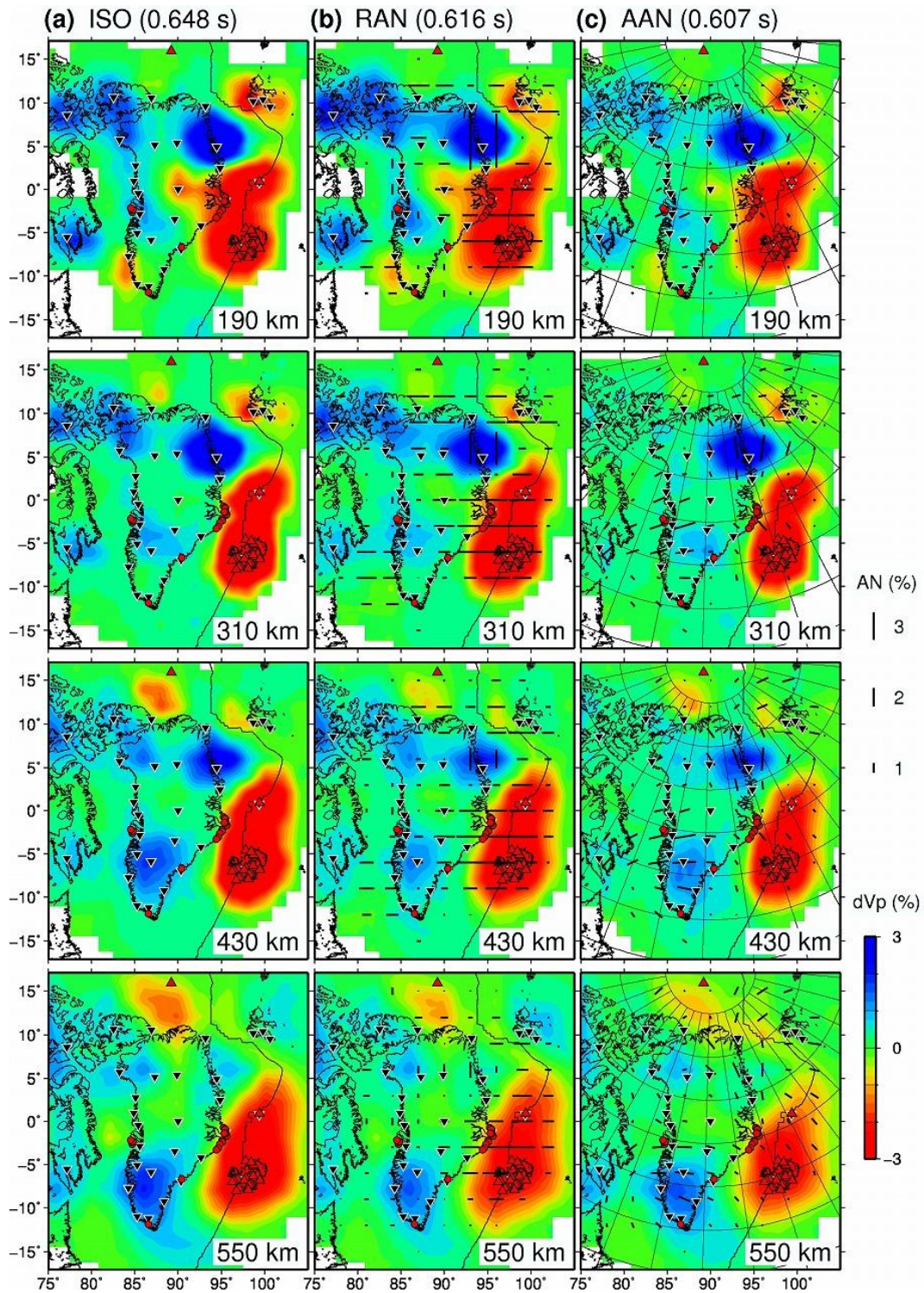
864

865 **Figure 8.** Same as [Figure 7](#) but along (a) seven NW-SE oriented profiles and (b) seven NE-SW

866 oriented profiles.

867

868



869

870 **Figure 9.** Comparison of (a) isotropic V_p tomography, (b) V_p radial anisotropy (RAN)
 871 tomography, and (c) V_p azimuthal anisotropy (AAN) tomography with the same 3-D grids, and

872 the same damping and smoothing parameters. The layer depth is shown at the lower-right corner
873 of each panel.

874

875

876

877

878

879

880

881

882

883

884

885

886

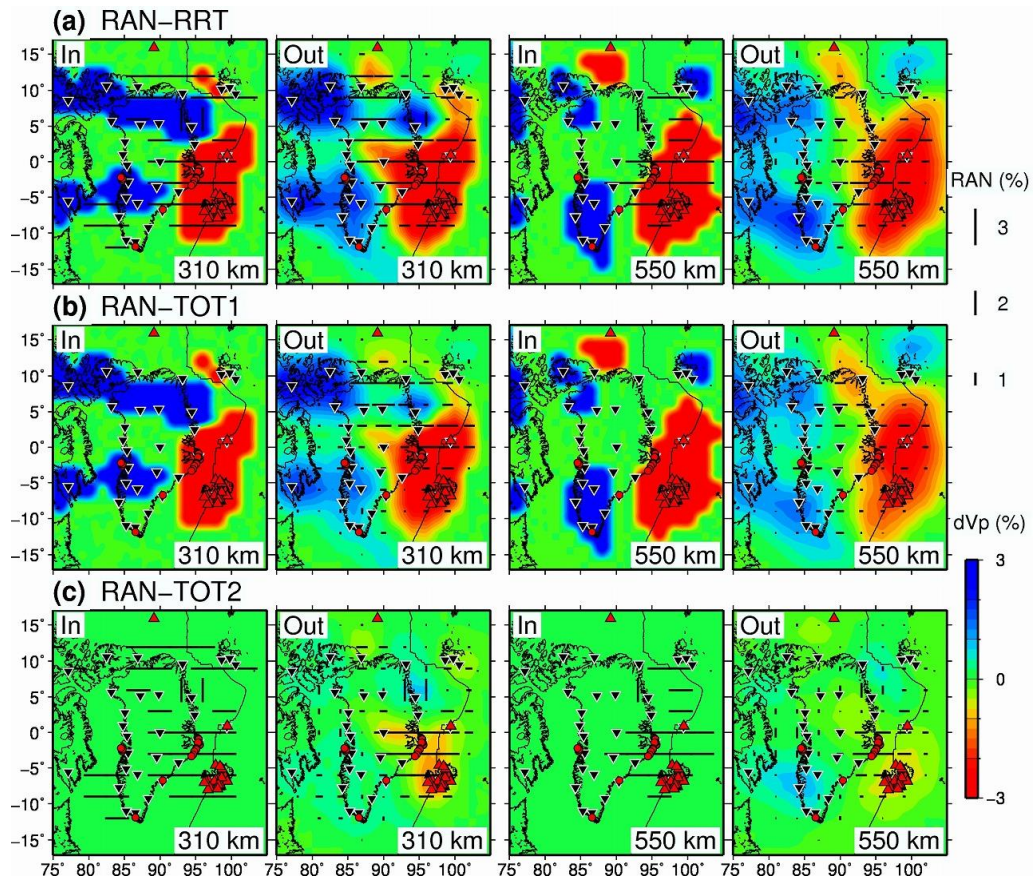
887

888

889

890

891



892

893 **Figure 10.** Summary of the resolution tests for V_p radial anisotropy (RAN) tomography. Map
 894 view images of the input (left panels) and output (right panels) models of the (a) RAN-RRT, (b)
 895 RAN-TOT1, and (c) RAN-TOT2 at depths of 310 km and 550 km. The layer depth is shown at
 896 the lower-right corner of each panel. The scales and symbols are the same as those in Figure 3.

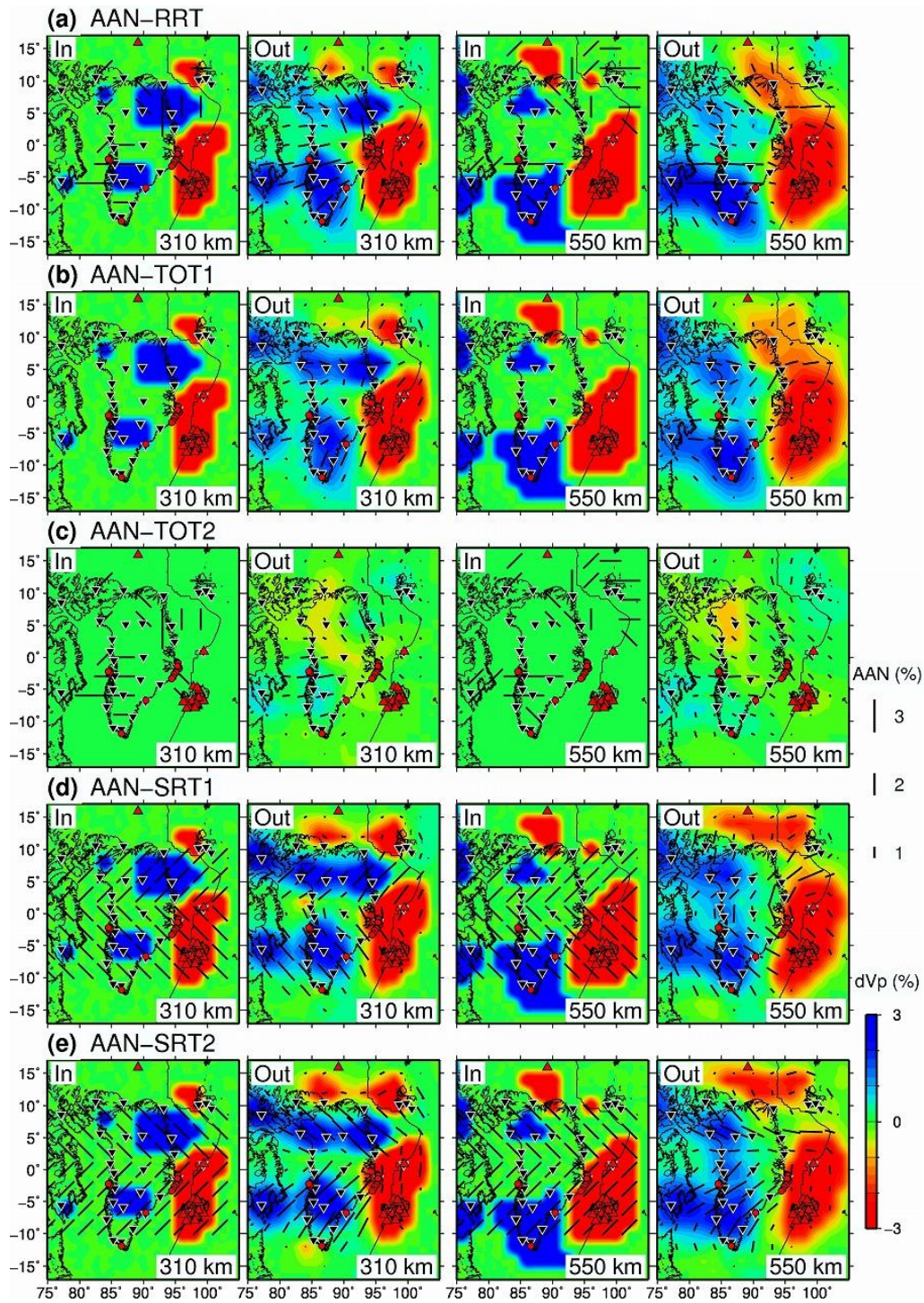
897

898

899

900

901



902

903 **Figure 11.** Summary of the resolution tests for V_P azimuthal anisotropy (AAN) tomography.

904 Map view images of the input (left panels) and output (right panels) models of the (a) AAN-RRT,

905 **(b)** AAN-TOT1, **(c)** AAN-TOT2, **(d)** AAN-SRT1, and **(e)** AAN-SRT2 at depths of 310 km and
906 550 km. The layer depth is shown at the lower-right corner of each panel. The scales and
907 symbols are the same as those in [Figure 6](#).

908

909

910

911

912

913

914

915

916

917

918

919

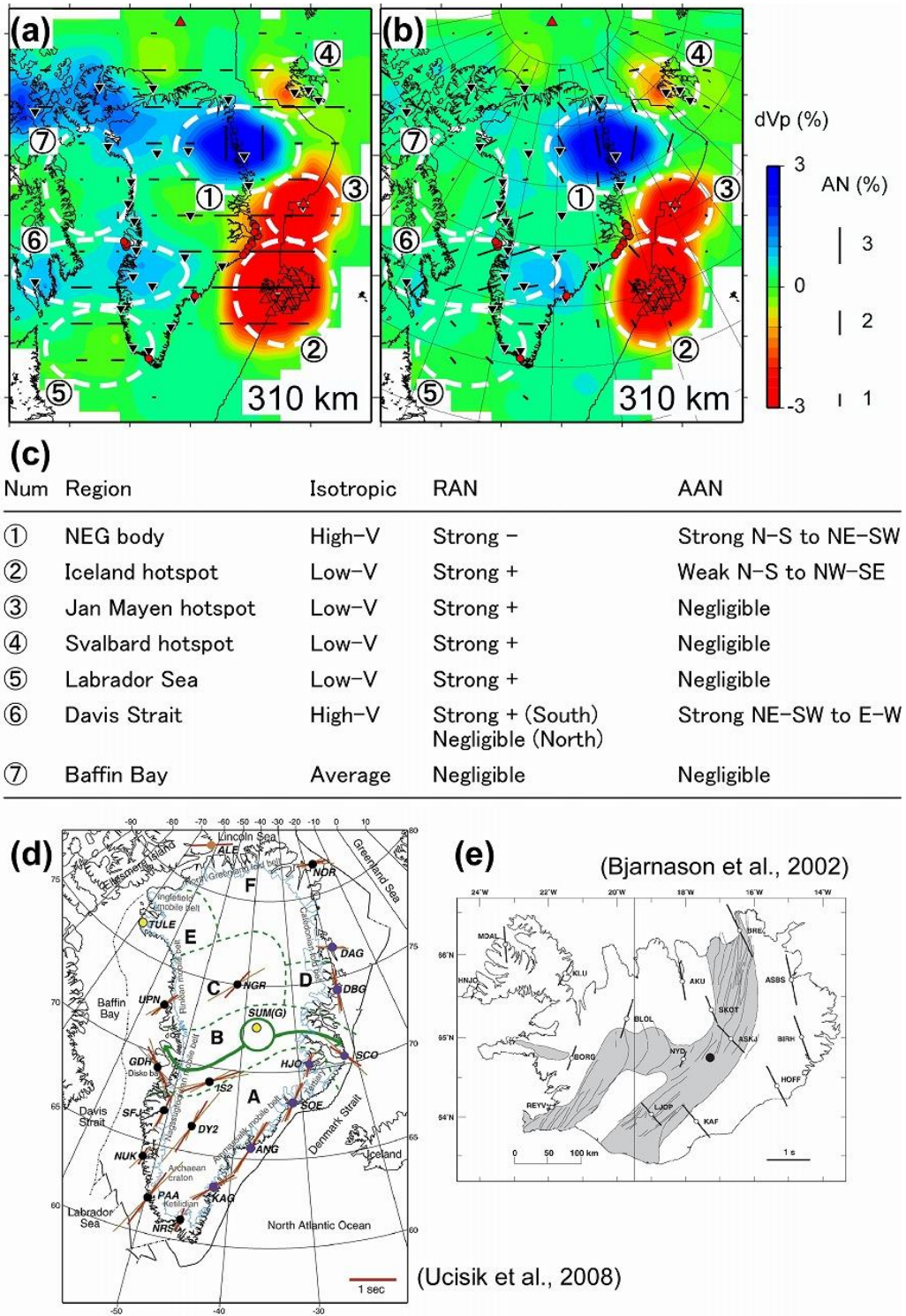
920

921

922

923

924



925

926 **Figure 12.** Main features of seismic anisotropy obtained by this study and comparison with shear
 927 wave splitting (SWS) measurements. Map view images of (a) V_p radial anisotropy (RAN)

928 tomography and **(b)** V_p azimuthal anisotropy (AAN) tomography at 310-km depth obtained by
929 this study. The scales are shown on the right. The major regions are numbered 1–7, whose
930 features are summarized in **(c)**. The other symbols are the same as those in Figures 3 and 6. **(d)**
931 SWS measurements at 20 stations in Greenland ([Ucisik et al., 2008](#)). The thick red bars denote
932 the fast-polarization orientation whose length showing the time delay, whereas the thin brown
933 bars denote their 2σ uncertainties. The yellow dots denote stations where the SWS is not
934 observed. **(e)** SWS measurements at 16 stations in Iceland ([Bjarnason et al., 2002](#)). The thick
935 black bars denote the fast-polarization orientation whose length showing the time delay.

936

937

938

939

940

941

942

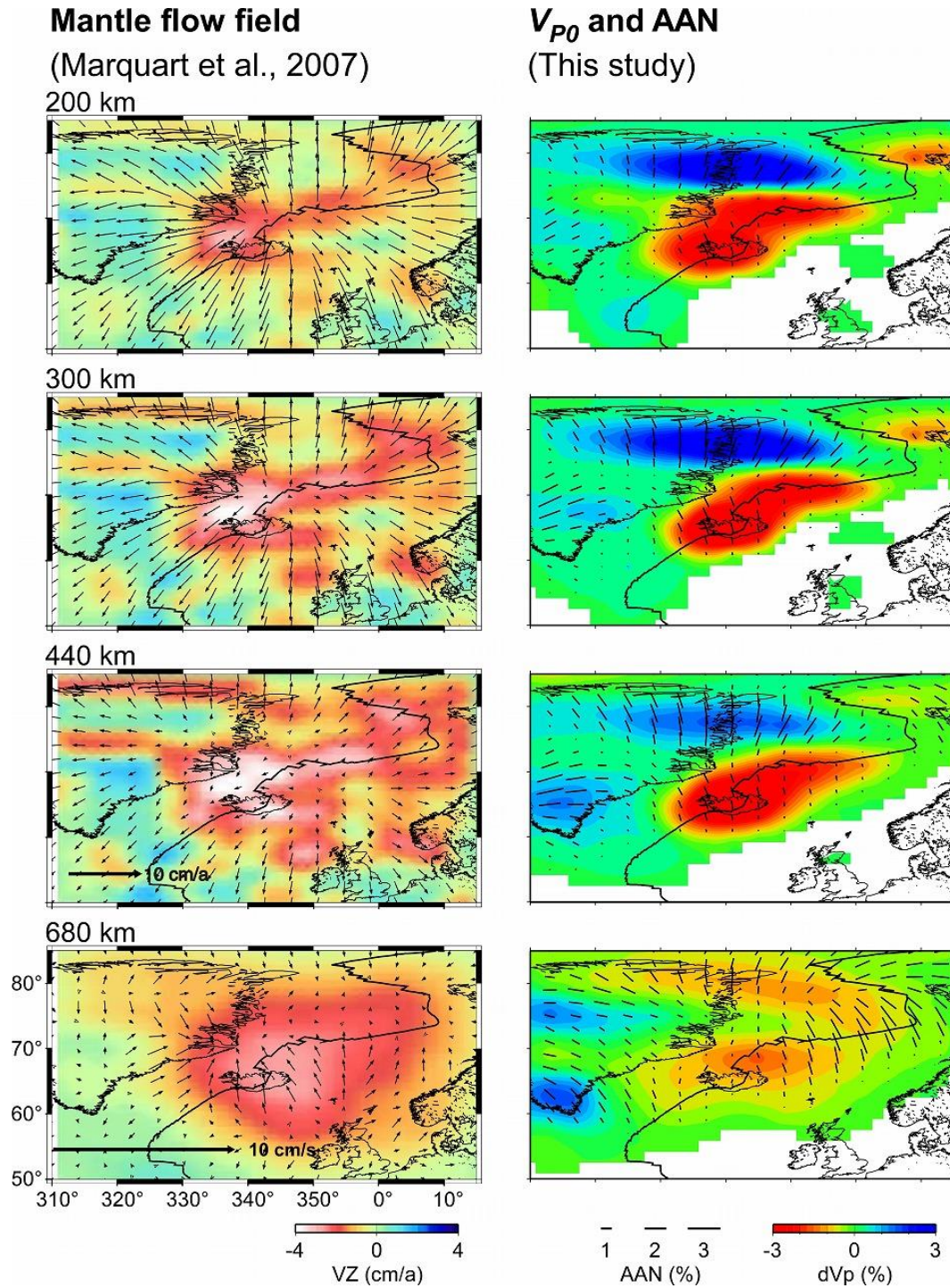
943

944

945

946

947



948

949 **Figure 13.** Comparison of the mantle flow field simulated by Marquart et al. (2007) (left) with
950 V_P azimuthal anisotropy (AAN) tomography obtained by this study (right). The layer depth is

951 shown above each map on the left. In the mantle flow field, horizontal flow is shown by arrows
952 whose scales are displayed on the 440-km map for the upper mantle, and on the 680-km map for
953 the lower mantle; vertical flow is shown by colors whose scale is shown at the bottom-left. The
954 AAN tomographic images are the same as those in [Figure 6](#) except that they are displayed in the
955 Cartesian coordinates.

956

957

958

959

960

961

962

963

964

965

966

967

968

969

970

971

972

973 **Table 1.** Information on the eight resolution tests conducted by this study.

Name	Description of the initial model
	Restoring resolution test. Highlights the pattern of actual RAN tomographic results.
RAN-RRT	Isotropic component: Contains high- V_{p0} (+3%) and low- V_{p0} (-3%). Anisotropic component: Contains positive α (+2%) and negative α (-2%).
RAN-TOT1	Trade-off test. Similar to the RAN_RRT model, but without the anisotropic component.
RAN-TOT2	Trade-off test. Similar to the RAN_RRT model, but without the isotropic component.
	Restoring resolution test. Highlights the pattern of actual AAN tomographic results.
AAN-RRT	Isotropic component: Contains high- V_{p0} (+3%) and low- V_{p0} (-3%). Anisotropic components: $\beta = +2\%$, $\psi = -45^\circ, 0^\circ, 45^\circ, \text{ or } 90^\circ$.
AAN-TOT1	Trade-off test. Similar to the AAN_RRT model, but without the anisotropic components.
AAN-TOT2	Trade-off test. Similar to the AAN_RRT model, but without the isotropic component.
	Synthetic resolution test. The model contains the following structures: Isotropic component: Same as the AAN_RRT
AAN-SRT1	Anisotropic components: $\beta = +2\%$, $\psi = 45^\circ$ for a region in the longitude range 90° – 100° and latitude range 0° – 10° , and $\psi = -45^\circ$ for a region in the longitude range 80° – 90° and latitude range -10° – 0° . Synthetic resolution test. The model contains the following structures: Isotropic component: Same as the AAN_RRT
AAN-SRT2	Anisotropic components: $\beta = +2\%$, $\psi = -45^\circ$ for a region in the longitude range 90° – 100° and latitude range 0° – 10° , and $\psi = 45^\circ$ for a region in the longitude range 80° – 90° and latitude range -10° – 0° .

974